

FLIGHT PROTOTYPE MODEL METEOR FLASH ANALYZER

by

F. N. Mastrup and C. D. Bass

FINAL REPORT

GPO PRICE \$ _____

CSFTI PRICE(S) \$ _____

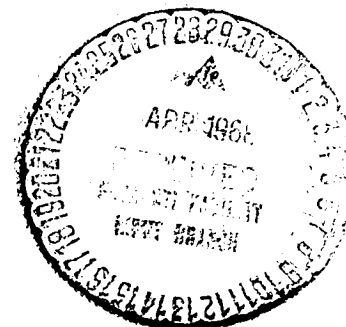
Hard copy (HC) 300

Microfiche (MF) 65

ff 653 July 65

Prepared for
NATIONAL AERONAUTICS AND SPACE ADMINISTRATION
Manned Spacecraft Center
Contract No. NAS9-6532

APRIL 1968



TRW
SYSTEMS GROUP

ONE SPACE PARK · REDONDO BEACH, CALIFORNIA

N68-21440
(ACCESSION NUMBER)
194
(PAGES)
CL-58-047
(NASA CR OR TMX OR AD NUMBER)
(THRU)
(CODE)
(CATEGORY)

FLIGHT PROTOTYPE MODEL METEOR FLASH ANALYZER

by

F. N. Mastrup and C. D. Bass

Final Report

Prepared for

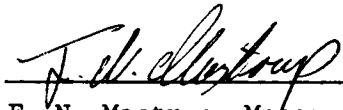
National Aeronautics and Space Administration

Manned Spacecraft Center

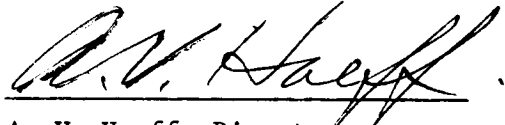
Contract No. NAS 9-6532

April 1968

Approved by:



F. N. Mastrup, Manager
Gaseous Electronics Department



A. V. Haeff, Director
Physical Electronics Laboratory

TRW Systems Group

One Space Park, Redondo Beach, California 90278

TABLE OF CONTENTS

	PAGE
LIST OF FIGURES	v
FOREWORD AND ACKNOWLEDGEMENTS	ix
SUMMARY	xi
1. INTRODUCTION.	1
2. EXPERIMENT CONCEPT AND PURPOSE.	2
2.1 Experiment Objectives.	2
2.2 Significance of the Meteor Flash Analyzer Experiment	2
2.3 Optical Meteor Observables and Data Interpretation	9
2.4 Anticipated Prime Obstacles and Uncertainties.	13
3. DETECTION OF OPTICAL METEORS FROM AN ORBITAL PLATFORM (DETAILED DISCUSSION)	14
3.1 Predicted Sporadic Meteor Abundance and Average Meteor Entry Velocity in the Solar System.	14
3.2 Experimental Concept Description	17
3.2.1 Optical Radiation from Meteors and Definition of Meteor Flash Analyzer Optical Observables.	17
3.2.2 The Background Radiation Environment.	22
3.2.3 Basic MFA Signal Channel Description.	26
3.2.4 Signal/Noise Ratios and Detection Sensitivity	29
3.2.5 Predicted Meteor Count Rates and Observable Meteor Magnitudes	34
3.2.6 Expected Background Signal Strengths in Earth Orbit.	36
3.3 Methods for Carrying Out an Orbital MFA Experiment	37
3.3.1 The Sensor Assembly (Figures 7, 9).	37
3.3.2 Basic Description of the Detector Electronic System.	38
3.3.3 Method for Carrying Out the MFA Experiment.	39

TABLE OF CONTENTS (Continued)

	PAGE
4. APPARATUS DESCRIPTION	
4.1 Mechanical and Necessary Equipment.	42
4.2 Electronic Systems Description.	47
4.2.1 Basic System	47
4.2.2 Summary System Specifications.	47
4.2.3 Signal Channel Description	52
4.2.4 Telemetry Interface Block Diagram.	56
4.2.5 Power Conversion, Protection Circuits and Calibration Generation	56
5. CALIBRATION FACILITY AND PROCEDURE	60
5.1 Calibration Test Facility	60
5.1.1 Relative Spectral Response	60
5.1.2 Relative Field-of-View Response.	60
5.1.3 Absolute Spectral Response	60
5.1.4 Optical Background Simulation and Sun Sensor Function	61
5.1.5 Additional Facilities.	61
5.1.6 Special Test Equipment	61
5.2 Calibration Test Procedure.	63
5.2.1 Electronic Tests	63
5.2.2 Relative Spectral Response	65
5.2.3 Field-of-View.	66
5.2.4 Absolute Responsivity.	69
5.2.5 Meteor Flash Simulation.	70
5.2.6 Sun Sensor Test.	73
5.2.7 Noise Level.	74

TABLE OF CONTENTS (Continued)

	PAGE
6. CALIBRATION TEST RESULTS.	75
6.1 Electronic Test Results.	75
6.1.1 Temperature Monitor	75
6.1.2 Signal Channel Response	75
6.1.3 Experiment Status Voltage	75
6.1.4 Photodiode Circuit Tests.	93
6.1.5 Calibration Lamp Circuit Test	93
6.2 Spectral Response.	93
6.3 Field-of-View.	103
6.4 Absolute Responsivity.	128
6.5 Optical Flash Simulation	130
6.6 Sun Sensor Test Results.	152
6.7 Noise Test Results	152
 7. RECOMMENDATIONS	
 APPENDIX A	A-1
A-1 INTRODUCTION.	A-1
A-2 APPARATUS	A-2
A-2.1 Particle Accelerator	A-2
A-2.2 Differential Pumping System and Target Chamber for Relative Radiant Energy Distribution Measurements.	A-4
A-3 RESULTS	A-9
A-4 TIME DEPENDENCE OF THE LIGHT EMISSION	A-17
A-5 ABSOLUTE RADIANT EFFICIENCIES	A-19
A-6 CONCLUSIONS	A-23
REFERENCES	A-24
LIST OF FIGURES.	A-25

LIST OF FIGURES

FIGURE NO.	TITLE	PAGE
1	Relative Sensitivity Function of the Long Wavelength Channel; Nominal $0.30 \mu - 0.40 \mu$	6
2	Relative Sensitivity Function of the Intermediate Wavelength Channel; Nominal $0.26 \mu - 0.30 \mu$	7
3	Relative Sensitivity Function of the Far UV Wavelength Channel; Nominal $0.22 \mu - 0.26 \mu$	8
4	Definition of Nightglow Intensities $I'(0)$ and $I'(\alpha)$	23
5	Signal Channel Optical Arrangement.	28
6	Experimental Geometry.	29
7	Sensor Assembly (Cover Removed).	43
8	Electronic Assembly (Cover Removed).	44
9	Fully Assembled Meteor Flash Analyzer with Connecting Cable	45
10	Experiment Test Set Unit	46
11	Basic Block Diagram Meteor Flash Analyzer.	48
12	Block Diagram Basic Signal Channel	53
13	Signal Channel Wave Forms.	55
14	Block Diagram Telemetry Interface Circuits	57
15	Block Diagram Power Conversion and Protection Circuits	58
16	Circuit Block Diagram of Optical Flash Simulator	62
17	Electronic Test Block Diagram.	64
18	Relative Spectral Response Test Block Diagram.	67
19	Optical Flash Simulation Test Block Diagram.	71
20	Electronic Calibration, Peak A. Ambient Temperature and 3 Values of α Abscissa for Gain 21; $x \ 21/6$ for Gain 6; $x \ 21/53$ for Gain 53.	81

LIST OF FIGURES (Continued)

FIGURE NO.	TITLE	PAGE
21	Electronic Calibration, Peak A. 1 Value of α , 3 Temperatures. Abscissa for Gain 21; x 21/6 for Gain 6; x 21/53 for Gain 53.	82
22	Electronic Calibration, Area A. 1 Value of α , 3 Temperatures. Abscissa for Gain 21; x 21/6 for Gain 6; x 21/53 for Gain 53.	83
23	Electronic Calibration, Area A. Ambient Temperature and 3 Values of α . Abscissa for Gain 21; x 21/6 for Gain 6; x 21/53 for Gain 53.	84
24	Electronic Calibration, Peak B. Ambient Temperature and 3 Values of α . Abscissa for Gain 21; x 21/6 for Gain 6; x 21/53 for Gain 53.	85
25	Electronic Calibration, Peak B. 1 Value of α , 3 Temperatures. Abscissa for Gain 21; x 21/6 for Gain 6; x 21/53 for Gain 53.	86
26	Electronic Calibration, Area B. 1 Value of α , 3 Temperatures. Abscissa for Gain 21; x 21/6 for Gain 6; x 21/53 for Gain 53.	87
27	Electronic Calibration, Area B. Ambient Temperature and 3 Values of α . Abscissa for Gain 21; x 21/6 for Gain 6; x 21/53 for Gain 53.	88
28	Electronic Calibration, Peak C. Ambient Temperature and 3 Values of α . Abscissa for Gain 21; x 21/6 for Gain 6; x 21/53 for Gain 53.	89
29	Electronic Calibration, Peak C. 1 Value of α , 3 Temperatures Abscissa for Gain 21; x 21/6 for Gain 6; x 21/53 for Gain 53.	90
30	Electronic Calibration, Area C. 1 Value of α , 3 Temperatures. Abscissa for Gain 21; x 21/6 for Gain 6; x 21/53 for Gain 53.	91

LIST OF FIGURES (Continued)

FIGURE NO.	TITLE	PAGE
31	Electronic Calibration, Area C. Ambient Temperature and 3 Values of α . Abscissa for Gain 21; $\times 21/6$ for Gain 6; $\times 21/53$ for Gain 53.	92
32A	Relative Response Test Data. Optical System Output Measured with Thermocouple Detector.	94
32B	Relative Response Test Data. Optical System Output Measured with Thermocouple Detector.	95
33A	Relative Response Test Data. Channel A Output Signal. . . .	96
33B	Relative Response Test Data. Channel A Output Signal. . . .	97
34A	Relative Response Test Data. Channel B Output Signal. . . .	98
34B	Relative Response Test Data. Channel B Output Signal. . . .	99
35A	Relative Response Test Data. Channel C Output Signal. . . .	100
35B	Relative Response Test Data. Channel C Output Signal. . . .	101
36	Field-of-View Contours, Channel A.	124
37	Field-of-View Contours, Channel B.	125
38	Field-of-View Contours, Channel C.	126
39	Field-of-View Contours, Photodiode	127
40	Absolute Spectral Responsivity, Channel A.	132
41	Absolute Spectral Responsivity, Channel B.	133
42	Absolute Spectral Responsivity, Channel C.	134
43	Comparison of Optical Flash Data and Electronic Calibration. Peak A, $\alpha = 3.2$ for Gain 21.	145
44	Comparison of Optical Flash Data and Electronic Calibration. Area A, $\alpha = 3.2$ for Gain 21.	146
45	Comparison of Optical Flash Data and Electronic Calibration. Peak B, $\alpha = 3.2$ for Gain 21.	147

LIST OF FIGURES (Continued)

	TITLE	PAGE
46	Comparison of Optical Flash Data and Electronic Calibration. Area B, $\alpha = 3.2$ for Gain 21.	148
47	Comparison of Optical Flash Data and Electronic Calibration. Peak C, $\alpha = 3.2$ for Gain 21.	149
48	Comparison of Optical Flash Data and Electronic Calibration. Area C, $\alpha = 3.2$ for Gain 21.	150
49	Oscilloscope Traces for Some Flash Simulation Tests.	151
APPENDIX		
A-1	Block Diagram of Experimental Arrangement.	A-5
A-2	Relative Spectral Response of EMI 6255 uv Photomultiplier Tube	A-6
A-3	Relative Intensity of Light Emission from Iron Particles In Air. High Velocity Particles are 30 km/sec average and Low Velocity Particles are 25 km/sec Average. Vertical Error Bars are Two Standard Deviations and Horizontal Error Bars are Full-Width-at-Half Maximum of the Filter-Phototube Combination.	A-10
A-4	Relative Intensity of Light Emission from Iron Particles in 44% CO ₂ - 56% N ₂ . High Velocity Particles are 30 km/sec Average and Low Velocity Particles are 25 km/sec Average. Vertical Error Bars are Two Standard Deviations and Horizontal Error Bars are Full-Width-at-Half-Maximum of the Filter-Phototube Combination.	A-11
A-5	Relative Intensity of Light Emission from Iron Particles in 75% CO ₂ - 25% A. High velocity particles are 30 km/sec average and low velocity particles are 25 km/sec average. Vertical error bars are two standard deviations and horizontal error bars are full-width-at-half-maximum of the filter phototube combination	A-12
A-6	Relative Intensity of Light Emission from Iron Particles in 100% CO ₂ . High velocity particles are 30 km/sec average and low velocity particles are 25 km/sec average. Vertical error bars are two standard deviations and horizontal error bars are full-width-at-half-maximum of the filter phototube combination	A-13

FOREWORD AND ACKNOWLEDGEMENTS

This final report on Contract No. NAS 9-6532 terminates a total of 14 months effort by TRW on the definition, design, construction and testing of a Meteor Flash Analyzer prototype for detecting and analyzing optical meteor flashes in planetary atmospheres. As a result of this effort a functional and fully tested instrument is now available which can be adapted with minimal design changes to existing spacecraft. Specific missions under consideration are the Apollo Applications program, the Nimbus E mission and a Mars mission on a spacecraft like Voyager. The latter mission offers from many aspects by far the greatest scientific challenge.

Many scientists and engineers associated with NASA and TRW contributed significantly to the program during its conception and execution. The problem came to the attention of F. N. Mastrup, the principal investigator, during a discussion at TRW in Spring 1965 in which S. Altshuler of TRW posed the problem of detection of optical meteors in the Martian atmosphere for determining the heavy meteor abundance in the vicinity of Mars. F. N. Mastrup studied and defined the present Meteor Flash Analyzer concept in a TRW Technical Report dated July 8, 1965. A proposal was subsequently submitted to NASA Headquarters for the study and design of an instrument. In the following months, many fruitful discussions were conducted with W. Keller and C. T. D'Aiutolo of NASA Headquarters. The final definition of the program and technical direction involved members of the Meteoroid Sciences Branch of NASA-MSC. Most of all, the numerous technical contributions from B. Cour-Palais and D. Kessler of NASA-MSC have significantly contributed to the course of the program.

F. N. Mastrup has been principal investigator and also project engineer on the first phase (study and breadboard construction) which ended in June 1967. The program continued 27 July 1967 with C. D. Bass assuming project engineering responsibilities for the second phase, (prototype). The electronic circuit design and construction has been mostly done by R. G. Yamasaki and G. Crook. Mechanical optical design and functional design has been executed under the direction of C. D. Bass. J. Atkinson (electronic manufacture and testing), H. Bobitch (mechanical design), and E. Thompson (mechanical manufacture) deserve specific mention for their significant

contributions.

J. F. Friichtenicht, J. C. Slattery and E. Tagliaferri have conducted the experiments on meteor spectral radiation distribution and absolute luminous efficiencies. Their experimental exploration of the far uv emission of iron meteors and of the gas target composition effect have significantly contributed to the long range goals of the Meteor Flash Analyzer program.

SUMMARY

The concept for carrying out an experiment for detecting and analyzing optical meteor flashes generated from planetary meteor entry has been studied and feasibility has been demonstrated.

A prototype model Meteor Flash Analyzer has been designed, constructed, and tested. The apparatus consists of a three-channel radiometer utilizing adjacent wavelength bands $\langle 0.23\mu; 0.26\mu \rangle$ (silicon channel), $\langle 0.26\mu; 0.30\mu \rangle$ (magnesium channel) and $\langle 0.30\mu; 0.41\mu \rangle$ (iron channel). Present information on average meteor composition, the wavelength location of the resonance lines or resonance multiplets of the respective elements and contemporary theory of meteor radiation, strongly suggests the above indicated association of optical bands with the radiation from specific meteor components. The long wavelength (iron) channel nearly coincides with the conventional spectral range for "photographic meteors" thus providing the necessary correlation of all data with contemporary (ground based) observational data. It has been shown that for terrestrial meteors in the iron channel detection sensitivity is background radiation limited. It is for this reason that optical detection of meteors in wavelength bands below the ozone limit at $\sim 0.30\mu$ appears to yield superior sensitivity.

The principal source of terrestrial nightglow below 0.30μ is believed to be associated with $O_2: {}^3\Sigma_u^+ \rightarrow X {}^3\Sigma_g^-$ at wavelengths greater than 0.26μ . No measurable nightglow has been recorded below this wavelength. Therefore, the far UV channel could be essentially detector limited with resulting significant increase in signal/noise.

Count rates and limiting meteor magnitudes have been predicted for the iron channel (photographic range) where reliable data on meteor radiation and background are available. For satellite altitude of 120 nautical miles, detector field-of-view of 30° , and detector aperture diameter of 5 cm, limiting photographic meteor magnitude is +3.3 resulting in an inverse count rate of 5.6 minutes/meteor. At 600 nautical miles the same detector is expected to yield inverse count rate of 22 minutes/meteor and limiting photographic meteor magnitude of -1.1. It is expected that significantly larger count rates will

be observed on the magnesium and silicon channels, although reliable predictions cannot be made at present for lack of relevant data. Because of this fact, provisions for gain adjustments have been provided for matching detector sensitivity to acceptable count rates. These gain adjustments can be effected by channel command independently for each radiometer channel. Minimum acceptable inverse count rate is limited by the electronic system and is 0.3 minutes/meteor.

The Meteor Flash Analyzer is designed to determine for each meteor flash and simultaneously in three wavelength bands the maximum meteor intensity, F_{\max} , and the time integrated meteor intensity, $\int F dt$. Video outputs have been provided for each channel allowing the measurement of the intensity vs. time variations of individual meteor flashes. In addition to the meteor data, there is a background measuring data channel for each of the three optical channels. The total of 9 meteor data channels can be used for the following:

- a) determining the far UV meteor radiation intensities and far UV absolute meteor radiation efficiencies
- b) for determining relative meteor composition variations $[Fe] \div [Mg] \div [Si]$
- c) for testing contemporary meteor radiation theory applied to the far UV radiation
- d) for determining meteor distribution functions $f(s)$ and $g(r)$ where $s = (v \cdot \cos \theta)/H$ and $r = m \cdot (H/\cos \theta)^3$ with v = meteor entry velocity, θ = meteor entry angle, m = meteor mass, and H = atmospheric scale height at the meteor burn-up altitude
- e) for measuring meteor intensity vs. time relation for meteor radiation simultaneously for the three optical channels.

The 3 background monitor channels will yield additional valuable data on background, although this is not expected to be substantially new data.

The Meteor Flash Analyzer contains also a fourth optical channel using a large dynamic range photodiode for providing continuous background radiation monitoring and automatic Meteor Flash Analyzer turn-on and turn-off during orbiting. This is necessary for protecting the sensitive optical signal channels from excessive irradiation levels. Automatic optical sensor calibration once during each orbit has also been provided.

The presently available prototype consists of the sensor assembly (weight: 8.3 lbs.; dimensions: 8.75" x 6.25" x 6.25") and the electronics assembly (weight: 6.2 lbs; dimensions: 7.5" x 7.5" x 6.625"). Total weight of the package is 15 lbs. and total power requirement is 7.5 Watts. As part of the program, a supporting laboratory study has been conducted on the radiation from electrically accelerated artificial iron micrometeorites impacting on gas targets of different compositions. Four gas mixtures were studied: a) Air, b) CO₂, c) 75% CO₂ - 25% A, d) 44% CO₂ - 56% Ne. Gases and gas mixtures b), c) and d) represent the composition of three martian model atmospheres presently being considered.

The laboratory study has yielded two most significant results:

- 1) relative spectral energy distribution of artificial iron micrometeorites in the velocity range 15 km/sec - 30 km/sec is independent of the varying gas composition of mixtures a), b), c) and d). Absolute radiative efficiency does depend on gas mixture. Mixture d) yields absolute radiative efficiency comparable to air. The two mixtures b and c yield radiation efficiency approximately one half that of air. From these measurements it appears that nitrogen contributes to high meteor radiation efficiency. A nitrogen deficient martian atmosphere would very likely yield only half as intense meteors relative to a terrestrial meteor of the same meteor mass, entry velocity, entry angle. Atmospheric scale heights are comparable for the two atmospheres according to recent NASA data.

1. INTRODUCTION

The Meteor Flash Analyzer program has been conducted in two phases: Phase 1 aimed at the definition of the measurements program and at the construction of a breadboard of the electronics portion of the Meteor Flash Analyzer. The work covered under Phase 1 has been described in detail in the interim final report, "Flight Prototype Model Meteor Flash Analyzer" by F. N. Mastrup, G. M. Crook, J. F. Friichtenicht and R. G. Yamasaki, May 1967. Phase 2 involved further studies on the definition of the orbiting Meteor Flash Analyzer Experiment, the design and construction of a flight model Meteor Flash Analyzer prototype, and the functional testing of such an instrument. In addition laboratory studies on electrically accelerated artificial iron micrometeorites were required. All these tasks have been fully accomplished and an experimental apparatus has evolved significantly more advanced and capable than the apparatus originally envisioned in our proposal. Specifically the most notable improvement is the addition of a third (silicon) channel, providing simultaneous coverage of the optical bandwidth most significant for all the important meteor components, Fe, Mg and Si. Other definite improvements over the original concept were the addition of three video outputs for allowing viewing of individual meteor intensity vs. time functions, improved experiment logic and telemetry interface, better light protection and provisions for gain switching thus allowing the experimenter to match instrument sensitivity to actually observed meteor count rates during orbiting. These experiment improvements were effected without additional costs to the program.

The present final report supersedes the interim final report published May 8, 1967 at the end of the Phase 1 program. Some of the information in Sections 2, 3 and 4 duplicates essentially information already presented in the earlier report; however, the information and conclusions have been significantly updated and improved. Sections 5, 6 and 7 are specific to the second phase program as they describe the design and tests of the flight model prototype. The spectral measurements on artificial micrometeorites are sufficiently independent from the main effort of this program that their presentation in a separate Appendix A appeared to be practical. Also for practical reasons the "Operating Instructions" have been published separately as Appendix B.

2. EXPERIMENT CONCEPT AND PURPOSE

2.1 EXPERIMENT OBJECTIVES

The Meteor Flash Analyzer Experiment is designed to count and analyze optical radiation pulses from meteors entering the nightside of the planetary atmospheres. Optical data will be recorded simultaneously in three wavelength bands $0.23 \mu \leftrightarrow 0.26 \mu$; $0.26 \mu \leftrightarrow 0.30 \mu$; and $0.30 \mu \leftrightarrow 0.40 \mu$ using a three-channel radiometer. In order to accomplish the objectives of the experiment, the optical observables F'_{\max} (maximum meteor intensity), $\int F' dt$ (integrated meteor intensity), and I' (background intensity) will be measured in all three wavelength bands. These data will be used to (1) determine relative meteor radiation efficiencies in the far ultraviolet inaccessible to ground-based observation, to (2) check consistency of contemporary meteor radiation theory, to (3) determine meteor distribution functions $g(r)$ and $f(S)$ where $S = (v \cdot \cos\theta)/H$, $r = (mH^3)/\cos^3 \theta$, m = meteor mass, v = meteor velocity, θ = meteor entry angle, and H = atmospheric scale height, to (4) attempt an interpretation of measured relative meteor intensities in the three wavelength channels in terms of the relative abundance ratios of $[Fe] \div [Mg] \div [Si]$ in meteors. Aside from the major objectives, additional experimental information on the intensity vs. time relationship of meteor-pulses and on the Earth background (nightglow) radiation is expected to be generated by the experiment.

2.2 SIGNIFICANCE OF THE METEOR FLASH ANALYZER EXPERIMENT

The Meteor Flash Analyzer (MFA) experiment was originally suggested¹ as a possible method of determining the mass-flux relationships of massive meteors in the vicinity of planets such as Mars and possibly Venus. This ultimate experiment objective remains as an important motivating aspect of the work. Although more limited in objective and scope, an Earth orbiting experiment constitutes a first necessary step towards the ultimate goal.

The significance of an Earth orbiting meteor experiment can be summarized as follows:

¹F. N. Mastrup, "Meteor Flash Analyzer," TRW Technical Report, July 8, 1965.

(a) The experiment will yield new quantitative data on far ultra-violet radiation from terrestrial meteors; evaluation and interpretation of these data in terms of contemporary meteor radiation theory may provide advanced understanding of the meteor radiation phenomena.

(b) The experiment will determine which of the three channels $< 0.23 \mu$; $0.26 \mu >$, $< 0.26 \mu$; $0.30 \mu >$ and $< 0.30 \mu$; $0.40 \mu >$ provides best signal/noise for detection of terrestrial meteors from Earth orbit. This experimental result can then be used in conjunction with the results of relevant laboratory experiments which have been conducted as part of this program to determine the best spectral range for planetary (Mars, Venus) meteor counting missions. Experiments of this type, including some already in the planning stage,² will probably be proposed in the near future because of widespread interest in determining mass-flux relationships for large meteors throughout the solar system.

(c) The Meteor Flash Analyzer concept of determining, from optical observables of individual meteors, values for $S = (v \cdot \cos\theta)/H$ and $r = (mH^3)/(\cos^3\theta)$ must be tested before it can be applied with reasonable assurance in missions to other planets. The concept will be tested by determining for terrestrial meteors distribution functions $f(S) \Delta S$ and $g(r) \Delta r$ and comparing these with the same distribution functions as calculated from the known mass-flux-velocity distributions of terrestrial meteors. If the concept proves valid, a simple tool for obtaining the unknown distribution functions for other planets will be available.

(d) The Meteor Flash Analyzer channels have been specifically selected to look for the iron $< 0.30 \mu$; $0.40 \mu >$, the magnesium $< 0.26 \mu$; $0.30 \mu >$ and the silicon $< 0.22 \mu$; $0.26 \mu >$ components in the total meteor radiation. It is expected, on the basis of contemporary meteor radiation theory, that the measured ratios:

$$\int F'(0.30; 0.40)dt \div \int F'(0.26; 0.40)dt \div \int F'(0.22; 0.26)dt$$

$$= \sigma_{Fe} [Fe] \div \sigma_{Mg} [Mg] \div \sigma_{Si} [Si]$$

²F. N. Mastrup, "An Experiment to Determine the Impact Rate, the Mass and Velocity Spectrum of Massive Martian Meteors from a Mars Orbiter," for Voyager 1971, NASA Log No. SL98 SC 05-(080), dated November 17, 1965.

where $[Fe]$; $[Mg]$; $[Si]$ are the relative concentrations in mole fractions of the elements in the meteor and σ_{Fe} ; σ_{Mg} ; σ_{Si} are constants proportional to the molecular excitation cross sections. Variations of intensity ratios for the three channels are therefore expected to yield directly relative meteor composition fluctuations.

Present theory of terrestrial meteor radiation is largely of a phenomenological nature and needs critical evaluation before conclusion can be shown for entry into planetary atmospheres radically different from the terrestrial atmospheres. Laboratory studies³ have therefore been conducted to study the effect of atmospheric composition on artificial meteor radiation in all wavelength ranges from approximately 0.23μ to 0.65μ using charged artificial iron micrometeorites accelerated to velocities in the range from approximately 15 km/sec to 30 km/sec. The artificial micrometeorites are made to collide with a target gas under controlled conditions of pressure and gas compositions. These experiments are expected to yield valuable information on the effect of target gas composition on meteor radiation. However, because of scaling and difficulties in obtaining electrically accelerated micrometeorites of high silicon content as in real meteors, experiments with real meteors are essential to determine absolute radiative efficiencies for far ultraviolet meteor radiation and to validate contemporary meteor theory for those wavelength ranges. One does expect significantly better signal/noise ratios for optical meteor detection in the far uv ranges, because of lower background radiation as will be discussed in Section 3.2. The Meteor Flash Analyzer optical signal channel selection is based upon the criteria discussed in the following.

The long wavelength channel encompasses the wavelength band $0.30 \mu \leftrightarrow 0.40 \mu$. It covers approximately the conventional photographic range of meteors and permits therefore to establish the relationship of the MFA-data with already available information from ground based observations. Furthermore, this channel is particularly adapted to look at the "iron component" of the meteor radiation. To demonstrate this point, we give the wavelength ranges

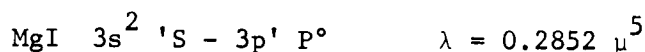
³J. C. Slattery, J. F. Friichtenicht, E. Tagliaferri, and F. N. Mastrup, (to be published).

for the iron resonance multiplets and the actually measured relative sensitivity function of the MFA channel (Figure 1):

FeI	$a^5D - Z^5F^\circ$	$0.3649 \mu - 0.3748 \mu^4$
	$a^5D - Z^5D^\circ$	$0.3824 \mu - 0.3930 \mu$
	$a^5D - Z^5P^\circ$	$0.3441 \mu - 0.3526 \mu$
	$a^5D - Y^5F^\circ$	$0.2954 \mu - 0.2973 \mu$
	$a^5D - Y^5D^\circ$	$0.2984 \mu - 0.3059 \mu$

The long wavelength channel can, therefore, literally be designated as the "iron channel."

The intermediate wavelength channel $0.26 \mu \leftrightarrow 0.30 \mu$ fulfills a similar function for measuring the "magnesium component," The magnesium spectrum is dominated by a single, very strong resonance line



which is at the very center of the intermediate wavelength channel pass band (Figure 2). A slight overlap with silicon and iron exists for this channel as can be seen from Figure 2. The rejection characteristics for Fe and Si might still be improved.

The short wavelength channel $0.23 \mu \leftrightarrow 0.26 \mu$ is especially selected to measure the "silicon component" by detecting the resonance multiplet



which is near the wavelength of peak far uv channel sensitivity (Figure 3). This optical channel selection takes on added significance if the average relative elemental abundance (mole fraction) of terrestrial meteors is considered (Table 1).

⁴Ch. E. Moore, "A Multiplet Table of Astrophysical Interest," NBS, Technical Note 36 (1959).

⁵Ch. E. Moore, "An Ultraviolet Multiplet Table," NBS, Circular 488, Section 1, (1950).

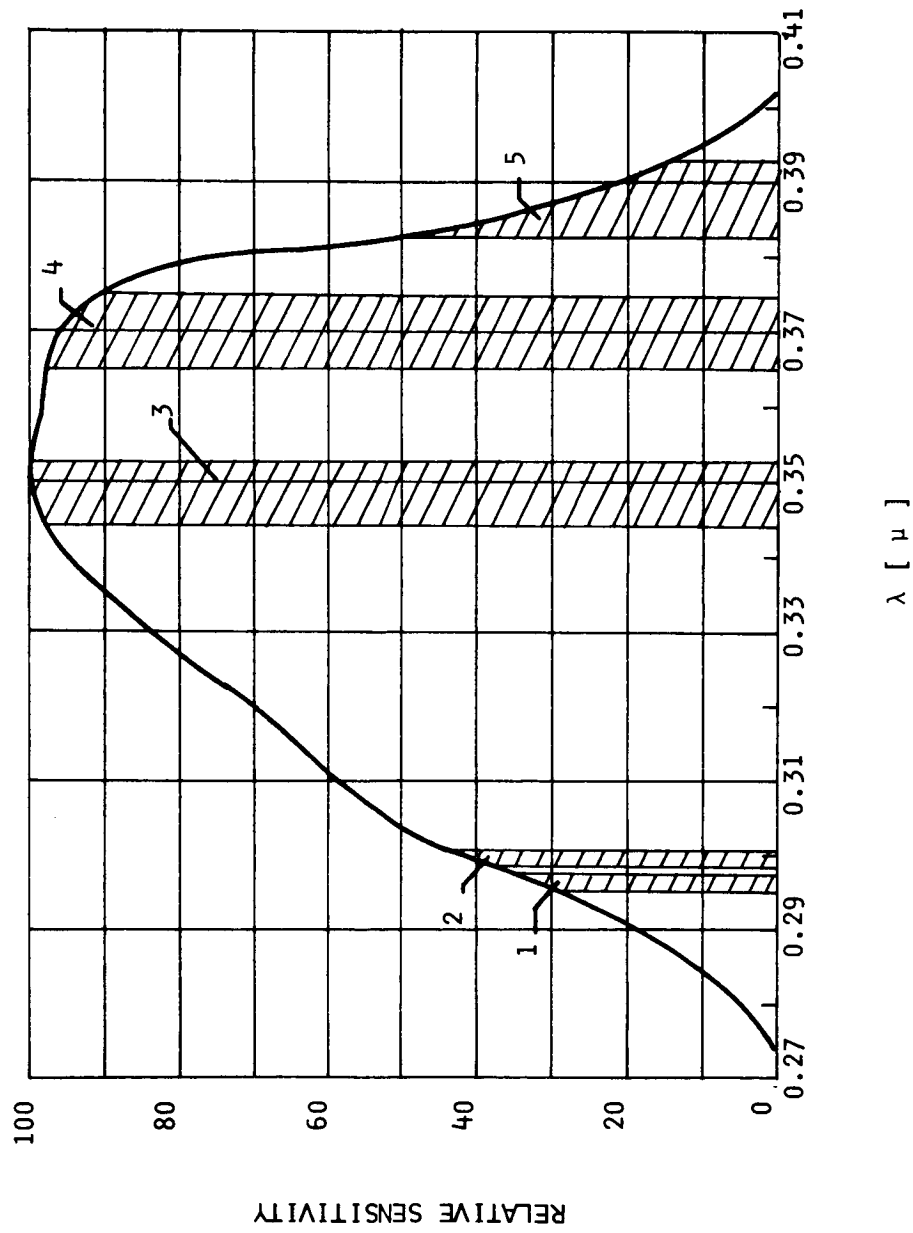
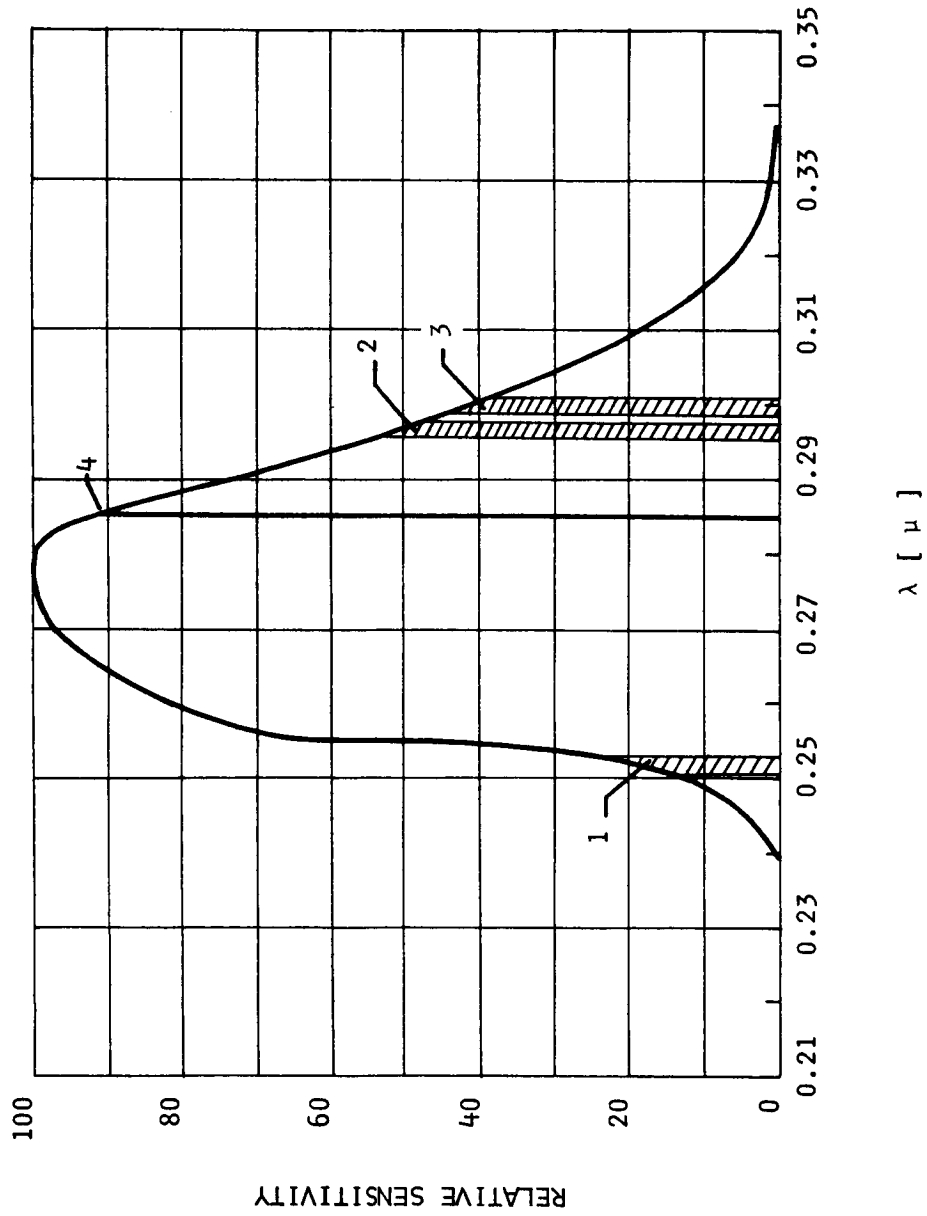


FIGURE 1. RELATIVE SENSITIVITY FUNCTION OF THE LONG WAVELENGTH CHANNEL; NOMINAL 0.30 μ - 0.40 μ



1. SiI $3p^2 \ 3P - 4s^3 \ p^o$
2. FeI $a^5D - \gamma^5F^o$
3. FeI $a^5D - \gamma^5D^o$
4. MgI $3s^2 \ 1S - 3p \ 1p^o$

FIGURE 2. RELATIVE SENSITIVITY FUNCTION OF THE INTERMEDIATE WAVELENGTH CHANNEL; NOMINAL $0.26 \mu - 0.30 \mu$

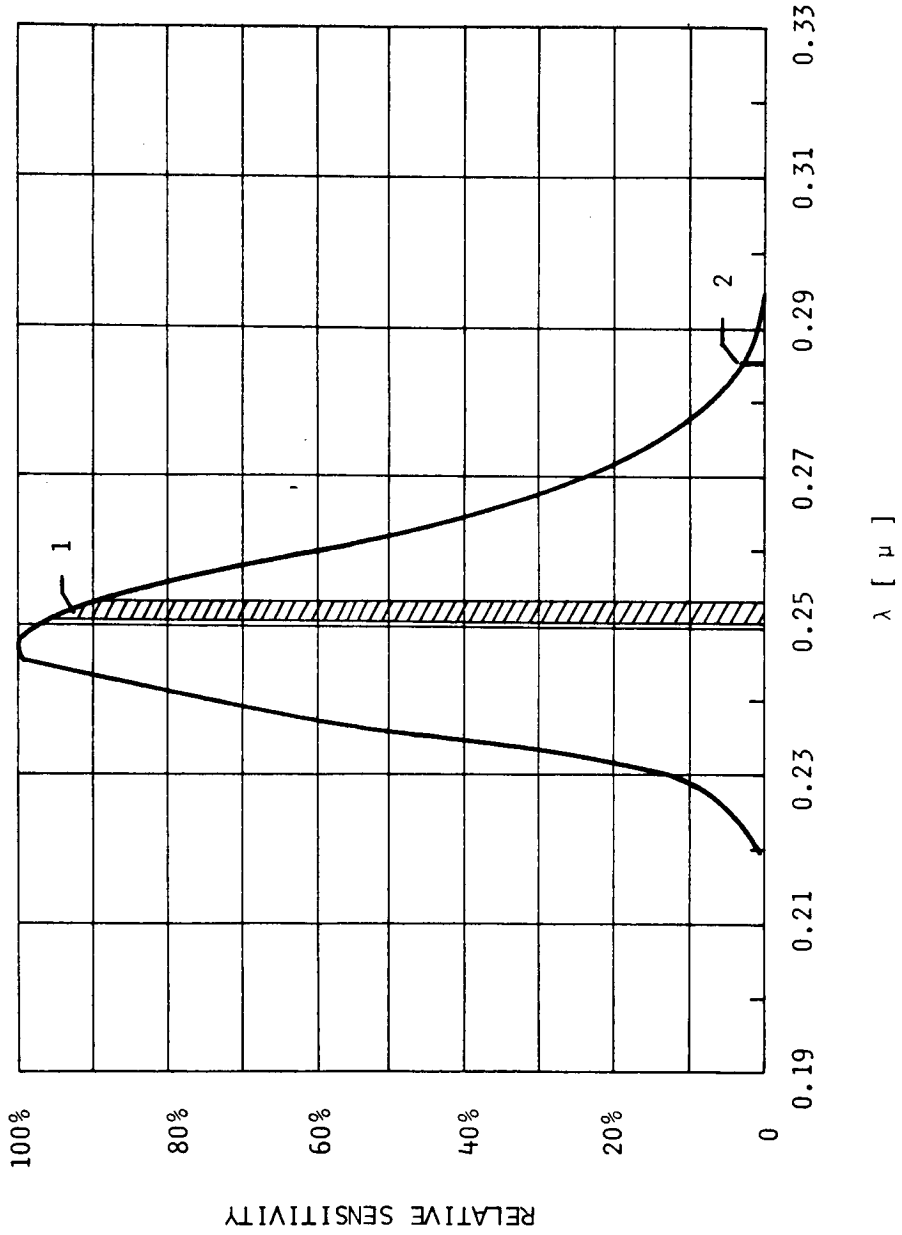


FIGURE 3. RELATIVE SENSITIVITY FUNCTION OF THE FAR UV WAVELENGTH CHANNEL; NOMINAL $0.22 \mu - 0.26 \mu$

Table 1. Average Relative Abundance
of Elements in Meteors
(Mole Fraction)

<u>Element</u>	<u>Abundance</u>
O	53 %
Si	15.5
Mg	14.5
Fe	11
Other elements	6

Considering the relative metal abundance in meteors and the fact that the spectral ranges of the resonance radiation of the important elements are well separated (little spectral overlap), it makes sense to define the three channels as the "iron", "magnesium", and "silicon" channel, respectively. Oxygen resonance radiation is in the vacuum ultraviolet (0.13 μ) and is not expected to contribute significantly to the radiation in the total wavelength band covered by the MFA. If the wavelength selection concept proves valid from actual data, the experiment becomes even more significant inasmuch as information on meteor composition can be obtained.

2.3 OPTICAL METEOR OBSERVABLES AND DATA INTERPRETATION

According to contemporary meteor radiation theory, the optical observables, F'_{\max} and $\int F' dt$, can be related to meteor mass m , entry angle θ , velocity v , and atmospheric scale height H , by the expressions:

$$F'_{\max}(\lambda_1; \lambda_2) = \frac{4}{9} A \frac{\lambda_2}{\lambda_1} \cdot \frac{m \cdot V^4 \cdot \cos\theta}{H} = \frac{4}{9} A \frac{\lambda_2}{\lambda_1} \cdot rs^4 \frac{\text{photons}}{\text{sec sterad}} .$$

$$\int F'(\lambda_1; \lambda_2) dt = \frac{\bar{\lambda} \cdot \tau_0(\lambda_1; \lambda_2)}{8\pi hc} mV^3 = A \frac{\lambda_2}{\lambda_1} mV^3 = A \frac{\lambda_2}{\lambda_1} rs^3 \frac{\text{photons}}{\text{sterad}} .$$

where parameters S and r are given by

$$S = \frac{v \cos \theta}{H}$$

$$r = \frac{mH^3}{\cos^3 \theta}$$

and $A_{\lambda_1}^{\lambda_2}$ is a constant related to the meteor "luminous efficiency" in the wavelength range $\langle \lambda_1; \lambda_2 \rangle$ (see also Section 3.1). Parameters S and r can be found from the observables by

$$S = \frac{9}{4} \frac{F'_{\max}(\lambda_1; \lambda_2)}{\int F'(\lambda_1; \lambda_2) dt}$$

$$rS^3 = \frac{\int F' dt}{A_{\lambda_1}^{\lambda_2}}$$

provided the luminous efficiencies $A_{\lambda_1}^{\lambda_2}$ are known. Evaluation of the latter constants for the two far ultraviolet channels is one of the objectives of the planned orbital experiment. This objective can be met by comparing integrated meteor flash intensities in the far ultraviolet channels with intensities in the long wavelength channel. The latter nearly coincides with the conventional photographic meteor wavelength range. For any meteor flash event, the following relationship holds:

$$A_{0.23}^{0.26} \div A_{0.26}^{0.30} \div A_{0.30}^{0.40}$$

$$= \int_{\max} F' (0.23; 0.26) dt \div \int_{\max} F' (0.26; 0.30) dt \div \int_{\max} F' (0.30; 0.40) dt$$

From the MFA observables F'_{\max} , $\int F' dt$, and I' and the derived quantities r and S, information can be obtained which satisfies the primary objectives of the experiment. The data will be evaluated as follows:

a. Determine Relative Radiation Efficiencies in the Far Ultraviolet

This objective will be accomplished by measuring the ratios of

$$\frac{A_{0.26}^{0.30}}{A_{0.30}^{0.40}} = \frac{\int F'(0.26;0.30)dt}{\int F'(0.30;0.40)dt} = a \left(F'_{\max}(0.30;0.40) \right)$$

$$\frac{A_{0.23}^{0.26}}{A_{0.30}^{0.40}} = \frac{\int F'(0.23;0.30)dt}{\int F'(0.30;0.40)dt} = b \left(F'_{\max}(0.30;0.40) \right)$$

For a large number of measurements the scatter of the ratios a and b will be determined. The data will be checked for independence (dependence) of constants a and b on $F'_{\max}(0.30;0.40)$ and for composition variations effects.

b. Determine Relative Meteor Composition Variations

Following contemporary meteor radiation theory one expects:

$$\begin{aligned} & \int F'(0.30;0.40)dt \div \int F'(0.26;0.30)dt \div \int F'(0.23;0.26)dt \\ & = \sigma_{\text{Fe}} [\text{Fe}] \div \sigma_{\text{Mg}} [\text{Mg}] \div \sigma_{\text{Si}} [\text{Si}] \end{aligned}$$

where [Fe]; [Mg]; [Si] are concentration in mole fractions of meteors and the σ are constants proportional to atomic excitation cross sections. An attempt will be made to interpret the scatter of constants a and b defined above in terms of relative concentration variations.

c. Test the Assumption of S-Independence on Wavelength Band

The S-values can be directly evaluated from MFA data by

$$S \approx \frac{F'_{\max}(\lambda_1; \lambda_2)}{\int F'(\lambda_1; \lambda_2)dt}$$

The ratios a' and b' defined below can then be evaluated:

$$\frac{S(0.26;0.30)}{S(0.30;0.40)} = \frac{F'_{\max}(0.26;0.30)}{\int F'(0.26;0.30)dt} \cdot \frac{\int F'(0.30;0.40)dt}{F'_{\max}(0.30;0.40)} = a'$$

$$\frac{S(0.23;0.26)}{S(0.30;0.40)} = \frac{F'_{\max}(0.23;0.26)}{\int F'(0.26;0.30)dt} \cdot \frac{\int F'(0.30;0.40)dt}{F'_{\max}(0.30;0.40)} = b'$$

Present assumptions suggest that $a' = 1$ and $b' = 1$.

- d. Determine from Orbital Data the Distribution Functions $f(S) \Delta S$ and $g(r) \Delta r$ for Terrestrial Meteors and Compare Results with Known Data for Photographic Meteors

The functions $f(S)$ and $g(r)$ are defined as follows:

$$f(S) \Delta S = \frac{\Delta n_S}{M_t} ; \quad g(r) \Delta r = \frac{\Delta n_r}{M_t}$$

where M_t is the total number of counts for which both r and S values have been obtained; Δn_S is the number of meteors yielding $\langle S; S + \Delta S \rangle$, and Δn_r is the number of meteors yielding $\langle r; r + \Delta r \rangle$.

- e. Evaluate Intensity vs. Time Relationships for Selected Meteor Pulses

This will be done for all three wavelength bands. Dependence of pulse shape on wavelength band will be checked and data compared with contemporary meteor radiation theory.

- f. Determine the Total Terrestrial Background Intensities

The background seen by detectors operating in the wavelength ranges $\langle 0.23 \mu; 0.26 \mu \rangle$, $\langle 0.26 \mu; 0.30 \mu \rangle$ and $\langle 0.30 \mu; 0.40 \mu \rangle$ will be determined as function of time during the experiment "on-time". The resulting background data will make possible improved signal/noise evaluation for future meteor detection experiments operating in the three indicated wavelength ranges.

2.4 ANTICIPATED PRIME OBSTACLES AND UNCERTAINTIES

An MFA prototype has already been built and functionally tested in the laboratory. There is no doubt, therefore, that the proposed instrument can be built to satisfy the weight and size specifications of this proposal.

Prime obstacles to the successful acquisition of data on all channels may be posed by one of the following conditions:

1. Far uv meteor radiance is substantially lower than expected.
2. Excessive increase of background by
 - a. Moonlight
 - b. Auroras
3. Erroneous signals from lightning flashes.

The existence of measureable far uv radiance has been documented by laboratory experiments on artificial iron micrometeorites.^{3,16,21} Theoretically, it is difficult to understand why, for example, the Si I resonance multiplet between 0.2507 μ and 0.2530 μ should not be excited in stony meteor trails. Yet, pertinent meteor data is not available at this time. One of the objectives of the MFA experiment is to make such data available. This would pave the way for advanced meteor detectors on planetary missions. In case substantial far uv meteor radiation should fail to materialize, this fact in itself would provide further insight into the meteor radiation problem. In that case, the long wavelength channel is still certain to return useful data.

Excessive background signal due to moonlight will affect primarily the long and intermediate wavelength channels. It is best not to conduct the experiment during times when auroras and moonlight would interfere with the experiment.

The possible interference caused by lightning flashes on the long wavelength radiometer channel has been discussed in Section 3.2.

3. DETECTION OF OPTICAL METEORS FROM AN ORBITAL PLATFORM (Detailed Discussion)

In this section the general problem of optical detection of massive meteors from orbiting satellites will be examined. Contemporary theory of optical meteor radiation will be combined with the background radiation field which originates primarily from nightglow. A set of practical Meteor Flash observables will be defined for measurement by the Meteor Flash Analyzer apparatus. Methods of data evaluation and estimates of sensitivity and count rates will be developed. The presented discussion is of relevance primarily for terrestrial meteors. During the discussion, occasional comments relevant to the experimental problem of measuring Martian meteors will be presented.

3.1 PREDICTED SPORADIC METEOR ABUNDANCE AND AVERAGE METEOR ENTRY VELOCITY IN THE SOLAR SYSTEM

Flux-mass relation presently adopted for massive meteors ($m \geq 10^{-2.19}$ gm = 6.4×10^{-3} gm) is⁶

$$\log_{10} P = - 1.34 \log_{10} m - 14.29 - \log_{10} \frac{\text{meteors } (>m)}{m^2 \cdot \text{sec}} \quad (1)$$

m = meteor mass (gm)

ρ = solar distance (A.U.)

P = accumulated impact rate of meteors of mass equal or greater than m (meteors/ $m^2 \cdot \text{sec}$).

There are additional seasonal variations for terrestrial meteors which can be included by adding a term $+\log_{10} S$ (S for seasonal variation) to Eq. (1)⁷.

⁶D. E. Evans, D. E. Pitts, and G. L. Kraus, "Venus and Mars Nominal Natural Environment for Advanced Planetary Mission Programs," 2nd ed., NASA SP-3016 (1967).

⁷NASA Design Standards Bulletin, DS-21, Rev. A, January 24, 1967, Code No. 1.1

Also, there is a minor difference in the constant in Eq. (1) between the References (6) and (7), the latter using a value of - 14.33. This small difference is of no consequence for the purpose of this discussion and we shall adopt, for this discussion, constants as given in Eq. (1). Rewriting Eq. (1) we obtain

$$P = \frac{5.13 \cdot 10^{-15}}{\rho \cdot m^{1.34}} \frac{\text{meteors } (\bar{v}_m)}{m^2 \cdot \text{sec}} \quad (1a)$$

Average relative velocity, V_c , of meteors relative to an object in circular orbit around the sun at distance ρ , is assumed to be⁶

$$V_c = \frac{2 \times 10^6}{\sqrt{\rho}} \text{ cm/sec} \quad (2)$$

In order to obtain average meteor entry velocity, one must account for the energy gain of the meteor from the gravitational potential of the meteor. Let \bar{V} be the average entry velocity into the planetary atmosphere. Then it is

$$\frac{m}{2} V_c^2 + U = \frac{m}{2} \bar{V}^2$$

where

$$U = GM m \cdot \int_{r_0}^{\infty} \frac{dr}{r^2} = \frac{GM}{r_0} m \text{ ergs}$$

r_0 = distance from planet center to burn-up height of meteors (cm)

G = gravitational constant ($6.67 \times 10^{-8} \text{ cm}^3/\text{gm sec}^2$)

M = planetary mass (gm)

Hence, average meteor entry velocity is

$$\bar{V} = \sqrt{V_c^2 + 2 \frac{GM}{r_0}} \text{ cm/sec} \quad (3)$$

Since the thickness of planetary atmospheres is thin compared to the planet's radius, the exact burn-up height of meteors is not critical for estimating \bar{V} from Eq. (3).

Employing known planetary characteristics⁸:

$$\text{Earth: } GM = 3.97 \times 10^{20} \frac{\text{cm}^3}{\text{sec}^2} ; r_o \approx 6.47 \times 10^8 \text{ cm}$$

$$\frac{2 GM}{r_o} = \frac{2 \cdot 3.97 \cdot 10^{20}}{6.47 \cdot 10^8} = 1.23 \cdot 10^{12} \frac{\text{cm}^2}{\text{sec}^2}$$

$$\text{Mars: } GM = 4.30 \times 10^{19} \frac{\text{cm}^3}{\text{sec}^2} ; r_o \approx 3.5 \times 10^8 \text{ cm}$$

$$\frac{2 GM}{r_o} = \frac{2 \cdot 4.30 \cdot 10^{19}}{3.5 \cdot 10^8} = 0.246 \cdot 10^{12} \frac{\text{cm}^2}{\text{sec}^2}$$

Combining Eqs. (2) and (3) with numerical values for Earth and Mars, respectively, one obtains for the average velocities:

$$\begin{aligned} \text{Terrestrial Meteors: } \bar{V}_{\oplus} &\approx 2.3 \times 10^6 \text{ cm/sec} \\ \text{Martian Meteors: } &(\rho = 1.52 \text{ A.U.}) \\ &\bar{V}_{\sigma} \approx 1.7 \times 10^6 \text{ cm/sec.} \end{aligned}$$

The influx rates of massive meteors as predicted by contemporary theory are, from Eq. (1a):

$$\text{Earth: } N_{\oplus} = \frac{5.13 \cdot 10^{-19}}{1.34} \frac{\text{meteors } (> m)}{\text{cm}^2 \cdot \text{sec}} \quad (1b)$$

$$\text{Mars: } N_{\sigma} = \frac{3.38 \cdot 10^{-19}}{1.34} \frac{\text{meteors } (> m)}{\text{cm}^2 \cdot \text{sec}} \quad (1c)$$

⁸C. W. Allen, "Astrophysical Quantities," University of London, The Athlone Press, (1955).

3.2 EXPERIMENTAL CONCEPT DESCRIPTION

Feasibility of an orbital Meteor Flash Analyzer experiment will be shown in this section. Based on the known elements of contemporary meteor radiation theory optical observables and observable strength for measurement from orbital platform will be evaluated. Combining signal strength with the signal derived from the background radiation yields signal/noise which determines the sensitivity of the experiment. Expected meteor count rates and limiting photographic meteor magnitudes will be evaluated.

3.2.1 Optical Radiation from Meteors and Definition of Meteor Flash Analyzer Optical Observables^{9,10,11}

Assume a meteor of mass m (gm) entering the atmosphere of the Earth at a velocity V (cm/sec). Contemporary theory assumes that

$$\int \frac{F}{V^3} dt = \frac{\tau_0^*}{2} m \quad , \quad (4)$$

where F is the meteor intensity in units of zero photographic (visual) magnitude of a meteor at 100 km height, V is the instantaneous velocity, and τ_0^* is the luminous efficiency constant. It is a well-established fact, from observations on Earth, that the velocity of most meteors does not vary appreciably during entry. Hence, the integrated meteor flash intensity (integrated over the whole luminous period) can be approximated by

$$\int F dt = \frac{\tau_0^*}{2} mV^3 \quad . \quad (5)$$

For an isothermal atmosphere, the maximum meteor intensity can be calculated from the entry parameters and is approximately given by

⁹ F. L. Whipple, J. Geophys. Res., 68, p. 4929 (1963).

¹⁰ F. L. Whipple, G. S. Hawkins, "Meteors," Handbuch of Physik, (Springer, 1963) XLII, pp. 519-64.

¹¹ J. A. Ratcliffe, Physics of the Upper Atmosphere, (Academic Press, 1960) pp. 513-50.

$$F_{\max} = \frac{4}{9} \cdot \frac{V \cos\theta}{H} \int F dt, \quad (6)$$

where F_{\max} is the maximum meteor intensity, H is the scale height of the atmosphere, and θ is the angle of entry (counted from the zenithal direction).

The measurements of integrated and maximum meteor intensity are the main tasks of the proposed Meteor Flash Analyzer (MFA) apparatus. The ratio of the two measured parameters,

$$\frac{F_{\max}}{\int F dt} = \frac{4}{9} \cdot \frac{V \cos\theta}{H} \sec^{-1},$$

should be almost independent of meteor mass. Hence, it should be possible to determine a spectrum of s -values, from measured data of integrated and maximum meteor intensity, where

$$s = \frac{V \cos\theta}{H} \sec^{-1}. \quad (7)$$

Another parameter, r , involving the meteor mass can be derived as

$$r = \frac{H^3 m}{\cos^3 \theta} = 2 \left(\frac{4}{9} \right)^3 \cdot \frac{\int F dt}{\tau_0^*} \frac{\int F dt}{F_{\max}}^3. \quad (8)$$

Radiation data from terrestrial meteors are frequently presented in stellar photographic (visual) magnitude units. This system of units is practical and meaningful as long as the Earth's surface is used as an observational platform. For satellite-borne experiments on meteors, any one of the usual physical systems of units is more practical. For the following quantitative treatment for the orbital instrument design problem, we shall adopt the Gaussian cgs system of units. "Meteor intensity" shall henceforth be understood to measure the number of photons emitted per second into unit solid angle for a specified wavelength band, assuming the meteor to be a point source. For this quantity, the symbol $F'(\lambda_1; \lambda_2)$ has been chosen. The (dimensionless) conversion efficiency of meteor kinetic energy into optical radiation energy in the wavelength band $\langle \lambda_1; \lambda_2 \rangle$ is assumed to be $\tau_0 \cdot V$. The dimension of τ_0

is therefore sec/cm. There is some question at this time whether the meteor¹² efficiency may be assumed directly proportional to meteor velocity, V. However, in contemporary meteor radiation theory, this assumption is often considered valid, and is believed to be in agreement with ground-based observation of photographic meteors. We shall, therefore, adopt this assumption for the purpose of this discussion. Thereby, using the conservation of energy, Eq. (2) can immediately be rewritten in terms of photon flux and cgs-units as

$$\int F'(\lambda_1; \lambda_2) dt = \frac{\bar{\lambda} \cdot \tau_0(\lambda_1; \lambda_2)}{8\pi hc} mV^3 = A_{\lambda_1}^{\lambda_2} mV^3 = A_{\lambda_1}^{\lambda_2} rs^3 \frac{\text{photons}}{\text{sterad}} \quad (3a)$$

Equation (6) becomes

$$F'_{\text{max}}(\lambda_1; \lambda_2) = \frac{4}{9} A_{\lambda_1}^{\lambda_2} \cdot \frac{m \cdot V^4 \cdot \cos\theta}{H} = \frac{4}{9} A_{\lambda_1}^{\lambda_2} \cdot rs^4 \frac{\text{photons}}{\text{sec sterad}} \quad (6a)$$

Equations (6) and (7) remain unchanged. Therefore,

$$\frac{F'_{\text{max}}(\lambda_1; \lambda_2)}{\int F'(\lambda_1; \lambda_2) dt} = \frac{4}{9} \cdot s \text{ sec}^{-1} \quad ;$$

Equation (8) becomes

$$r = \frac{H^3 m}{\cos^3 \theta} = \frac{\int F'(\lambda_1, \lambda_2) dt}{A_{\lambda_1}^{\lambda_2}} \cdot \left(\frac{4}{9}\right)^3 \left(\frac{\int F'(\lambda_1, \lambda_2) dt}{F'_{\text{max}}(\lambda_1, \lambda_2)}\right)^3 \text{ gm cm}^3 \quad (8a)$$

In these equations, $h = 6.62 \times 10^{-27}$ ergs · sec; $c = 3 \cdot 10^{10}$ cm/sec; $\bar{\lambda}$ is a weighted "average" wavelength, characteristic of the meteor intensity distribution in time and wavelength, and of the wavelength band:

¹²J. F. Friichtenicht, J. C. Slattery, and E. Tagliaferri, "A Laboratory Measurement of Meteor Luminous Efficiency," TRW Systems Technical Report 05320-6005-R000, Submitted to NASA under Contract NASA-1336, December 1966, to be published in the Astrophysical Journal.

$$\bar{\lambda} = \frac{\int_t^2 \int_{\lambda_1}^{\lambda_2} F'(\lambda_1, \lambda_2) dt}{\int_t^2 \int_{\lambda_1}^{\lambda_2} dt d\lambda \frac{F'(\lambda, t)}{\lambda}} \text{ cm} .$$

Because the true meteor intensity function is not well-known, $\bar{\lambda}$ can only be approximately determined.

For using Equations (5a), (6a), (8a), the constants "A" have to be evaluated. This leads to the discussion of $\tau_0(\lambda_1, \lambda_2)$. In contemporary meteor radiation theory, the constant $\tau_0(\lambda_1, \lambda_2)$ is usually measured in terms of

$$[\tau_0^*] = [\text{zero photographic (visual) magnitude} \cdot \text{sec/gm (cm/sec)}^3] .$$

Meteor intensities in Equations (4) and (5) are measured in terms of a zero photographic magnitude meteor at a height of 100 km. Therefore,

$$\tau_0 = 4\pi \cdot 10^{14} \cdot I_0^* \cdot \tau_0^* ,$$

where I_0^* is the radiation power flux produced at the Earth's surface by a "zero magnitude" star in the photographic range $\lambda \lambda 0.30 \mu \leftrightarrow 0.45 \mu$. Whipple⁹ gives the value of τ_0^* for a stony meteor of zero photographic magnitude as

$$\log_{10} \tau_0^* = -18.7 \rightarrow \tau_0^* = 2 \times 10^{-19} \frac{\text{zero photographic magnitude} \cdot \text{sec}}{\text{gm} \cdot (\text{cm/sec})^3}$$

A zero photographic magnitude star yields an approximate irradiance level in the $< 0.30\mu ; 0.40\mu >$ wavelength range just outside the Earth's atmosphere of (we neglect color index differences between a photographic meteor and photographic star because the latter is not well-known)

$$I_0^* \sim 6 \times 10^{-6} \frac{\text{ergs}}{\text{cm}^2 \cdot \text{sec}} .$$

Hence,

$$\tau \begin{cases} 0.40\mu \\ 0.30\mu \end{cases} \approx 1.5 \times 10^{-9} \text{ sec/cm}$$

For a meteor of 20 km/sec, the efficiency follows approximately as

$$(\tau_0 \cdot V) \approx 3 \times 10^{-3} .$$

Independent laboratory measurements carried out in this laboratory on artificial micrometeorites directly yielded a value of 5×10^{-3} for 20 km/sec.¹⁰ Accounting for the concentration of iron in stony meteors and assuming that all the radiation comes from its iron content, this data would lead to a minimum value of 1×10^{-3} for stony meteors.

Verniani¹³ gives for τ_0 of photographic meteors the value of

$$\tau_0 = 5.25 \times 10^{-10} \text{ sec/cm} ,$$

which yields luminous efficiency of 0.001 for $V = 20$ km/sec. It appears, therefore, that a value of $\tau_0 = 5 \times 10^{-10}$ sec/cm is about the minimum value consistent with actual observations. For the purpose of the following discussion, we shall adopt this minimum value. Using τ_0 , the value for the constant "A" in Eq. (2a) can be evaluated readily. It is, for $\bar{\lambda} = 0.38\mu$,

$$A \begin{cases} 0.40\mu \\ 0.30\mu \end{cases} = \frac{\bar{\lambda} \cdot \tau_0}{8\pi \text{ hc}} = \frac{3.8 \times 10^{-5} \cdot 5 \times 10^{-10}}{8\pi \cdot 6.62 \cdot 10^{-27} \cdot 3 \cdot 10^{10}} = 3.8 \frac{\text{photons} \cdot \text{sec}}{\text{ergs} \cdot \text{sterad} \cdot \text{cm}} .$$

The corresponding constants for radiative efficiencies of meteors in the ultraviolet ranges from approximately $0.23\mu \leftrightarrow 0.30\mu$ are not known. One may well expect substantial radiation in the far ultraviolet band, both for stony and iron meteors. The reason for this is fairly straightforward. For

¹³F. Verniani, Smithsonian Contributions to Astrophysics, Vol. 8 , No. 5.

silicon, for example, the lowest excited state $4s^3P^o$ (4.9 eV), leads to radiation at 0.25μ . Magnesium resonance radiation is at $\lambda = 0.2852\mu$. A study of this problem for stony meteors has yielded for far UV channel the ratio of the efficiency constants, the range

$$0.5 < \tau = \frac{\tau_0 \left| \begin{array}{l} 0.26 \\ 0.23 \\ 0.45 \end{array} \right.}{\tau_0 \left| \begin{array}{l} \\ \\ 0.30 \end{array} \right.} < 2$$

For the purpose of estimating count rates in the far ultraviolet channel $<0.23; 0.26\mu>$ we choose in view of the above discussion, $\tau_0 = 2.5 \times 10^{-10}$ sec/cm and $\bar{\lambda} = 0.252\mu$. It follows that

$$A_{0.22}^{0.26} = \frac{2.52 \times 10^{-5} \cdot 2.5 \times 10^{-10}}{8\pi \cdot 6.62 \times 10^{-27} \cdot 3 \times 10^{10}} \approx 1.3 \frac{\text{photons.sec}}{\text{ergs.sterad.cm}}$$

For the intermediate channel $<0.26\mu; 0.30\mu>$ we use directly recent laboratory measurements conducted on artificial iron micrometeorites ignoring entirely the significant magnesium concentration in most meteors. Measurements suggest a value for τ_0 approximately 0.2 times the value for the photographic range which yields $\tau_0 \approx 1 \times 10^{-10}$.

Using $\lambda = 0.28\mu$,

$$A_{0.26}^{0.30} = \frac{2.8 \times 10^{-5} \cdot 10^{-10}}{8\pi \cdot 6.62 \times 10^{-27} \cdot 3 \times 10^{10}} \approx 0.56 \frac{\text{photons.sec}}{\text{ergs.sterad.cm}}$$

This derived constant A may be more than one order of magnitude too low.

3.2.2 The Background Radiation Environment

Meteor flashes from an orbital platform must be observed against a natural radiation background. We shall briefly list the important sources

of background radiation for terrestrial environment. It has become customary to measure intensities of nightglow and related phenomena in terms of rayleighs, R.¹⁴

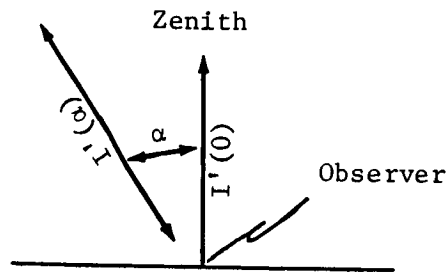


Figure 4. Definition of Nightglow Intensities $I'(0)$ and $I'(\alpha)$

Figure 4 defines the nightglow intensity, $I'(\alpha)$. It is

$$I'(\alpha) = \frac{I'(0)}{\cos \alpha} = \frac{R \cdot 10^6}{4\pi \cdot \cos \alpha} \frac{\text{photons}}{\text{cm}^2 \cdot \text{sec} \cdot \text{sterad}} \quad (9)$$

Therefore, $I'(0)$ and $I'(\alpha)$ describe the effective radiance (in terms of photons) of the background radiation field.

The most important source of terrestrial background radiation interfering with the MFA experiment is nightglow, because it cannot be avoided by choosing a proper experiment time. Other background radiation sources such as reflected moonlight and aurorae are in fact much stronger in intensity, but they can be eliminated by the timing of the experiment. It suffices to say here that both the full moonlight and aurorae would certainly render the long wavelength channel $0.30\mu \leftrightarrow 0.40\mu$ useless. Man-made sources of radiation can easily be excluded from interfering with the long wavelength channel by proper electronic filtering (see Reference 11). Lightning flashes will probably cause some interference on the long wavelength channel; whereas, the two far UV channels are entirely shielded by the Earth's ozone layer. The latter argument holds, of course, also for all man-made sources. Discussing the lightning flash problem, it is evident that the

¹⁴J. W. Chamberlain, "Physics of the Aurora and Airglow", Academic Press (1961).

latter might produce a signal on the visible channel, but never on the shielded UV channel. A bright meteor, on the other hand, is expected to trigger both visible and far UV channels.

Nightglow intensities are known to be subject to latitudinal, diurnal, annular, and secular variations. The data quoted in the following are, therefore, understood to be average values.

In the ultraviolet spectral region,¹⁵ the terrestrial airglow consists of

- 1) Ly- α : $\lambda = 0.1217 \mu$
- 2) OI: $\lambda = 0.2972 \mu$
- 3) O₂: $A^3\Sigma_a^+ \rightarrow X^3\Sigma_g^-$ (Hertzberg), $0 \leq V'' \leq 9$, $0.25 \mu \leftrightarrow 0.39 \mu$.

The Ly- α nightglow is of no interest here. As far as the ultraviolet nightglow is concerned, only the OI-0.2972 μ line and the O₂ - Hertzberg system need be considered. Table 2 gives data reported by J. P. Hennes.¹⁶ Hennes reported his data in rayleigh units which have been listed in Column 1. The second column lists the same data in terms of the quantity $I'(0)$, and the third column gives the integrated intensity from 0.25 μ up to wavelength λ ; i.e.,

$$\int_{0.25}^{\lambda} [I'(0) \cdot \Delta\lambda] .$$

From Hennes' data, we draw the following conclusions important for the design of the Meteor Flash Analyzer:

¹⁵Shea L. Valley, Scientific Editor, "Handbook of Geophysics and Space Environments, McGraw Hill Book Company, Inc., 1965.

¹⁶J. P. Hennes, J. Geophys. Res., 71, p. 763 (1966).

Table 2. Ultraviolet Nightglow Intensities

Wavelength Range [μ]	Zenith Emission Rate (rayleighs)	$I'(0)$ Photons $\frac{\text{cm}^2 \cdot \text{sec} \cdot \text{sterad}}{[10^6]}$	$\Sigma I'(0)\Delta\lambda$ Accuracy $\pm 50\%$ ¹² [10^6]
0.2511 - 0.2526	0.1	0.008	0.008
0.2555 - 0.2578	2	0.159	0.167
0.2578 - 0.2610	5	0.398	0.565
0.2610 - 0.2649	10	0.796	1.36
0.2649 - 0.2691	13	1.035	2.40
0.2691 - 0.2725	15	1.193	3.59
0.2725 - 0.2765	22	1.75	5.34
0.2765 - 0.2802	21	1.65	7.01
0.2802 - 0.2839	22	1.75	8.76
0.2839 - 0.2884	30	2.39	11.15
0.2884 - 0.2924	28	2.23	13.38
0.2924 - 0.2989	46	3.66	17.04
0.2989 - 0.3050	39	3.10	20.1
0.3050 - 0.3121	39	3.10	23.2
0.3121 - 0.3197	40	3.18	26.4
0.3191 - 0.3250	32	2.55	29.0
0.3250 - 0.3355	55	4.38	33.3
0.3355 - 0.3408	29	2.31	35.7
0.3408 - 0.3528	51	4.06	39.7
0.3528 - 0.3602	35	2.79	42.5
0.3602 - 0.3680	29	2.31	44.8
0.3680 - 0.3803	35	2.79	47.6
0.3803 - 0.3857	12	0.455	48.6

1) $\lambda < 0.253\mu$,	$I'(0) < 1 \times 10^4$	$\frac{\text{photons}}{\text{cm}^2 \cdot \text{sec} \cdot \text{sterad}}$
2) $\lambda < 0.258\mu$,	$I'(0) < 2 \times 10^5$	
3) $\lambda < 0.265\mu$,	$I'(0) < 1.4 \times 10^6$	
4) $\lambda < 0.284\mu$,	$I'(0) < 0.9 \times 10^7$	
5) $\lambda < 0.305\mu$,	$I'(0) < 2 \times 10^7$	
6) $\lambda < 0.305\mu \leq \lambda \leq 0.386\mu$,	$I'(0) \sim 2.9 \times 10^7$	

It is well-known that for background-determined detector noise, the signal/noise ratio is inversely proportional to $[I'(0)]^{1/2}$. Therefore, one expects, for constant signal, increase in signal/noise as the upper wavelength limit is reduced further. If it can also be shown that significant meteor radiation exists at the wavelength of the silicon resonance lines, then limiting the wavelength band to below $\lambda = 0.26\mu$, or even 0.253μ would yield significantly better signal/noise. Similarly, Mg 0.2852μ presents an argument for the intermediate wavelength channel.

The nightglow spectrum in the visible range between $0.40\mu \leftrightarrow 0.50\mu$ consists of

- 1) O_2 : $A^3\Sigma_u^+ \rightarrow X^3\Sigma_g^-$; $7 \leq v'' \leq 13$; $0.39\mu \leftrightarrow 0.48\mu$
- 2) OH: Meinel Bands ($v' \leq 9$)
- 3) Continuum

The origin of the continuum has never been clearly established.¹⁴ Atomic lines of the night glow begin to appear at wavelengths greater than 0.5577μ (forbidden OI). These are of no interest here because of the wavelength limitation on the Meteor Flash Analyzer apparatus. For background radiation discussion for a Martian mission see Reference 1.

3.2.3 Basic MFA Signal Channel Description

In order to further describe the experiment concept, it is necessary to discuss the fundamental features of the MFA signal channels. In Section 3.2.1 the meteor observables to be measured have been defined as $\int F'(\lambda_1; \lambda_2) dt$ and $F'_{\max}(\lambda_1; \lambda_2)$. We shall furthermore require the option of measuring the complete intensity vs. time dependence, $F'(\lambda_1; \lambda_2; t)$, of selected meteor flashes. This measurement will be used as control data; it must also be kept in mind that the aforementioned relations regarding meteor radiation have been proven only for

light accessible to ground-based radiation. Checking of the fundamental meteor radiation relations eqs. 2 and 3 in the far ultraviolet is therefore an important objective of the experiment. Finally, in view of the discussion of Section 3.2.2 a background radiation measurement is needed for critical assessment of the measurements signal/noise.

The three MFA signal channels are identical in design concept except for varying optical filters and detector choices. Figure 5 shows the schematic of the optical arrangement. A two-component quartz lens of 5 cm effective aperture collects the incident radiation. The aperture in the focal plane of the lens system determines the field of view (f.o.v.). Because of careful lens design an almost constant sensitivity over the entire f.o.v. is obtained which is followed by a very rapid sensitivity decrease at the edge of the f.o.v. The full f.o.v. angle is approximately 30° . The optical pass bands are selected by the filter combinations and the PM-tube sensitivity functions. Both far UV-channels employ EMR tube types 541A-05M-14 exhibiting almost constant quantum efficiency of approximately 10% in the wavelength range 0.2μ to 0.4μ and a Corning glass UV transmitting filter of the type 7-54. Each far UV-channel has one additional interference filter defining the two pass bands $0.23\mu \leftrightarrow 0.26\mu$ and $0.26\mu \leftrightarrow 0.30\mu$, respectively. The long wavelength channel, which has a pass band similar to the traditional photographic meteor range, has an EMR 541A-01-14 PM detector and a Corning 7-54 filter. This latter combination defines a pass band given approximately by the range $0.30\mu \leftrightarrow 0.40\mu$. The UV transmitting absorption filters employed in all optical channels fulfill the dual purpose of helping define the pass bands and to protect the sensors when exposed to back-scattered sunlight during orbiting. Direct exposure of the sensors to the back-scattered light from the Earth would damage the photomultipliers even though the high voltage is turned off when the spacecraft is on the earth's unlit side. All three MFA signal channels have been carefully aligned to view identical f.o.v. A calibration lamp included in the optical sensor package provides a valuable check and measure of any sensitivity changes experienced by the sensors during the mission.

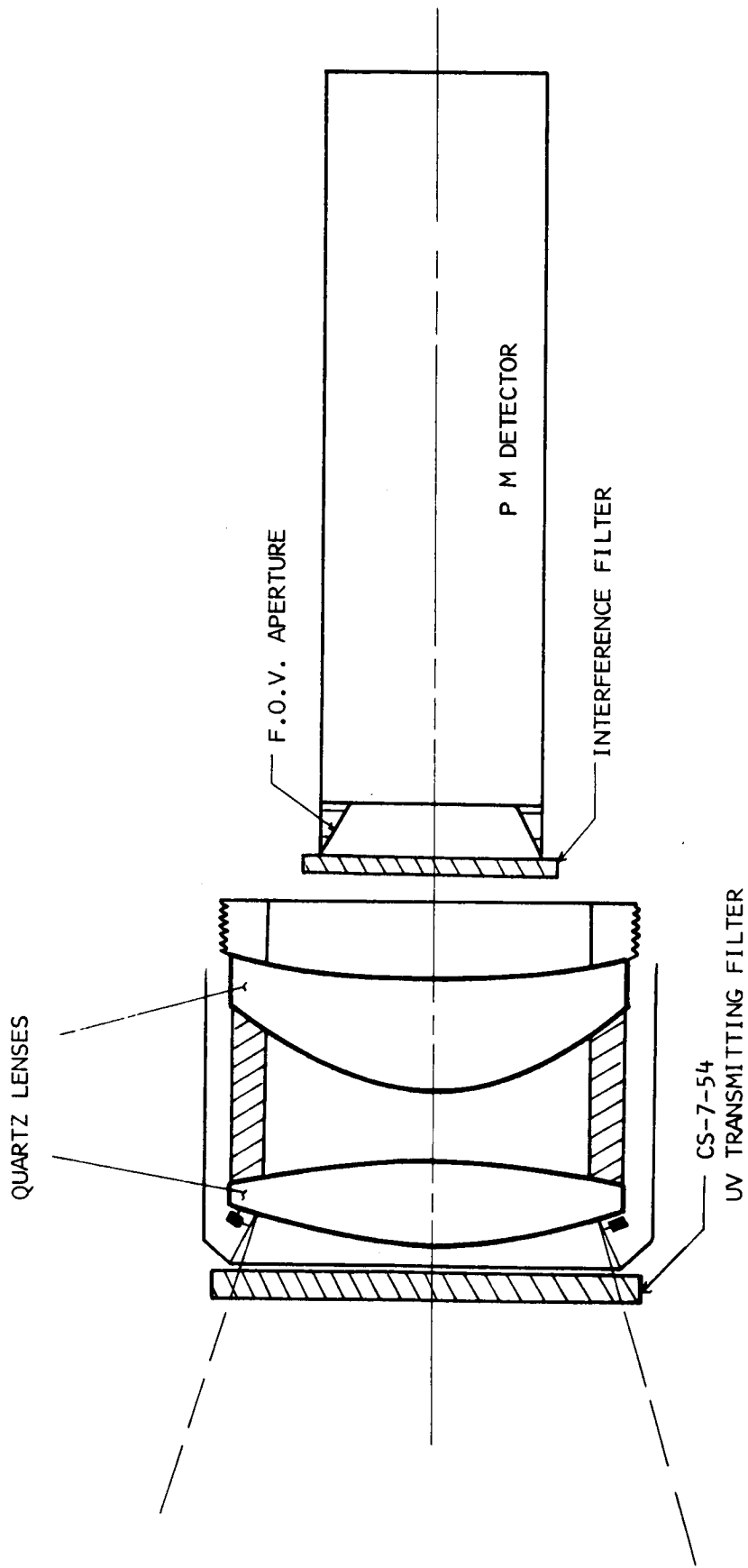


FIGURE 5 SIGNAL CHANNEL OPTICAL ARRANGEMENT

The basic block diagram of the signal channel electronics has been shown in Figure 12. The total signal from the PM detector consists of a slowly varying component originating from the background radiation field and occasionally of a superimposed meteor flash signal which varies relatively fast (approximately 1 sec. flash duration). As will be shown later, the total signal is dominated by the background. Therefore, the "background" amplifier which measures total PM signal, essentially records the background radiation intensity. The signal amplifier which is followed by a properly-dimensioned high and low pass filter rejects the background and passes only the meteor signal. However, the background signal will dominate the noise at the output of the signal amplifier - electronic filter combination. The noise problem will be discussed later. The meteor signal will be electronically processed to yield directly outputs proportional to integrated meteor intensity and maximum meteor intensity. The fourth data channel allows direct monitoring of signals proportional to the intensity vs. time variations of the meteor signals. Since there are three signal channels there are a total of 12 data channels of which 9 yield optical meteor data.

3.2.4 Signal/Noise Ratios and Detection Sensitivity

The strengths of the meteor observables $\int F'(\lambda_1; \lambda_2) dt$ and $F'_{\max}(\lambda_1; \lambda_2)$ has been given in Eqs. (5a) and (6a), respectively. For Earth orbit, expected background intensities (nightglow) have been discussed in Section 3.2.2. When this information is combined with the optical system's parameters and the characteristics of the detector and its electronics, the measurement problem is entirely defined. We shall use this discussion to aid in the selection of system's parameters.

Figure 6 defines the experimental geometry.

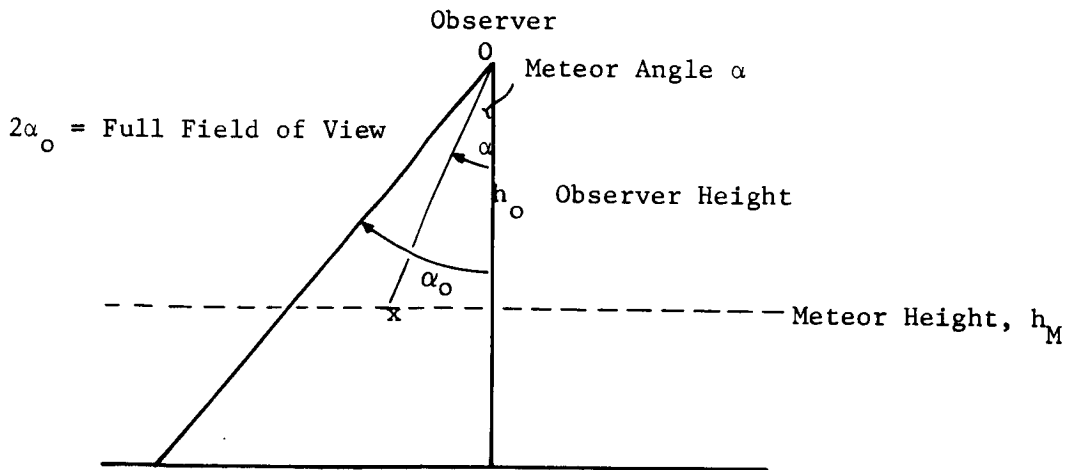


Figure 6. Experimental Geometry

It is necessary to distinguish between the observer's height, h_o , and the meteor height, h_M , all measured from the planet's surface. The optical axis of the detector is assumed to be pointed towards the planet's center. Let d stand for the effective collecting aperture of the lens, and let $2\alpha_o$ be the optical system's full field of view. Assume a meteor flash at an angle, α , from the optical axis.

The photocurrents excited by the meteor signal and the background intensity yield a composite signal

$$i_p(t) = i' + i''(t) \text{ amps ,} \quad (10)$$

where i' is the background signal (d.c.) and $i''(t)$ is the time-dependent meteor signal. The maximum meteor signal current is

$$i''_{\max} = \frac{\pi d^2}{4} \cdot \frac{\cos^2 \alpha}{(h_o - h_M)^2} \cdot \eta \cdot T \cdot G \cdot e \cdot F'_{\max} \text{ amps .} \quad (11)$$

The integrated meteor signal is

$$\int i''(t) dt = \frac{\pi d^2}{4} \frac{\cos^2 \alpha}{(h_o - h_M)^2} \cdot \eta \cdot T \cdot G \cdot e \cdot \int F' dt \text{ coulombs .} \quad (12)$$

The background signal current is readily found as

$$i' = \pi^2 d^2 \cdot \sin^2 \frac{\alpha_o}{2} \cdot \eta \cdot T \cdot G \cdot e \cdot I'(o) \text{ amps .} \quad (13)$$

It is interesting to note that the background signal current is independent of detector height. The background signal current is the primary source of systems noise, at least for wavelengths longer than 0.26μ . The rms noise voltage across the PM anode resistor, Ω , is

$$\bar{V} = \Omega \cdot a \cdot \sqrt{2 eG \Delta f \cdot i'} \text{ volts .} \quad (14)$$

The signal/noise ratio, N, for maximum signal follows as

$$N = \frac{\Omega \cdot I''_{\max}}{\bar{V}} = \frac{1}{2^{5/2}} \frac{d \cdot \cos^2 \alpha \cdot \sqrt{\eta} \cdot T}{(h_o - h_M)^2 \cdot \sin^{\alpha_o/2} \cdot a \cdot \sqrt{\Delta f}} \cdot \frac{F'_{\max}}{\sqrt{I'(o)}} \quad (15)$$

Here, η is detector quantum efficiency, G is detector photomultiplier gain, T is total optical system's transmission, a is secondary emission noise enhancement factor ($a = 1.2$) and Δf is detector electronics bandwidth. From a point of view of data analysis, it is practical to eliminate the dependence of maximum signal current on meteor angle, α , because this dependence produces additional uncertainties in data analysis. This can be accomplished by introducing an absorption filter such that the rays coming from the central regions of the field of view are more strongly attenuated than the rays coming from the edge. Considering Eqs. (11) and (12) it is clear that the filters should attenuate as

$$T(\alpha) = \frac{T_o}{\cos^2 \alpha}.$$

Such a filter could be placed in front of the PM - photocathode. The difficulty lies in the fact that relative filter attenuation, $T(\alpha)$, should be independent of wavelength over the considered optical band. This poses problems in the ultraviolet. In practice, an absorption filter appears to be hardly worthwhile if we consider the effect of the $\cos^2 \alpha$ - factor on the measurements for relatively small field of view angles. The error is further reduced if we assume for $\cos^2 \alpha$ an average value following from statistics as

$$\overline{\cos^2 \alpha} = \frac{1}{2} (1 + \cos^2 \alpha_o).$$

Minimum detectable signals can now be easily found by combining Eqs. (5a), (6a), and (15). One verifies easily that

$$F'_{\max} = \frac{4}{9} A_{\lambda_1}^{\lambda} \cdot rs^4 \geq \frac{2^{5/2} \cdot a \cdot \sqrt{\Delta f} \cdot (h_o - h_M)^2 \cdot \sin^{\alpha_o/2}}{d \cdot \cos^2 \alpha \cdot \sqrt{\eta T}} \cdot \sqrt{I'(o)} \Big|_{\lambda_1}^{\lambda_2} N \quad (16)$$

This equation expresses the "selection effect" encountered in optical meteor detection. The latter obviously favors the detection of fast meteors. Equation (16) states the necessary condition that a meteor peak signal will be recorded with minimum signal/noise N . In order to determine expected meteor count rates, it is only necessary introduce the abundance of meteors where F'_{\max} exceeds the value given by the equality sign in Equation (16). For terrestrial meteors, it is practical to re-introduce for F'_{\max} photographic magnitudes F_{\max} because the well-known Flux-magnitude relation of Hawkins and Upton¹⁷ can be directly applied. The latter states:

$$\log_{10} M' = 0.537 m_{pg} - 4.33 \frac{\text{meteors} > m_{pg}}{\text{km}^2 \text{ hr}} \quad (17)$$

By definition

$$- m_{pg} = 2.5 \cdot \log_{10} \frac{F_{\max}}{I_0} \quad (18)$$

where I_0 is the intensity of a zero photographic magnitude meteor at the Earth's surface (see Section 3.2.2). Combining Equations (17) and (18) and measuring count rates per cm^2 area and second time interval, one finds

$$M' = \frac{1.3 \times 10^{-18}}{(F_{\max}/I_0)^{1.34}} \frac{\text{meteors} > F_{\max}}{\text{cm}^2 \text{ sec}}$$

A meteor detector at height, $h_0 - h_M$, above the meteors and covering full field of view $2\alpha_0$ surveys an area of size approximated by

$$A = \pi \cdot (h_0 - h_M)^2 \cdot \text{tg}^2 \alpha_0 \text{ cm}^2$$

Hence the total count rate is

$$M_t = \frac{4.08 \times 10^{-18}}{(F_{\max}/I_0)^{1.34}} \cdot (h_0 - h_M)^2 \cdot \text{tg}^2 \alpha_0 \cdot \frac{\text{meteors} > F_{\max}}{\text{sec}} \quad (19)$$

¹⁷ Hawkins, G. S. and Upton, E. K. L., "The Influx Rate of Meteors in the Earth's Atmosphere", *Astrophysical Journal*, Vol. 128, No. 3, pp 727-735, 1958.

In order to apply Equation (16) one needs only to recall that

$$F'_{\max} = \frac{F_{\max}}{I_o} \cdot \frac{I_o^*(\lambda_1; \lambda_2) \bar{\lambda}}{hc \cdot 10^{-14}} \frac{\text{photons}}{\text{sec sterad}} \quad (20)$$

where $\omega = 10^{-14}$ sterad is the solid angle subtended by 1 cm^2 of the earth's surface at the standard meteor height of 100 km. The ratio F_{\max}/I_o refers strictly to the meteor magnitude on the photographic scale as defined in Equation (18) even when considering meteor intensities in the far UV channels. The parameter $I_o^*(\lambda_1; \lambda_2)$ is the irradiance (watts/cm^2) generated at the Earth's surface by a zero photographic magnitude meteor and $\bar{\lambda}$ is an average wavelength, characteristic of the channel optical pass band and the meteor intensity distribution.

Combining Equation (16) with Equations (19) and (20), the total meteor count rate is

$$M_t = 4.08 \times 10^{-18} \left[\frac{I_o^*(\lambda_1; \lambda_2) \cdot \bar{\lambda} \sqrt{\eta T}}{hc \cdot 10^{-14} \sqrt{I'(o)}} \frac{\cos^2 \alpha d}{N \cdot 2^{5/2} a \sqrt{\Delta f}} \right]^{1.34} \frac{t_g^2 \alpha_o}{(h_o - h_M)^{0.68} (\sin \alpha_o / 2)^{1.34}} \frac{\text{meteors}}{\text{sec}} \quad (21)$$

The factors $I_o^*(\lambda_1; \lambda_2)$, $\bar{\lambda}$, $\sqrt{\eta T}$ and $\sqrt{I'(o)}$ depend on the optical wavelength channel. For the photographic channel (using $\bar{\lambda} = 0.38\lambda$)

$$\frac{I_o^*(\lambda_1; \lambda_2) \bar{\lambda}}{hc \cdot 10^{-14}} = \frac{6 \times 10^{-6} \cdot 3.8 \times 10^{-5}}{6.62 \times 10^{-27} \cdot 3 \times 10^{10} \cdot 10^{-14}} = 1.15 \times 10^{10} \frac{\text{photons}}{\text{sec sterad}}$$

Here we assumed a value for I_o^* equal to that of a zero photographic magnitude star (see discussion of Section 3.2.1). For the far UV channels the corresponding factors should have relative values corresponding to the $A_{\lambda_1}^{\lambda_2}$ parameters discussed in Section 3.2.1. Table 3 combines estimated numerical values for the wavelength dependent parameters in Equation (21).

*MgI - resonance radiation has been neglected.

Table 3

Channel	$\bar{\lambda}$ [μ]	$\frac{I_o^*(\lambda_1; \lambda_2) \bar{\lambda}}{hc \cdot 10^{-14}}$ photons/sterad sec	$I'(o)$ photons/cm ² sec sterad	$\sqrt{I'(o)}$	$\sqrt{\eta T}$
0.30 μ - 0.40 μ	0.38	1.15×10^{20}	3×10^7	5.48×10^3	0.32
0.26 μ - 0.30 μ	0.28	$0.17 \times 10^{20} *$	2×10^7	4.47×10^3	0.32
0.22 μ - 0.26 μ	0.252	0.373×10^{20}	2×10^5	4.47×10^2	0.23

The limiting (photographic) magnitude of detectable meteors for the various channels follows immediately from combining Eq. (18) with Eqs. (16) and (20).

$$-m_{PG} = 2.5 \log_{10} \left[\frac{hc \cdot 10^{-14} \cdot \sqrt{I'(o)}}{I_o^*(\lambda_1; \lambda_2) \bar{\lambda} \cdot \sqrt{\eta T}} \frac{2^{5/2} a \sqrt{\Delta f} \cdot N}{d \cos^2 \alpha} (h_o - h_M)^2 \sin \alpha_o / 2 \right] \quad (22)$$

photographic magnitudes

3.2.5 Predicted Meteor Count Rates and Observable Meteor Magnitudes

Meteor count rates and observable meteor magnitudes can be predicted approximately by using Eqs. (20) and (21). The approximate nature of the predictions relates primarily to uncertainties in exact meteor spectral radiance distribution. At the present time, the only applicable data for the spectral range below 0.30 μ comes from laboratory experiments on simulated micrometeorites. The application of this laboratory data to real meteors involves, however, assumptions regarding scaling.

It is useful to briefly consider the dependence of meteor count rates and observable magnitudes as function of MFA collecting lens diameter, d , full field of view, $2\alpha_o$, and orbital altitude, $h_o - h_M$. The effect of lens diameter is to change meteor count rates proportional to $d^{1.34}$. The dependence on field of view angle is slightly more complicated. For angles of practical interest, however, the approximation

$$\frac{\text{tg}^2 \alpha_o}{\text{Sin}(\alpha_o/2)^{1.34}} \approx 2.53 \cdot \alpha_o^{0.68}$$

is useful. It shows that meteor count rates vary relatively slowly with increasing f.o.v. Similarly, meteor count rates are inversely proportional to $(h_o - h_M)^{0.68}$; i.e., small orbital altitude changes are not expected to drastically affect meteor count rates.

We shall apply Eqs. (21) and (22) to two cases of practical interest. The first case takes reference to an orbital altitude of $h_o = 600$ nautical miles as planned for the Nimbus E mission. The corresponding value for ($h_M = 90$ km)

$$h_o - h_M = 1,020 \text{ km}$$

The second case for which numerical values will be presented is for

$$h_o - h_M = 132 \text{ km}$$

The latter would correspond to an orbital altitude of 120 nautical miles. Many of the lower orbits are in this altitude range. Besides, by comparing the numbers for the two cases, the altitude effects can be most clearly demonstrated.

The presently available MFA prototype apparatus has the following characteristics:

Collecting lens effective diameter	$d = 5 \text{ cm}$
Collecting lens full field of view	$2\alpha_o = 30^\circ$
Electronic detector bandwidth	$\Delta f = 4 \text{ Hz}$
	$\frac{2}{\cos^2 \alpha} = 0.966$

Table 4 gives numerical values for count rates and limiting photographic magnitudes for the three MFA signal channels for $h_o = 600$ nautical miles. Table 5 gives the corresponding numbers for $h_o = 120$ nautical miles.

Table 4. Meteor Count Rates and Limiting Magnitudes for $h_o = \text{Nautical Miles}$

Channel	Meteor Count Rate Mt sec^{-1}	Inverse Count Rate Minutes/Meteor	Limiting Photographing Magnitude
0.30 μ ↔0.40 μ	3.0×10^{-3}	22.0	- 1.09
0.26 μ ↔0.30 μ	$3.0 \times 10^{-4} *$	220.0	- 2.95
0.22 μ ↔0.26 μ	1.2×10^{-2}	5.4	+ .05

* MgI resonance radiation has been neglected.

Table 5. Meteor Count Rates and Limiting Magnitudes for $h_o = 120 \text{ Nautical Miles}$

Channel	Meteor Count Rate Mt sec^{-1}	Inverse Count Rate Minutes/Meteor	Limiting Photographic Meteors Magnitude
0.30 μ - 0.40 μ	7.6×10^{-4}	5.6	3.3
0.26 μ - 0.30 μ	$7.6 \times 10^{-5} *$	55.0	1.45
0.22 μ - 0.26 μ	3.1×10^{-3}	1.4	4.45

* MgI resonance radiation has been neglected

3.2.6 Expected Background Signal Strengths in Earth Orbit

Count rates and limiting photographic meteor magnitudes in earth orbit have been discussed and numerical values have been presented in Section 3.2.4 and Section 3.2.5. Both count rates and limiting magnitudes depend on altitude. According to Eq. 13, PM-tube signals excited by the background are independent of detector altitude within the approximation used for the derivation of the equation. Table 6 gives approximate numerical values.

Table 6. Background Signal Currents

Channel	Background Signal Current
0.30 μ - 0.40 μ	$\sim 2.1 \times 10^{-6}$ amps
0.26 μ - 0.30	$\sim 1.5 \times 10^{-6}$ amps
0.23 μ - 0.26	$\sim 0.7 \times 10^{-8}$ amps

3.3 METHODS FOR CARRYING OUT AN ORBITAL MFA EXPERIMENT

The methods and procedures for carrying out the planned experiment depend in part on some basic optical and electronic features of the apparatus. Therefore, the discussion of the experiment procedure in Section 3.3.3 will be preceded by a brief description of the essential features of the apparatus in Sections 3.3.1 and 3.3.2. This description is limited in scope because a more detailed discussion follows in Section 4.

The presently available MFA prototype consists of two packages referred to in the following as the Sensor Assembly and the Electronics Assembly. The two assemblies are connected by a flexible cable of ample length. The Sensor Assembly must be mounted such that an unobstructed 30° f.o.v. in the direction of the Earth is provided. The Electronic Assembly box can be placed in any convenient location inside the spacecraft. Weight and size of the MFA assemblies are as follows:

Sensor Assembly:	8.75" x 6.25" x 6.25"	Weight 8.32 lbs.
Electronic Assembly:	7.5" x 7.5" x 6.625"	Weight 6.19 lbs.

3.3.1 The Sensor Assembly (Figures 7, 9)

The Sensor Assembly combines the detectors and associated optics for the three optical data channels and a fourth channel for monitoring the background intensity. The latter channel consists of a photoemissive diode of large dynamic range and associated optics; it protects the sensor channels against excessive illumination levels and provides automatic turn-on and turn-off

during orbiting. This feature permits the instrument to operate, after initial activation, without attention from the ground. The Sensor Assembly also contains the calibration lamp needed for monitoring any sensitivity changes of the channels. Aside from the optical components and the detectors, the Sensor Assembly contains the signal preamplifiers and the high voltage supplies for the PM tubes and the calibration lamp.

The four optical channels are aligned to cover nearly identical fields of view. The basic optical design of an individual MFA radiometer channel has been discussed in Section 3.2.3.

3.3.2 Basic Description of the Detector Electronic System

Most of the electronic circuitry of the MFA is contained in the electronic assembly. Principal exceptions are power supplies for operating sensors, calibration lamp, and signal preamplifiers which must be located near the sensors. The discussions of this section will concentrate on the essential features of the electronic system necessary to explain the experiment methods and procedures. Further electronic design details are provided in Section 4. Figures 18 and 19 show the electronic assembly.

We refer first to Figure 11 of Section 4 showing the Block Diagram of the basic signal channel. The total photomultiplier signal is fed to a preamplifier of low output impedance. This preamplifier is located in the optical sensor assembly box. Its purpose is to provide proper signal power and impedance to permit the signal to pass via the cable to the electronic assembly, where it is fed into two different input amplifiers. The total photomultiplier signal consists of a very slowly-varying background radiation signal with the meteor signals superimposed. Since the background signal is expected to be much larger than the meteor signal one of the two amplifier channels is used to condition the total photomultiplier signal, thereby recording essentially the background.

In the second amplifier channel a high and low pass filter are used to pass only meteor-like signals. The properly conditioned meteor signals from the output of this channel are electronically processed to yield the integrated and peak

amplitude signals. The second amplifier channel also has a direct output for recording the intensity-time function of the meteor signal by filtering out the dc photocurrent component. This latter data will be employed primarily for checking integrated and peak signals. Measurement of the intensity vs. time meteor signal in the two far ultraviolet channels will also provide new information on the nature of far UV meteor radiation.

The electronic system of the MFA will perform a number of additional functions designed to power the apparatus and to facilitate the task of taking the desired data. These functions are best described by referring to the Block Diagram, Figure 10, of Section 4. The power conversion unit conditions the power to operate the various MFA components using 28-volt dc power assumed to be available from the spacecraft. The light protection circuit will greatly facilitate the execution of the MFA experiment. It is designed to protect the signal channel from damage due to excessive illumination levels and to provide automatic instrument turn-on and turn-off while in orbit. The protection circuit functions as follows: The large dynamic range photoemissive diode provides a signal proportional to the total radiative flux incident on the MFA. The protection channel f.o.v. is identical to that of all the signal channels; the optical filter bandwidth and photocathode sensitivity is made to be nearly identical to that of the long wavelength signal channel, because, under all conditions likely to occur during the experiment, the long wavelength channel will always be first subjected to excessive illumination. When the photodiode signal exceeds a certain level, the high voltage feeding the PM tubes is turned off, thereby preventing damage to the tubes. After the photodiode signal has subsided below a predetermined level, the high voltage is again turned on. There are also provisions to protect the PM tubes during initial activation of the experiment. After turn-on, the photodiode channel will first monitor the background. PM-tube voltage will only be supplied when the photodiode signal indicates safe illumination levels.

3.3.3 Method for Carrying Out the MFA Experiment

In the preceding Section 3.2 the observables to be measured by the MFA have been defined as (1) maximum meteor intensity, F'_{\max} , (2) integrated meteor

intensity, $\int F' dt$, and (3) background radiation intensity, I' . This data is planned to be obtained simultaneously in three wavelength bands which have been defined earlier (Section 2.2). In addition to the measurements objectives (1), (2), and (3) it is planned to record complete intensity vs. time data of selected meteors.

The experiment has to be performed from an orbiting platform in order to eliminate the disturbing effects of the Earth's ozone. Terrestrial meteors appear at an average height above ground of 90 km. Expected count rates for the purpose of this proposal, we shall assume spacecraft and limiting magnitudes have been estimated for two altitudes above ground; namely 1020 km (600 nautical miles) and 222 km (120 nautical miles). It has been shown (Section 3.2.5) that expected meteor count rates do not depend very critically on spacecraft altitude. Therefore the actual spacecraft altitude variations are not considered critical.

The experiment method is to point the wide field of view, three-channel radiometer straight down towards the dark Earth or planet. The radiometer is expected to sense the meteor radiation against the planet's background (nightglow), and the radiometer electronics will record electrical quantities proportional to meteor observables, F'_{\max} , $\int F' dt$, background intensity, I' and meteor intensity $F'(t)$. The proportionality constants are assumed to be known because of suitable ground and in-flight sensor calibration. The data will be telemetered to the ground station.

Major limitations on the data collecting ability of the MFA are imposed by (1) available meteor intensities, and (2) terrestrial background intensities (nightglow). The requirements of a spacecraft-borne experiment impose major restrictions on permissible weight and size of the experiment package. These spacecraft-imposed restrictions are mostly reflected in the chosen size (5-cm diameter) of the radiometer light-collecting aperture which determines the instrument sensitivity.

Aside from the three radiometer sensor channels, the experiment package includes an in-flight calibration lamp and a fourth radiometer channel designed to protect the radiometer sensor channel against damage from excessive background illumination levels as will be discussed in Section 4. The in-flight calibration

lamps are intended to check for major changes in sensor channel calibration during flight. This check which is planned to be performed every five minutes during the data taking experiment period, is completely automated.

4. APPARATUS DESCRIPTION

4.1 MECHANICAL AND NECESSARY EQUIPMENT

A general description of the apparatus has been presented in Section 3.3. Detailed drawings will be made available separately. A prototype model of the MFA has been built and functionally tested. We do not expect any major design changes to be required to produce flight hardware for the Nimbus E Mission. Some reduction in weight and volume from the values for the present prototype will be possible, although it is not believed necessary at this time for the Nimbus.

The mechanical configuration of the available MFA prototype is shown in the photographs, Figures 7, 8, and 9. Weight, size figures, and power requirements have been presented in Tables 6 and 7.

TABLE 6
WEIGHT AND SIZE (MAXIMUM VALUES)

EQUIPMENT ITEM	MAXIMUM WEIGHT LBS.	MAXIMUM VOLUME CUBIC INCHES	MAXIMUM DIMENSIONS INCHES	SHAPE
Sensor Assembly	8.32	342	8.75 x 6.25 x 6.25	Rectangular
Electronics Assembly	6.19	373	7.5 x 7.5 x 6.625	Rectangular

TABLE 7
POWER

	STANDBY	AVERAGE	MAXIMUM (DURING CAL. CYCLE)
Total Power	3.0 Watts	7.5 Watts	9.5 Watts

Accessory test equipment consists of an electronic meteor flash simulator to stimulate the electronics shown in Figure 10.

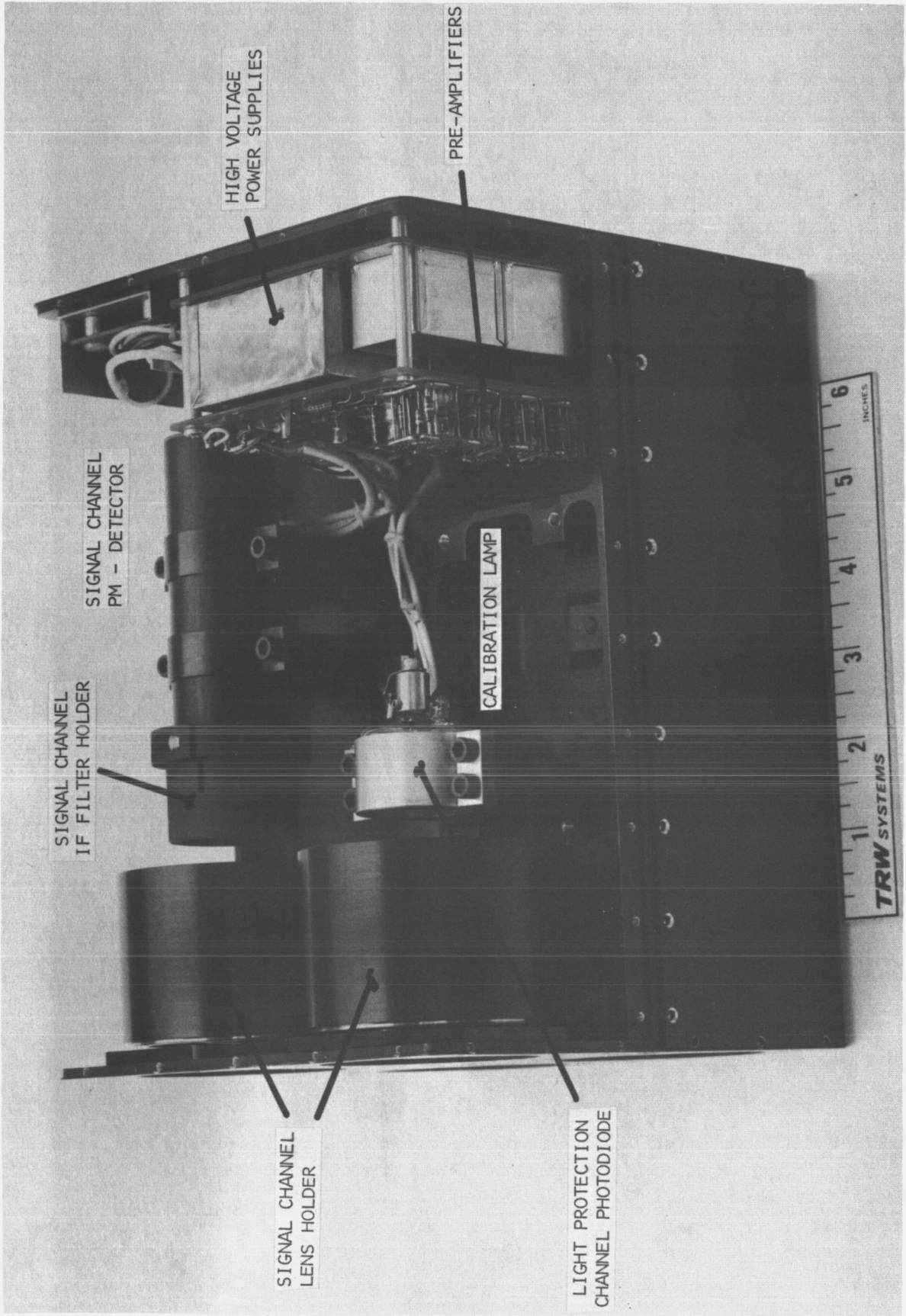


FIGURE 7. SENSOR ASSEMBLY (COVER REMOVED)

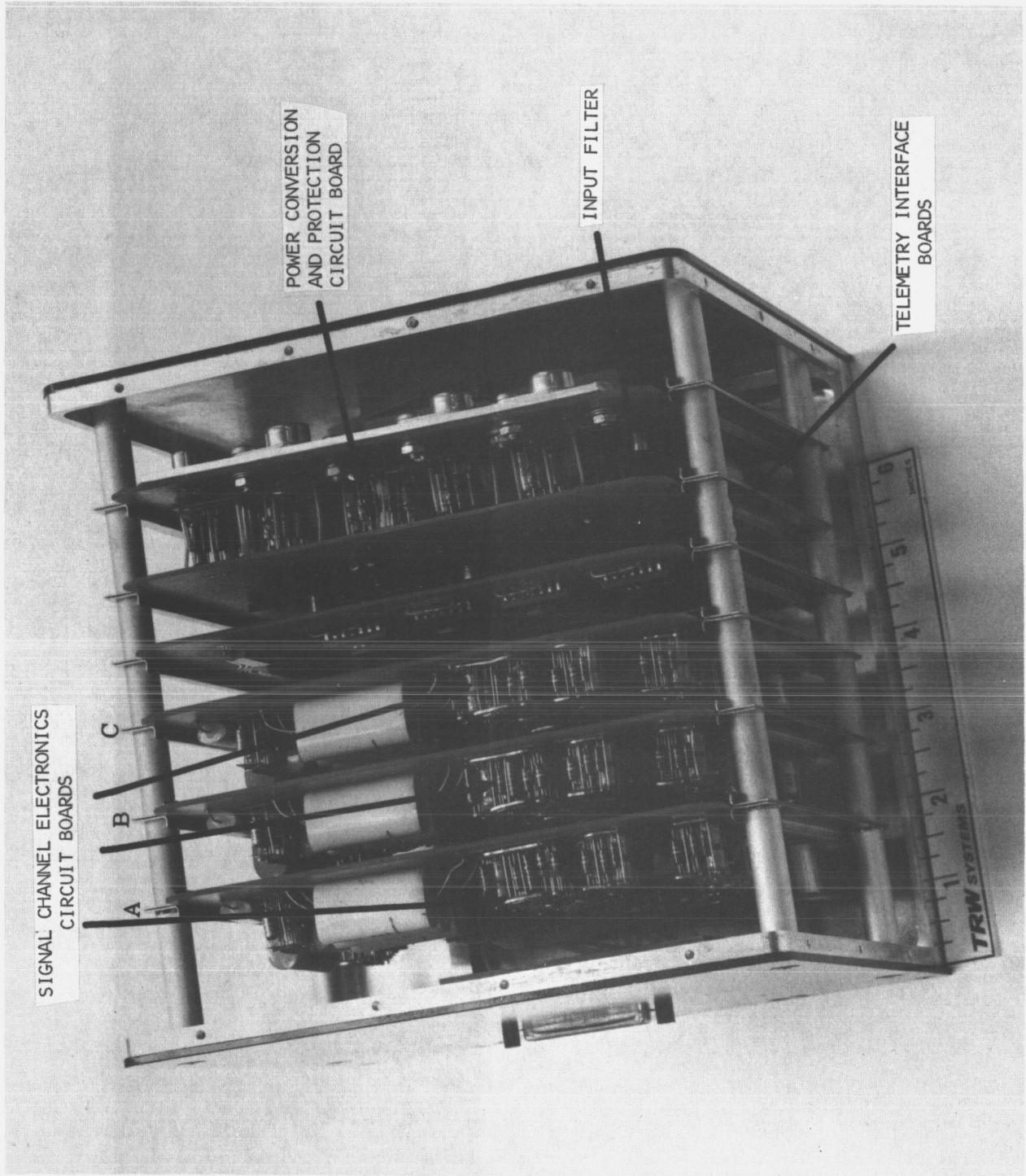
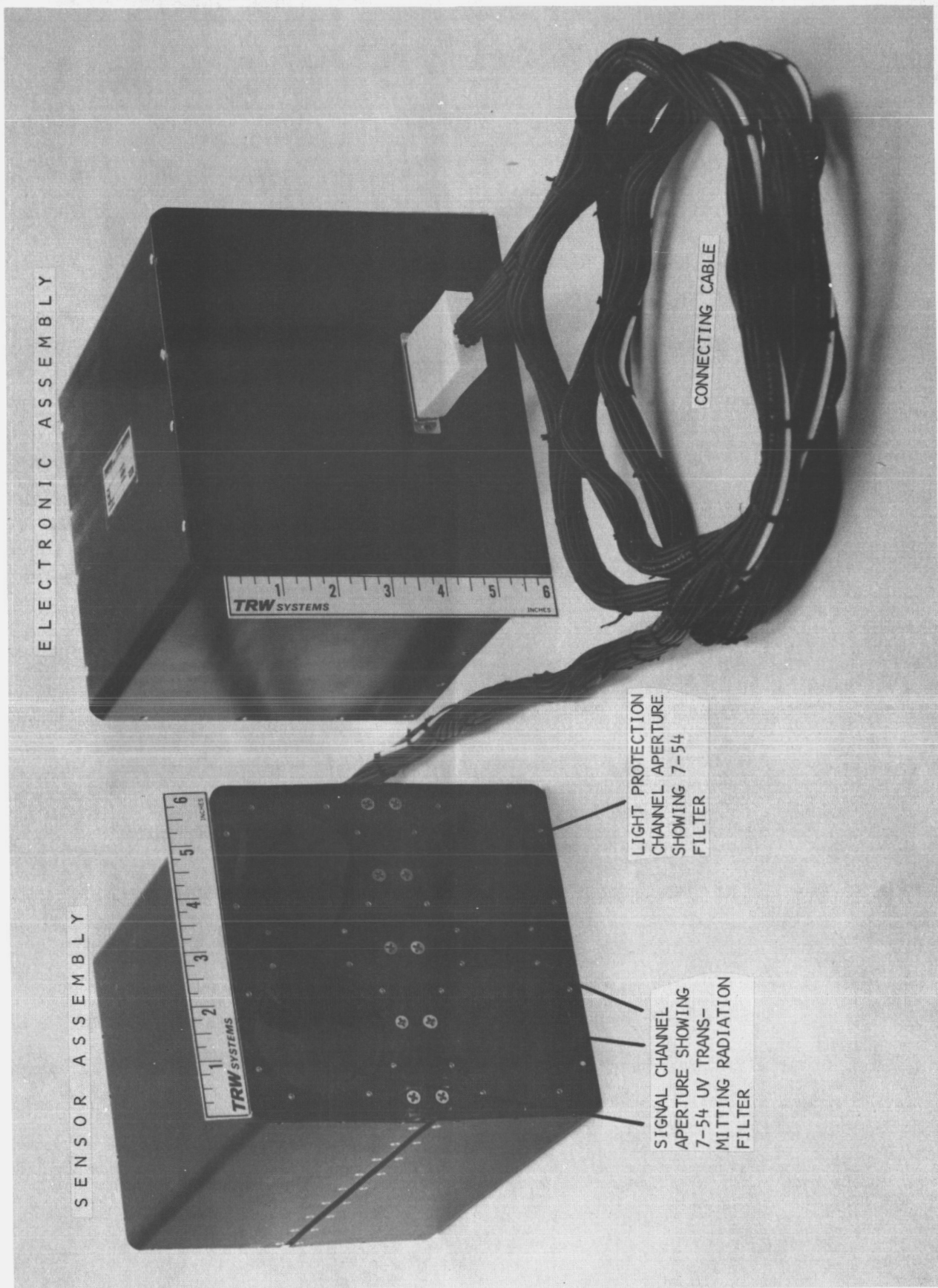


FIGURE 8. ELECTRONIC ASSEMBLY (COVER REMOVED)



ELECTRONIC ASSEMBLY

SENSOR ASSEMBLY

TRW SYSTEMS
INCHES

TRW SYSTEMS
INCHES

CONNECTING CABLE

LIGHT PROTECTION
CHANNEL APERTURE
SHOWING 7-54
FILTER

SIGNAL CHANNEL
APERTURE SHOWING
7-54 UV TRANSMITTING
RADIATION
FILTER

FIGURE 9. FULLY ASSEMBLED METEOR FLASH ANALYZER WITH CONNECTING CABLE

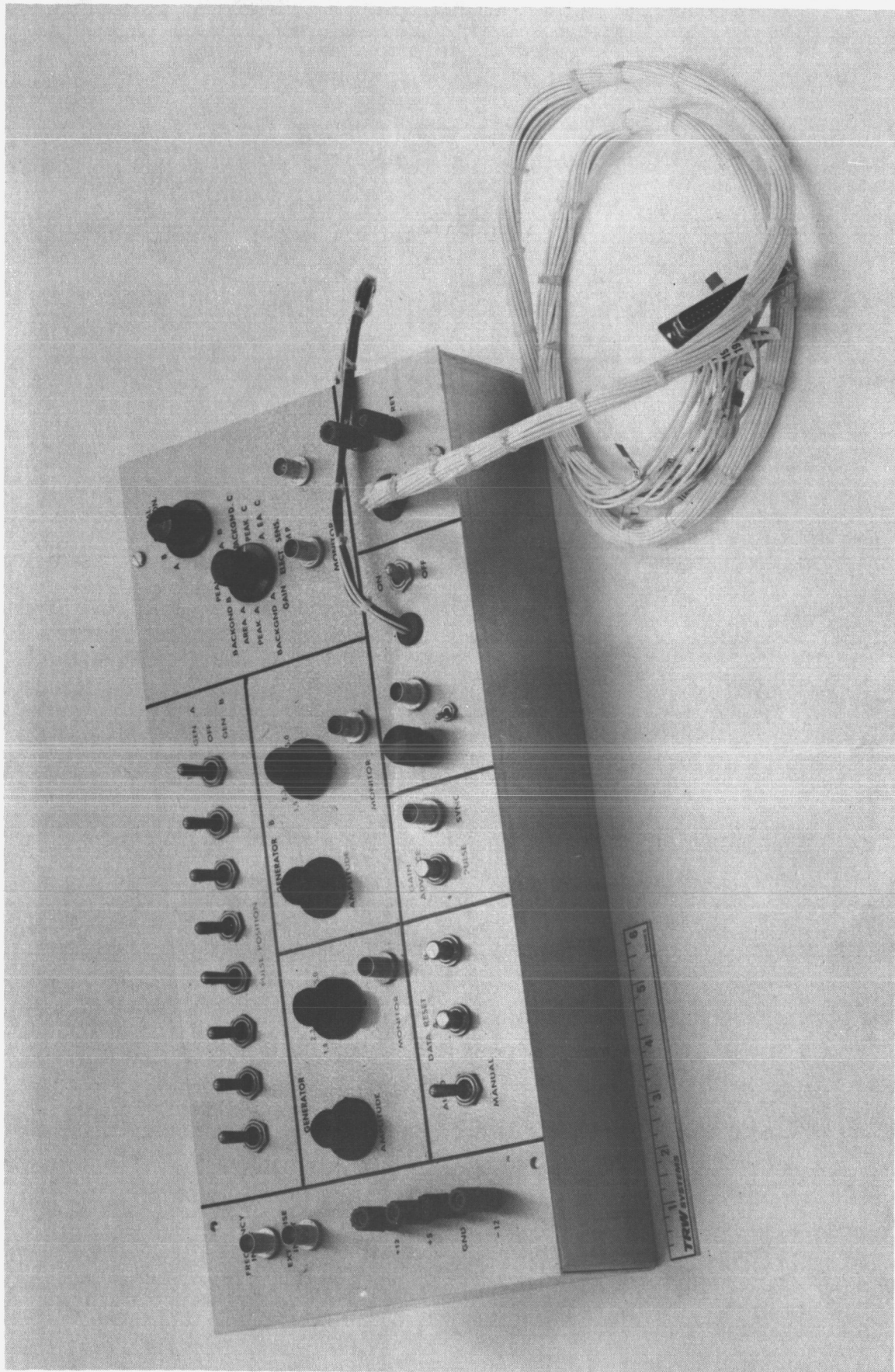


FIGURE 10. EXPERIMENT TEST SET UNIT

4.2 ELECTRONIC SYSTEMS DESCRIPTION

The purpose of this electronic system is to condition the PM-tube signals generated from meteor flashes observed from a satellite orbiting a planet and to power the experiment. The analysis consists of the measurement of the peak and the integral (area) of the meteor flash intensity wave form.

4.2.1 Basic System

The basic system block diagram is shown on Figure 11. The salient features of its subsystem blocks are summarized below.

- (1) The system contains three signal channels. The channels process the signals and temporarily store the signal peaks and integral values for the satellite telemetry system. The channels also monitor the background intensity incident on their photomultiplier. The data outputs are analog voltage amplitudes.
- (2) The telemetry interface subsystem contains circuitry to reset the signal channel temporary storage after the data has been "read" by the telemetry. It also can change any signal channel gain ± 10 db via a ground station impulse command. An analog output voltage indicates the channel gain.
- (3) A photoemissive diode sensor is used to protect the signal photomultiplier tubes. If the incident light is too high, the voltage to the signal PMTS is turned off. Also, an analog voltage output is used to indicate the system temperature.

4.2.2 Summary System Specifications

4.2.2.1 Signal PMTS

(1) Signal

- (a) Wave shape: Exponentially rising pulse with fast fall
- (b) Duration: 0.2 to 0.7 sec. at the $1/e$ amplitude point
- (c) Maximum Data Rate: 0.22 to 0.26 μ channel = 1 per 20 sec.
0.26 to 0.30 μ channel = 1 per 20 sec.
0.31 to 0.45 μ channel = 1 per 20 sec.
- (d) Amplitude: 2.5×10^{-9} amps to 1.3×10^{-6} amps

NOTE: The system is designed to handle an extra ± 10 db amplitude range.

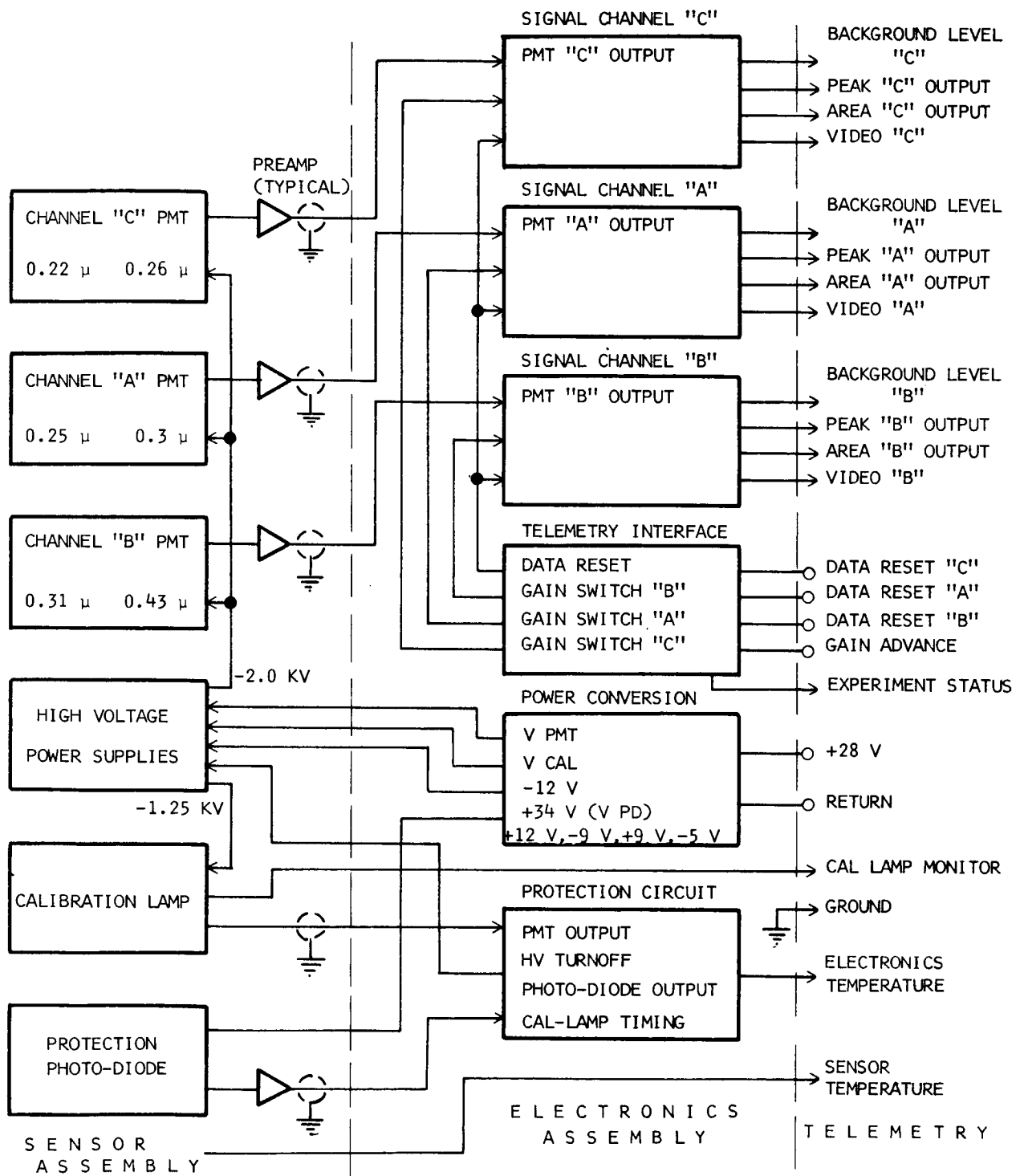


Figure 11. BASIC BLOCK DIAGRAM METEOR FLASH ANALYZER

4.2.2.2 Noise

- (1) PMT $\approx 0.5 \times 10^{-9}$ amps peak-to-peak
- (2) External Noises
 - (a) Lightning ≈ 0.2 sec. duration
 ≈ 2.5 cps
 - (b) Nightglow, moonlight, patchiness of the night sky, etc.
(See Table II-5.)

4.2.2.3 Protection Sensor

- (1) Photodiode
 - (a) Trigger signal = 1×10^{-10} amps
 - (b) Noise level = 1×10^{-12} amps
- (2) Input transient. When the signal PMTS are turned on, a high ambient light condition will occur. This will not exceed twice the nightglow amplitude and will decay to the nightglow within 1.5 minutes.

4.2.2.4 Telemetry Outputs

- (1) Basic Characteristics
 - (a) Analog words
 - (b) Amplitude 0 - 6.4 V
 - (c) Source impedance \approx 1K. Except for the following outputs:
 - 1 Temperature sensors
 - 2 Calibration on monitor \approx 2K
 - (d) Expected load. $R_L = 2.5 \text{ M}$, $C_L = 1000 \text{ pf}$, Sink $10 \mu\text{a}$
 - (e) Desired telemetry A/D accuracy = 8 bits
 - (f) Maximum output fault voltage = +1 V, -8.5 V
- (2) High Rate Sampled Outputs - 1 Sample/10 sec.
 - (a) Peak Channel A
 - (b) Area Channel A
 - (c) Peak Channel B
 - (d) Area Channel B
 - (e) Peak Channel C
 - (f) Area Channel C
 - (g) Cal. on
 - (h) 2-minute O.S.
- (3) Low Rate Sampled Outputs

<u>Output</u>	<u>Desired Sample Rate</u>
(a) Background Channel A	1 Sample/Minute
(b) Background Channel B	
(c) Background Channel C	
(d) Sensor Temperature	
(e) Electronics Temperature	
(f) Gain Status	
- (4) Recorder Inputs
 - (a) Video Channel A
 - (b) Video Channel B
 - (c) Video Channel C

(4) Recorder Inputs - Continued

Desired Characteristics

- (a) Bandwidth = 50 cps
- (b) Amplitude Range +1 V to -8 V
- (c) Load R \geq 20K

4.2.2.5 Experiment Inputs

(1) Impulse Command for Gain Switching

- (a) Off level: Open relay (normal position)
On level: Relay shorted to ground
- (b) Duration of short: 60 milliseconds min.
Contact bounce duration: 4 milliseconds max.
- (c) Relay contact rating: 28 V at 0.5 ma

(2) Data Reset Pulses

- (a) Function: These pulses reset the experiment temporary storage circuits after they are "read" by the telemetry unit
- (b) Number required: 3 (one per channel). This input simultaneously resets the peak and the area outputs of a channel.
- (c) Reset Pulse Characteristics

Amplitude upper level: 5 V to 11 V

Amplitude lower level: 0 to +1.3 V

Pulse duration: 140 nsec. min.

Pulse position: The pulses falling edge activates the temporary storage reset pulse

Load 22K shunted by less than 100 pf capacity

(3) Input Power

- (a) Voltage range: Minimum = 23.5 V
Maximum = 34.0 V
10 milliseconds transient = +40 V
- (b) Source impedance = 1.5 Ω max.

(3) Input Power - Continued

- (c) Input ripple = 450 mV pp max.
- (d) Experiment output ripple \leq 40 mV peak-to-peak
- (e) Experiment power at +28 V

Quiescent = 7.5 watts @ -20°C

Peak during calibrate \approx 9.5 watts

For 3-sec. period occurring every 4 to 6 minutes

Standby power when experiment is in the sunlight
side of the orbit \approx 3.0 watts

4.2.2.6 Calibration Light Source

The signal photomultipliers will observe a 2-second calibration light source every 5 minutes. An output line is provided to monitor when calibration occurs.

4.2.2.7 Temperature Range

The acceptable temperature range is -20°C to $+45^{\circ}\text{C}$.

4.2.2.8 Sensor to electronics maximum cable length = 12 feet.

4.2.3 Signal Channel Description

The signal channel block diagram is shown on Figure III-6.

A dc amplifier is used to monitor the PMTS dc background current. The meteor flash signals are amplified by an ac coupled amplifier. Gain control signals are used to select an amplifier gain of 6, 20, or 60. This feature allows the system to change its sensitivity and increases its dynamic range.

When the signal PMTS are first turned on, the incident background light will create a large step voltage at the input. Since the input r-c time constant must be large, this step can block the amplifier for 10 minutes. The input switch reduces this recovery time to 2 minutes. The switch is actuated by the PMT turn-on signal and effectively reduces the input time constant for a 2-minute period.

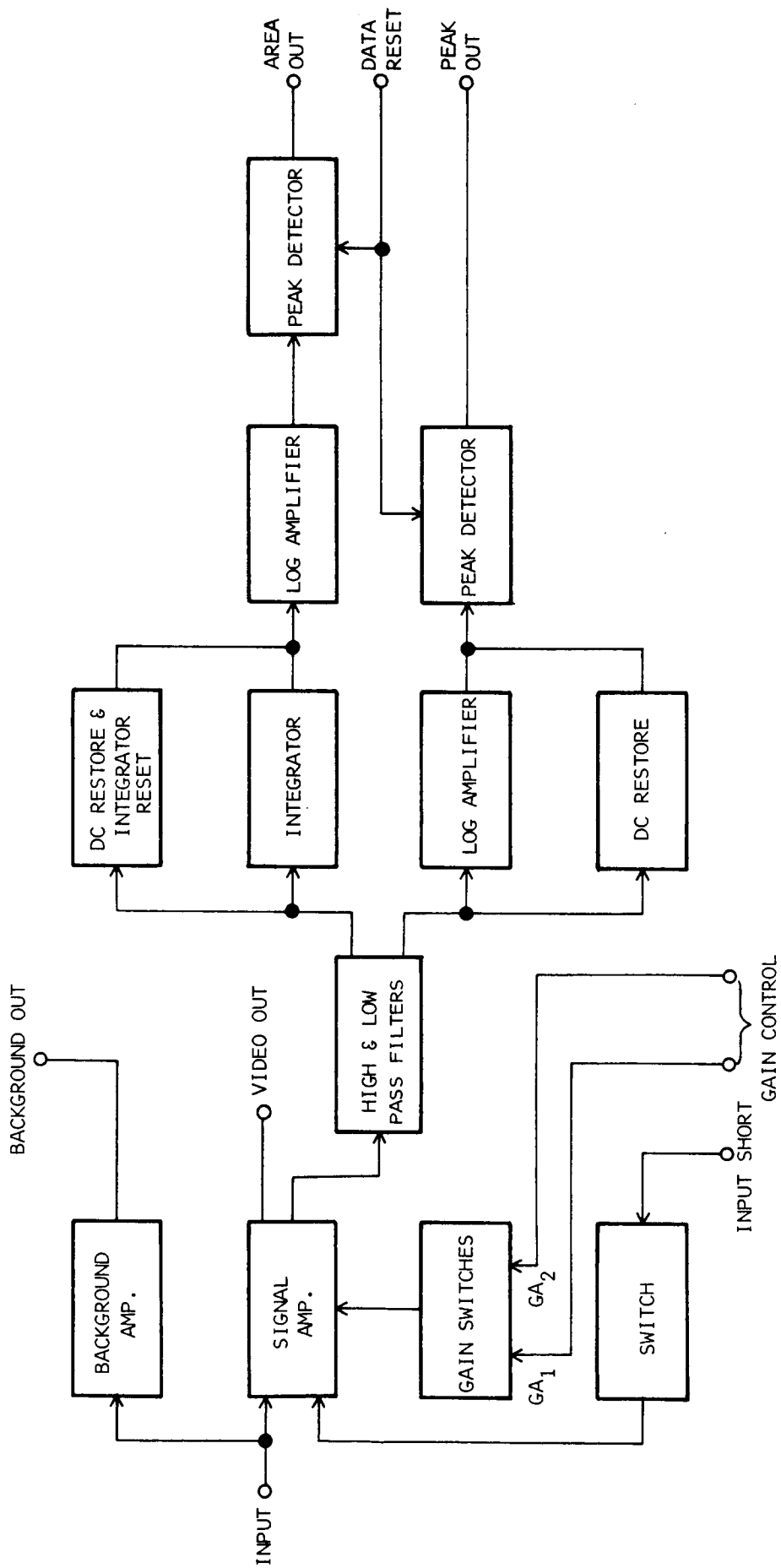


Figure 12. BLOCK DIAGRAM BASIC SIGNAL CHANNEL

After amplification, the signals are filtered by a low-pass (2.4 cps) and a high-pass filter (0.1 cps). These filters are used to increase the system signal-to-noise ratio. In addition, the high-pass filter blocks the input amplifier's dc drift.

Since a high-pass filter cannot pass a dc voltage, unipolarity pulses will cause a dc level shift at its output. The dc shift is a function of the signal repetition rate and can be quite severe for high rates. The dc shift problem is eliminated (at the expense of reduced signal-to-noise ratio) by dc restore circuits. The restoration is accomplished by clamp diodes which are the feedback elements of operational amplifiers. This arrangement reduces the clamped off-set error to less than 0.2 mV. The dc restore circuit at the integrator input provides another important function. The input is clamped at the end of a signal. This clamping action also resets the integrator. Thus, the integrator is automatically reset after each signal pulse. A threshold adjust is provided to insure that the integrator is reset and will not drift when there is no signal and the noise level is too low to guarantee the clamp reset action.

Log amplifiers are provided to compress the signal dynamic range (at the expense of the signal-to-noise ratio). This is required to minimize the effect of telemetry error. For example, for a linear system the output signal will range from 5 mV to 5 V. For an 8-bit telemetry system, the maximum resolution is 20 mV. Thus, for low level signals the error can be

$$\frac{20 \text{ mV} \times 100}{5 \text{ mV}} = 400\%$$

The log amplifiers are followed by peak detectors. The signal's peak amplitude and area are stored on the peak detector capacitors. The circuits hold this analog voltage until the telemetry system multiplex is ready to accept the data outputs. After the telemetry read pulse, a data reset pulse is generated to reset the peak detectors.

Typical signal wave forms are shown on Figure 13.

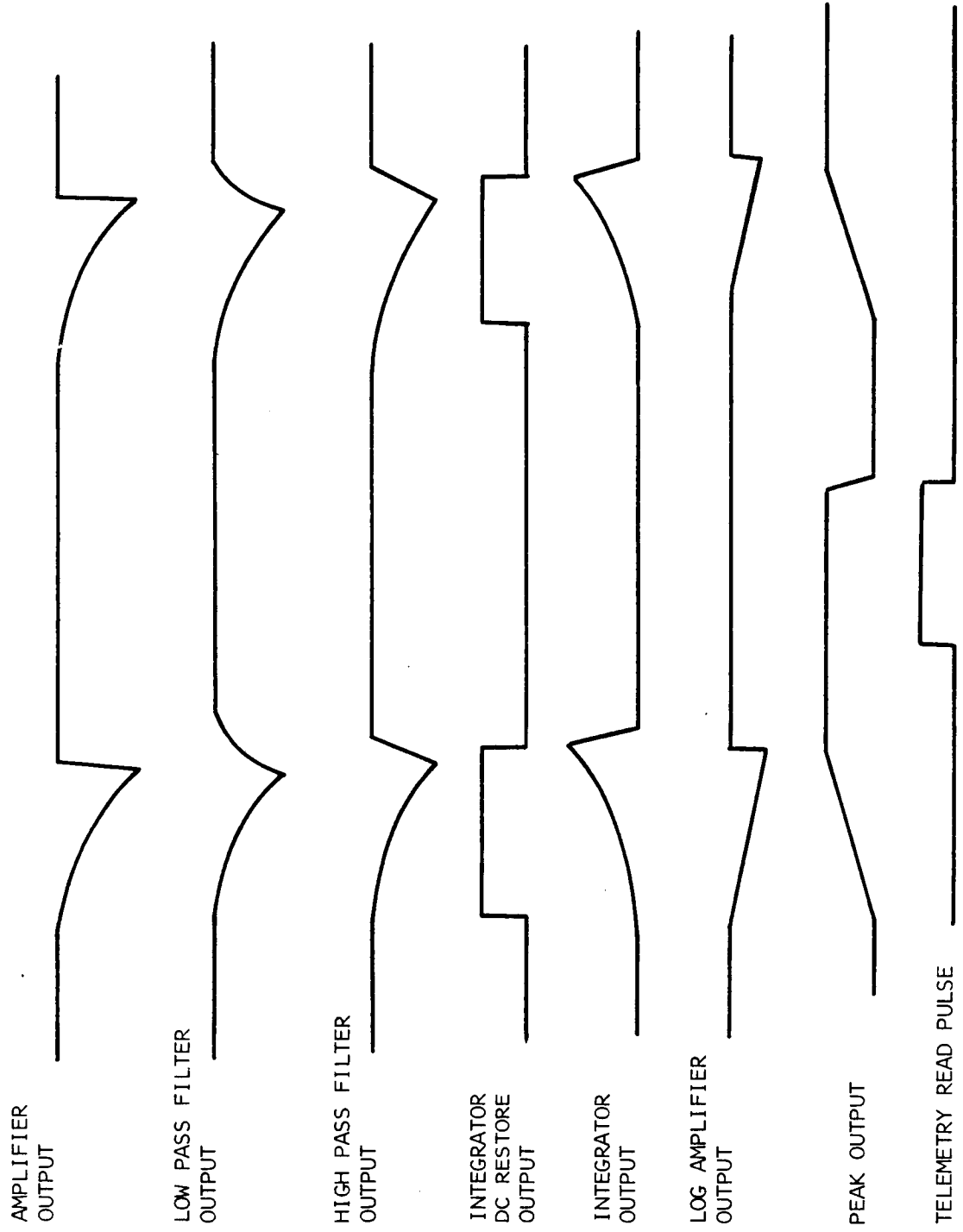
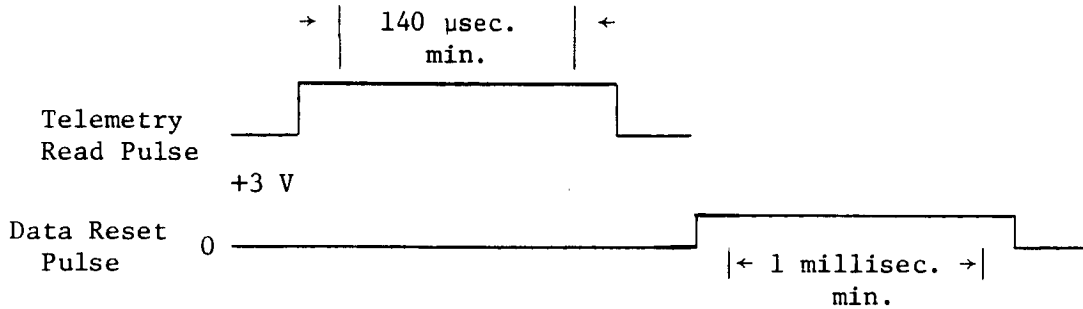


Figure 13. SIGNAL CHANNEL WAVE FORMS

4.2.4 Telemetry Interface Block Diagram

The block diagram is shown on Figure 14. Two one-shots are provided to reset the signal channel peak detectors. It has been assumed that the telemetry system will send a pulse when it is accepting data from an analog word output line. The trailing edge of this pulse will trigger the one-shot as shown below.



The signal channel gain can be changed in increments of ± 10 db by an external gain advance signal. A total of 27 gain combinations for the three channels is provided by the incremented 27-state counter. A D/A converter allows determination of the counter state (hence system gain) via one experiment analog word line.

4.2.5 Power Conversion, Protection Circuits and Calibration Generation

The block diagram is shown on Figure 15. A dc-to-dc converter converts the input 28 V dc to a 10 kc square wave. The basic preregulated +9, -9, +34 V is obtained by transformer coupling, rectifying, and filtering the square wave. These unregulated supply voltages supply power to the photodiode detection circuitry. Regulated +12 V, -12 V, and -5 V is obtained from three current limited regulators. Two dc-to-dc converters supply +2.0 kV for the PMTS and 700 V for the calibration lamp.

The protection circuitry controls the system power and operates as follows: As the satellite approaches the sunlight side of its orbit, the sunlight triggers the photodiode detection circuitry. This action turns off the +12 V and -12 V power supplies and hence, power to the photomultipliers. The -5 V supply is not turned off to maintain the state of the gain control flip-flops.

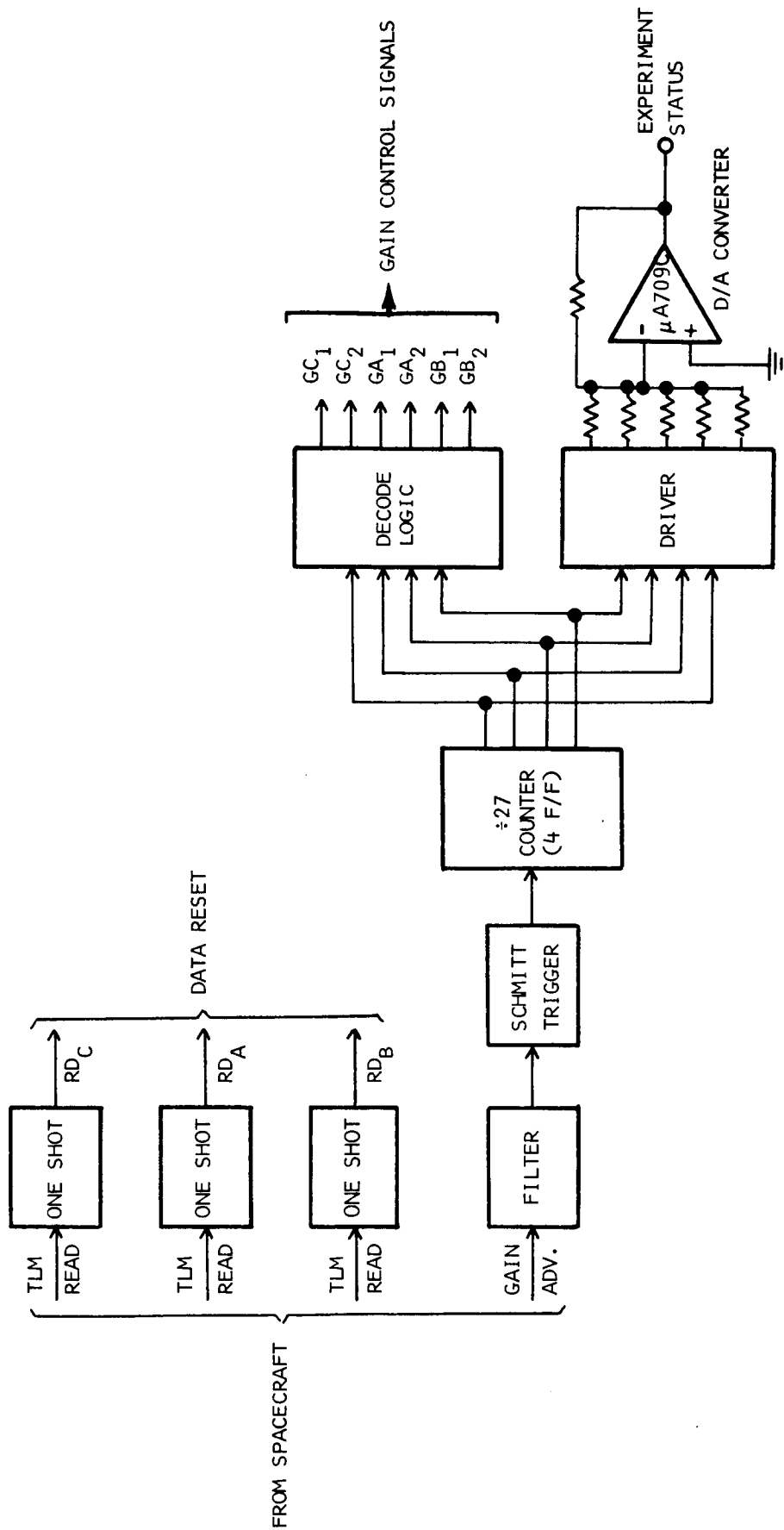


Figure 14. BLOCK DIAGRAM TELEMETRY INTERFACE CIRCUITS

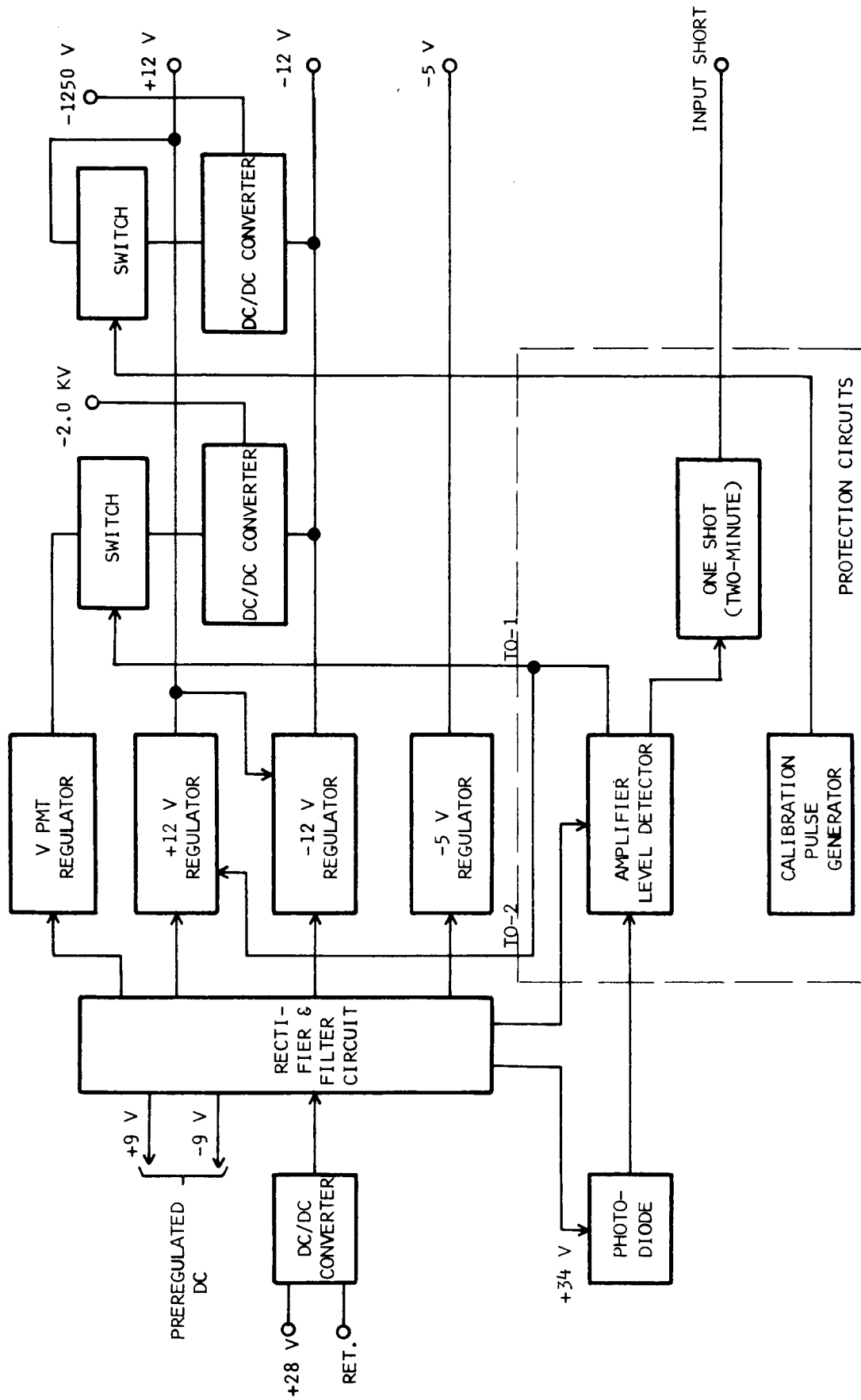
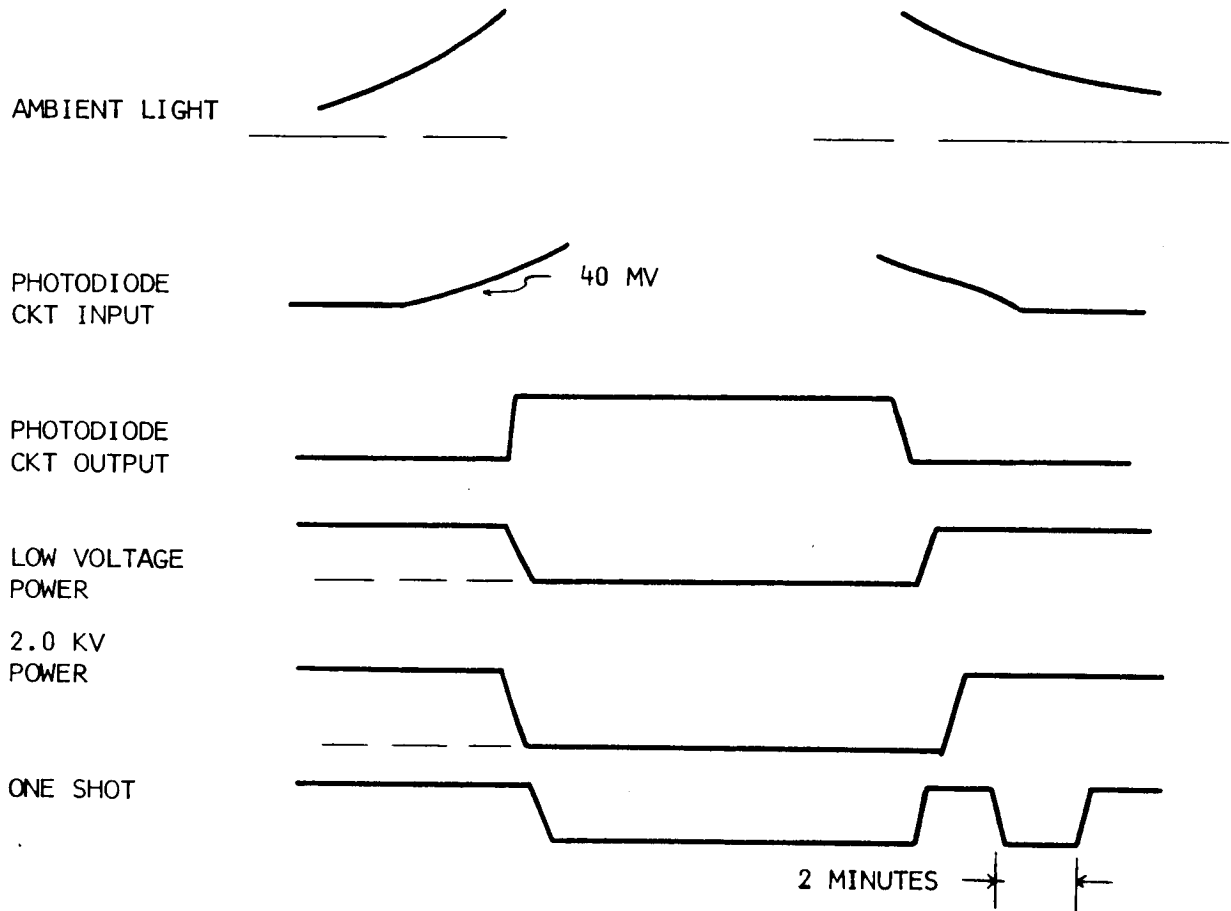


Figure 15. BLOCK DIAGRAM POWER CONVERSION AND PROTECTION CIRCUITS

As the satellite approaches the dark side of its orbit, the photodiode will turn on the 2.0 kV power to the signal PMTS. This will introduce a large transient at the PMT output. The 2.0 kV turn-on triggers a 2-minute one-shot which controls circuitry that recovers the signal channels from the transient.

The basic signal wave forms are shown below.



The calibration generator generates a 2-second light flash every 5 minutes. This light flash is used to calibrate the signal channel outputs. Since the calibration time is asynchronous with the telemetry, an experiment output line must be provided to monitor when calibration occurs. This output is also used to monitor the calibration lamp current level.

5. CALIBRATION FACILITY AND PROCEDURE

5.1 CALIBRATION TEST FACILITY

The calibration test facility in general is assembled from standard laboratory equipment, supplemented by some special items designed and fabricated specifically for the MFA. The latter are the electronic meteor flash simulator and the optical meteor flash simulator. Several (7) general purpose laboratory power supplies capable of supplying up to 28 V dc and .200-.300 A are required.

5.1.1 Relative Spectral Response

The basic component for this test is a McPherson Model 218 monochromator with a 2400 λ /mm grating. Of primary importance in this measurement is a Reeder thermocouple, with power responsivity wavelength independent, and a Deuterium discharge lamp with spectral output corresponding to the wavelength range of interest. This lamp eliminates scattered light problems which could cause significant errors in the far and middle ultraviolet channels.

5.1.2 Relative Field-of-View Response

The field-of-view fixture is a large, rigid framework with an adjustable table upon which to mount the instrument. The entire fixture is mounted on a rotary table, with angular resolution of $1/4^\circ$, for rotation about the vertical axis. The mounting table is held in a yoke assembly which is rotated around the horizontal axis by an identical rotary table. A small laser is useful for alinement of optical axes.

5.1.3 Absolute Spectral Response

An Eppley Laboratory thermopile is used to calibrate secondary standards which are particularly applicable to the MFA calibration. The thermopile is calibrated by Eppley against standards traceable to N.B.S. in volts/watt/cm² incident on the detector. Hg lamps with line emissions at 2537 Å and 3650 Å are ideal sources for calibrating the MFA. Because of thermal drift problems

associated with measurement of small DC signals from the thermopile, a thermocouple and lock-in amplifier are used as an intermediate comparison measurement system.

5.1.4 Optical Background Simulation and Sun Sensor Function

The flash tests are most conveniently carried out with the simulator and MFA in close proximity, covered by a black cloth to provide total darkness. The background simulation is easily controlled by a small W lamp placed under the cloth and operated by a variable power supply. The sun sensor test can be performed easily by several means. The method chosen is illumination of the MFA by a commercial Sun-Gun lamp operated by a variac to provide intensity control if desired.

5.1.5 Additional Facilities

An assortment of electronic, optical and mechanical equipment is also required to perform the tests. These are standard items and are called out as required for each test.

5.1.6 Special Test Equipment

5.1.6.1 Electronic Meteor Flash Simulator

The simulator test set is a signal conditioner and junction box. All signals and voltages entering and leaving the MFA electronic and sensor assemblies are routed through this unit. For monitoring input and output signal levels, multiple position switches and test jacks are provided on the control panel. The test set provides a variable amplitude, exponentially rising voltage as a signal source (electronic simulation) when the sensors are not being used. When the sensors are used, the test set drives the light source to produce an optical signal of the same temporal variation (optical simulation).

5.1.6.2 Optical Meteor Flash Simulation

The basic circuit block diagram of the optical flash simulator is shown in Figure 16. An incandescent lamp is used to convert a current into a light output. A portion of the light output is converted to a feedback current by a photomultiplier. A summing amplifier compares the feedback with the input waveform. The difference is amplified and controls the lamp current. Thus the lamp output is controlled by a closed loop servo and follows the input waveform.

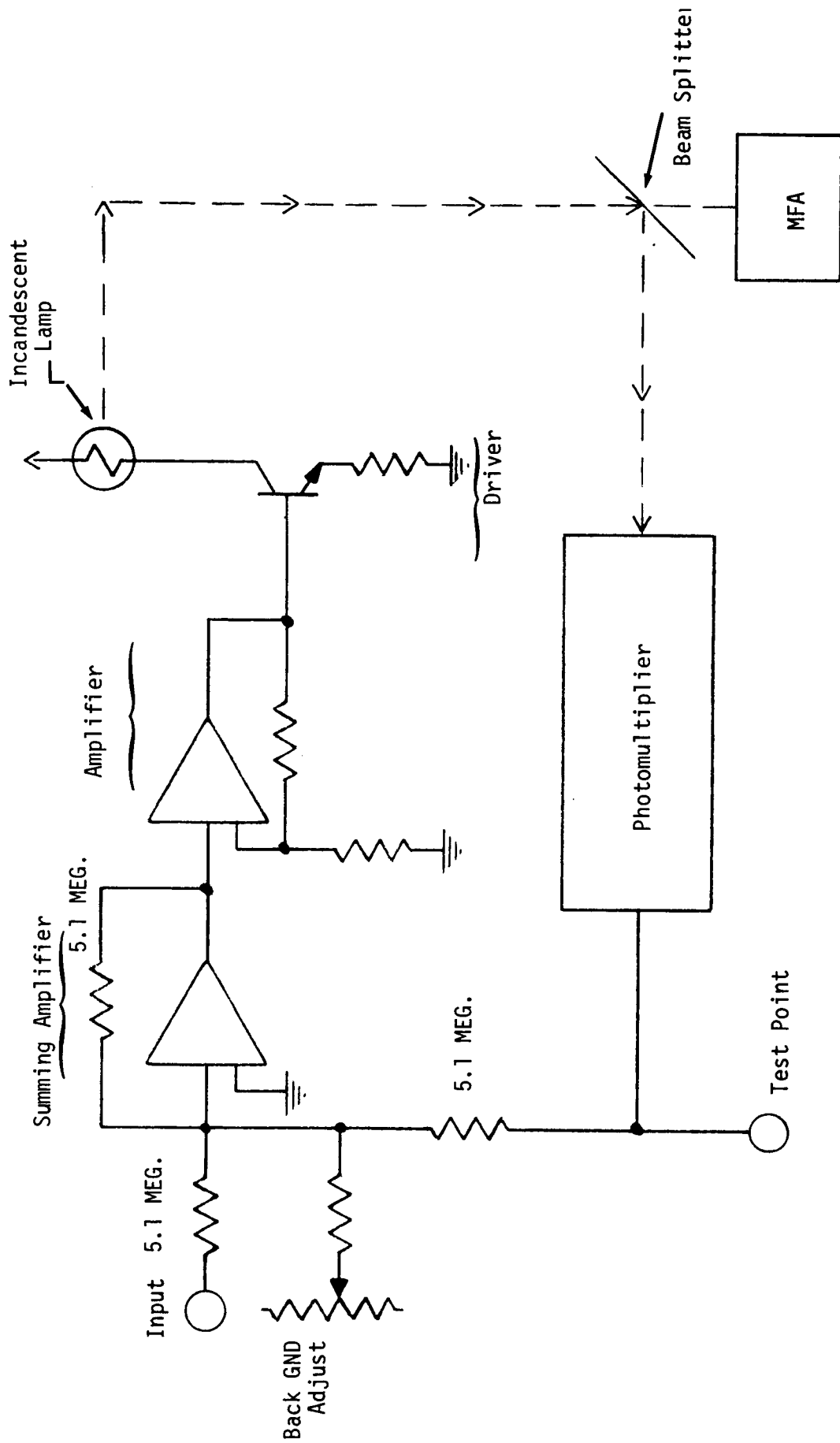


Figure 16. Circuit Block Diagram of Optical Flash Simulator

5.2 CALIBRATION TEST PROCEDURE

5.2.1 Electronic Tests

Equipment Required

MFA Electronic Flash Simulator
H.P. 202A Function Generator (or equivalent)
H.P. 350 D Attenuator
Digital Voltmeter, H.P. 3440 with 3443 Plug-in (or equivalent)
Oscilloscope
Temperature Controlled Chamber
1/15 Voltage Attenuator
Chart Recorder

Procedure

Set up the experiment as shown in Figure 17.

5.2.1.1 Temperature Monitor Test

Set the output selector to Exp.Temp.; record the DVM reading and ambient temperature. Place the electronic assembly inside the temperature chamber. Allow the system to come to equilibrium at -10°C . Record the temperature monitor output. Repeat at $+50^{\circ}\text{C}$.

5.2.1.2 Signal Channel Response Test

Set the output selector to Exp. Status and push the gain advance button until the DVM reads $4.2\text{V} \pm 0.2\text{V}$. This voltage corresponds to gain 21 for each channel. Set the experiment Data Reset to manual and control reset by the push button. Insert the 1/15 attenuator in series with the H.P. 350D. Set the Pulse Position toggle switches to Generator B and connect the oscilloscope to the Test Monitor.

Observe the exponential waveform on the oscilloscope screen. Adjust the amplitude potentiometer until the peak output is five volts. Set α at five. For attenuations of 0, 10, 20, 30, 40, 50 and 60 db, record the peaks and areas for the three data channels. Reset the data outputs before each reading. Repeat for $\alpha = 3.2$ and $\alpha = 1.4$. At $\alpha = 3.2$ and 20 db attenuation, short (turn off) the simulator output. Measure the fall in output voltage for peak and area outputs.

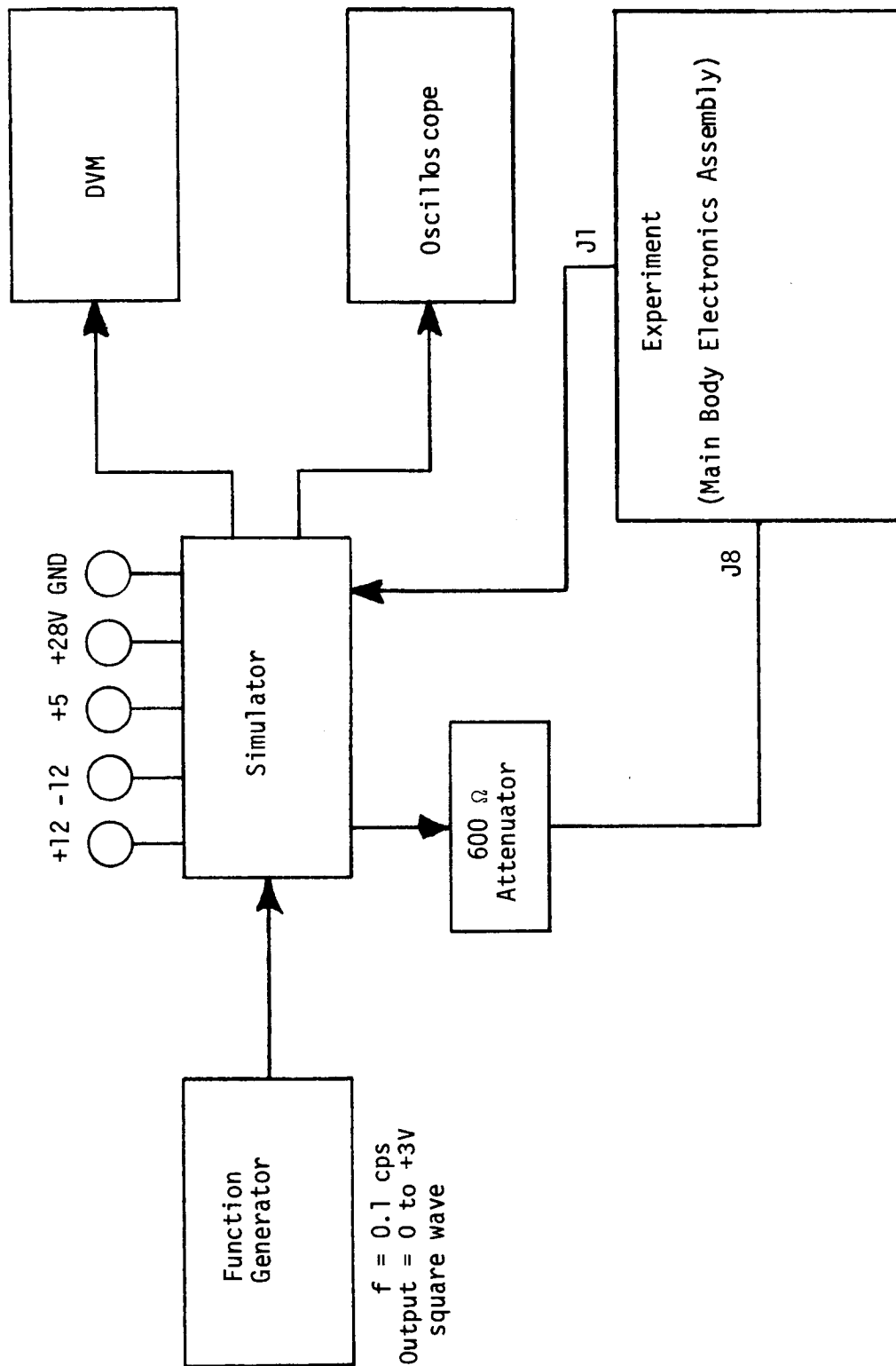


Figure 17. Electronic Test Block Diagram

Perform these measurements at ambient temperature, -10°C and $+50^{\circ}\text{C}$. Delete the memory hold voltage experiment at 50°C .

5.2.1.3 Experiment Status Voltage Steps

The purpose of this test is to demonstrate that the gain status diagnostic voltage corresponds to the correct combination of the 3 gain states for each channel. With the experiment setup as for the previous test, set the attenuator at 20 db. Set the output selector to Experiment Status. Record the experiment status voltage, and the peak output amplitude of each video output on the oscilloscope. Advance the gain state and repeat the measurement until all 27 steps have been observed.

5.2.1.4 Photodiode Circuit Tests

Turn on the photodiode tester voltage. Record the experiment status voltage. Increase the photodiode voltage until the +12V and -12V are turned off, as indicated by the experiment status voltage output going negative. Record the photodiode voltage at turn-off. Decrease it slightly and verify that the experiment status voltage returns to its original value. Repeat this test in the temperature chamber at -10°C and $+50^{\circ}\text{C}$. At ambient temperature, record the input current at 28V before and after the photodiode turns off +12V and -12V.

5.2.1.5 Calibration Lamp Circuit Tests

Connect the Cal Monitor output to the recorder. Record several pulses and observe the pulse duration, pulse amplitude and pulse repetition rate.

5.2.2 Relative Spectral Response

Equipment Required

Deuterium Light Source
Condensing Lens
Light Beam Chopper
Monochromator
Thermocouple Detector
Lock-in Amplifier
Collimating Lens
Strip Chart Recorder
MFA Sensor Unit Test Chassis

Procedure

Set up the equipment as shown schematically in Figure 18. The thermocouple can be removed from the beam by rotating a mirror, allowing the beam to continue on through the collimator and irradiate the MFA, as shown in the diagram. Allow the deuterium lamp to warm up for 10-15 minutes. With the thermocouple in place, and the beam chopper in operation, record the system output from 2000-4000 Å. Record amplifier gain settings.

Rotate the mirror behind the exit slit which focuses the beam on the thermocouple until the beam is directed to the collimator. Turn off the chopper and make sure that the beam is not obstructed. Place the MFA sensor unit so that the collimated beam strikes the aperture at Channel A. Apply the power required to operate the MFA through the test chassis. Connect the output monitor at Channel A to the chart recorder. Record the output from 2000-3000 Å. Keep track of the "volts-full-scale" settings of the chart recorder. Make sure that the peak signal level is below 4 volts.

Move the MFA until Channel B is irradiated by the collimated beam. Switch the output monitor on the test chassis to B. Record the output from 2300-3500 Å. Keep track of the "volts-full-scale" settings of the chart recorder. Make sure that the peak signal level is below 4 volts.

Repeat as above for Channel C. Record the spectral output from 2500-4000 Å.

This completes the data recording required to plot the relative spectral response.

5.2.3 Field of View

Equipment Required

Field of View Test Fixture
Deuterium Light Source
Tungsten-Iodine Sun Gun
Neutral Density Filters
MFA Optical Unit Test Chassis
Digital Voltmeter
Laser

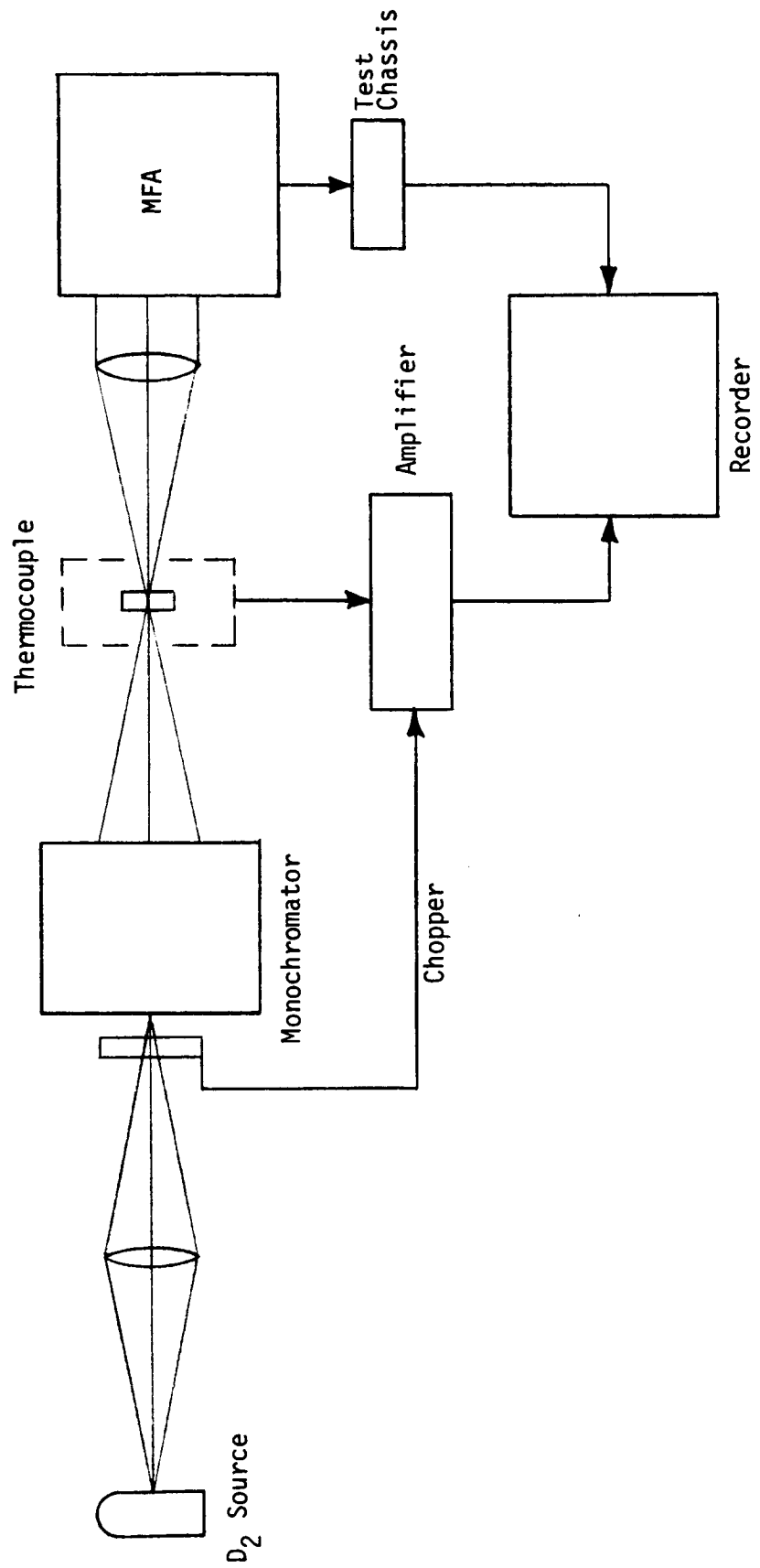


Figure 18. Relative Spectral Response Test Block Diagram

Procedure

Attach the MFA sensor unit to the field-of-view fixture, with the azimuth and elevation adjustments set at 0° . Aline an optical bench rail perpendicular to the MFA, Channel A, on the fixture. Set the Deuterium lamp on the optical rail one meter or more from the MFA aperture. Place several neutral density filters (total ND = 4 or greater) in front of the lamp. Turn on the lamp and block the indirect illumination with black cloths or flocking paper. Connect the output monitor of the test chassis to the digital voltmeter, and select Channel A.

Turn off the room lights. Apply power to the MFA. Remove neutral density filters until the output is .500-1.00 volts. With the azimuth at 0, change the elevation in the + direction, and record the output at intervals of 2° - 3° until the signal has fallen to 10% or less of the maximum observed signal. Return to the 0° - 0° position and repeat for - elevation. Return to 0° - 0° and move the azimuth setting to $+5^\circ$. Record the output, then repeat as above for + and - elevation. Continue this procedure at azimuth increments of 5° until azimuth setting is $+15^\circ$. Beyond this point, observe the change of output at 0° elevation, and increase the azimuth setting in increments sufficient to distinguish 1/2 and 1/10 maximum response. Repeat the procedure for - azimuth angles until reaching $\sim 1/10$ maximum response position.

Return the field of view fixture to the 0° - 0° position. Remove the D_2 lamp and aline MFA Channel B along the axis established by the laser. Replace the lamp and repeat the procedure as for Channel A. After completing Channel B data recording, aline Channel C of the MFA and repeat the same procedure. (Note: it may be more convenient to use a variac controlled "sun-gun" type W lamp to achieve the desired stimulation of Channel C). Record all the data required for Channel C. Reset and aline the MFA photodiode channel, and repeat the procedure for the photodiode. (Note: the photodiode response should be more uniform and fewer data points will be required.)

5.2.4 Absolute Responsivity

Equipment Required

Calibrated Hg Pen Ray Lamp
Calibrated Hg Osram Lamp
Neutral Density Filters
2537 Å Interference Filter
3650 Å Corning Filter
MFA Electronic Test Console
Digital Voltmeter

Procedure

Mount the pen ray lamp on an optical rail behind the 2537 Å interference filter and a number 2 neutral density filter. Block the reflected, indirect beams by shielding the lamp with black cloth or flocking paper. Place the MFA approximately 10 ft. from the lamp. Cover the filters with an opaque shutter, turn on the lamp and allow it to warm up for 30 minutes to assure stability.

After the lamp has warmed up, turn off all room lights. Apply power to the MFA through the test console. Connect the output monitor to the digital voltmeter. Record the D.C. background output of Channels A and B. (These outputs should read ~ 16 mv.) Cover the MFA aperture with black cloth or paper so that the instrument can see no external light. Observe backgrounds A and B and record the values if there is a change. (Channels A and B are UV sensitive only and should not be stimulated even if the darkened room has light leaks).

Remove the shutter from the lamp-filter combination and record the outputs of A and B. Make sure that the signals are in the linear range of the instrument (4 V or less). Turn off the lamp and the instrument; turn on the room lights. Measure the distance from the MFA aperture to the lamp.

Replace the lamp/filter combination with the Osram lamp, 3650 Å filter, and a number 3 neutral density filter. Turn the lamp on for 30 minutes before making a measurement. Block the scattered light and shutter the direct beam as before. Place the MFA ~ 50 ft. from the lamp. Turn off the lights and turn

on the MFA. Record the background output of the Channel C. Blind the MFA and record the zero irradiance background C output. (In this case, the light level in the room will probably cause a signal, 5-10 mv above the zero level.) Uncover the MFA, remove the shutter from the lamp and record the Channel C output. Make sure that the signal is less than 4 V. Turn off the lamp and instrument; turn on the room lights. Measure the distance from the MFA aperture to the lamp.

5.2.5 Meteor Flash Simulation

Equipment Required

Optical Flash Simulator
MFA Electronic Flash Simulator
H.P. 202A Function Generator (or equivalent)
H.P. 350D Attenuator
Digital Voltmeter
Oscilloscope and Camera
Optical Flash Control Chassis
Small W Lamp
Neutral Density Filters

Procedure

Set up the equipment as shown schematically in Figure 19. The flash simulator should be approximately 6-12 inches from the MFA aperture, Channel C. A black cloth large enough to cover both the flash simulator and MFA optics provides the convenience of not having to work in a totally dark room. The neutral density filters and simulator-MFA distance can be adjusted by reaching inside the cloth.

Set the function generator for a .1 cps square wave. Set the 8 pulse position switches at generator B, α selector switch at 3.2, and connect the monitor to the oscilloscope. With a .5 cm/sec. sweep, observe the output on the oscilloscope screen and rotate the amplitude adjustment until the peak of the exponential waveform is 5 volts. Disconnect the electronic signal from

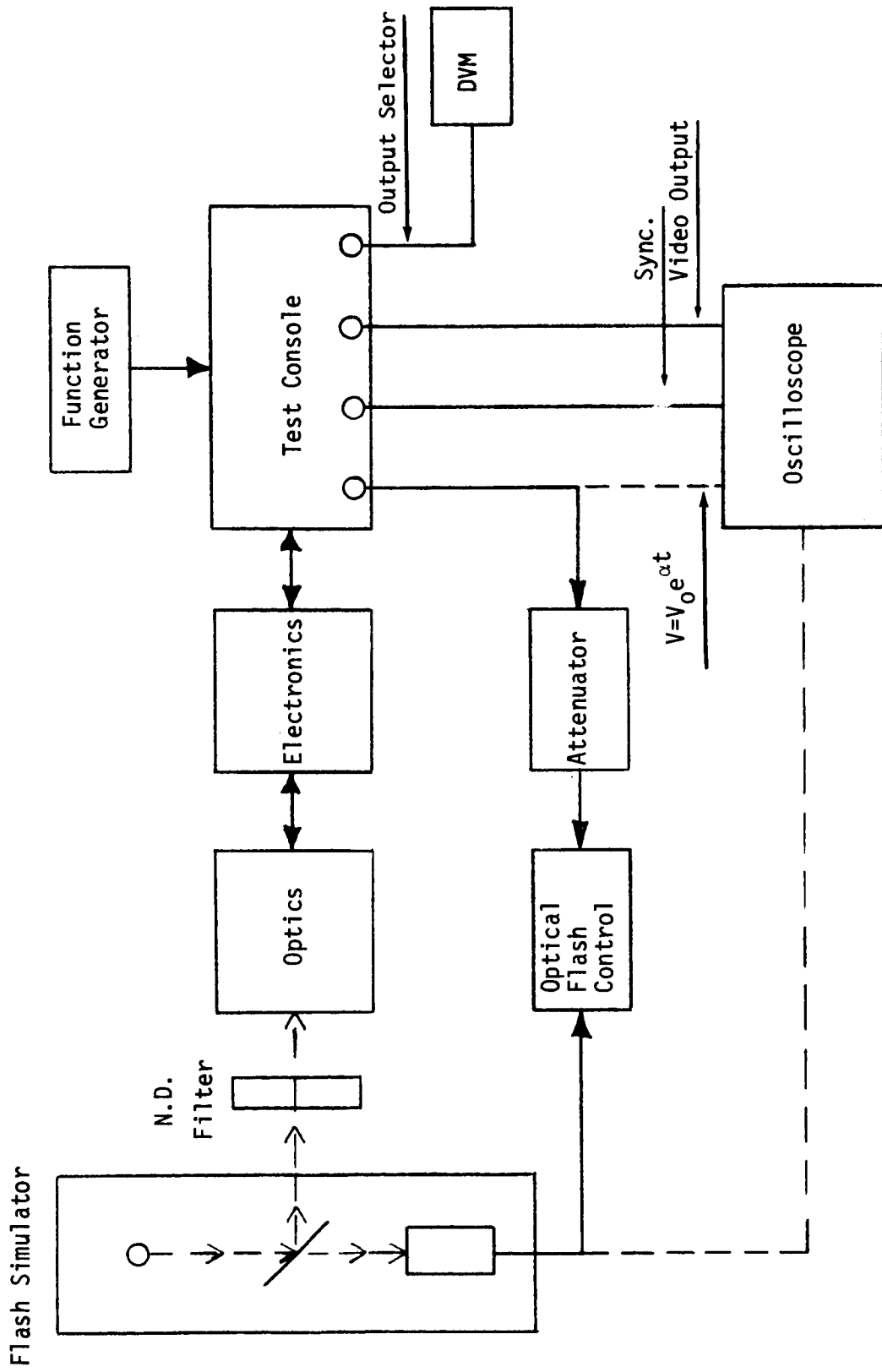


Figure 19. Optical Flash Simulation Test Block Diagram

the oscilloscope and connect it, through the attenuator, to the flash control input. Connect the control photomultiplier output from the flash control chassis to the oscilloscope. Observe the output and verify that the waveform is identical to the electronic driving function. With an EMI 6255 tube at 600 V, the peak output should be approximately .4 V. (Note: in the adjustment stages it may be convenient to increase the function generator frequency.) Remove the photomultiplier output from the oscilloscope.

Connect the video output monitor to the oscilloscope and set the selector switch to Channel C. Connect the output selector to the digital voltmeter and set the switch at background C. Set the reset switch on the test console to manual and control experiment reset by the two push buttons. Turn on the MFA. With no neutral density filter in the path, adjust the simulator-aperture distance until the video output waveform is approximately 6 V at its peak, and the background monitor reads -5 to -10 mv. (The attenuator may be useful in obtaining the desired output.) At 6 V peak output, the system is operating nearly at its upper limit. Switch the output selector to the gain position, and record the voltage; return the switch to peak C. Cover the MFA aperture and reset the experiment. The DVM should read 500 mv or less. Switch to area C; the output should also be 500 mv or less. If the experiment does not reset, wait 1-2 minutes, pressing the reset button intermittently, until the peak and area diagnostics have reached the correct levels. The system is now adjusted for simulated flash testing.

Uncover the MFA aperture. Photograph the oscilloscope trace when the lamp triggers. Record the peak and area voltages. Reset the experiment and record the reset levels of the peak and area detectors. Record the background voltage. Record the peak, area and reset voltages for two more flashes, but do not take additional photographs.

Insert a neutral density 1 filter in the path. Repeat the measurements as above. Remove the N.D. 1 filter and replace it with N.D. 2. Repeat the same set of measurements. Remove the N.D. 2 filter and insert N.D. 3. Repeat the measurements, but do not take any photographs.

Remove the neutral density filter. Place the small W lamp under the black cloth, between the filter position and the aperture. Using a variable power supply, turn the lamp on slowly until the background output reads $\sim +10$ mv. Perform the same set of measurements as above, except for those with neutral density 3 filter. Increase the lamp power until the background voltage is $\sim +100$ mv. Repeat the measurements as with background of 10 mv. This completes the flash testing on Channel C. Turn off the MFA.

The flash simulator lamp is a glass covered W lamp, and thus the short wavelength radiation is insufficient to stimulate Channels A and B. For the purpose of verifying operation of the electronic system with an optical input, remove the instrument covers and remove the interference filters and holders from photomultiplier tubes A and B. (Once performance has been verified, it is recommended that this test is not repeated.) Replace the covers and setup the experiment as before, with the flash simulator positioned before Channel A. Adjust the distance and/or attenuation for peak signal of 6 V and background of approximately 17 mv. Perform the measurements as before with no filter, followed by N.D. 1-3. Repeat the measurements on Channel B. Turn off the MFA. Replace the interference filters on the detectors. This completes flash testing of the unit. Leave the experiment setup for the next test.

5.2.6 Sun Sensor Test

Procedure

Set the experiment as in the previous test for Channel C, no external background. Insert neutral density 3 filter and record peak, area, and reset levels for three flashes. Remove the black cloth covering the experiment. Illuminate the MFA with a variac controlled sun gun. Increase the power until the photodiode turns off the photomultiplier high voltage supply. Background C output should be 5.3 - 5.5 V just before turn-off. In the off condition, the background monitor reads a negative voltage. (If the background reaches 5.7 V without turning off, stop the experiment. It may be necessary to reset the photodiode control circuit.) Decrease the sun gun intensity until the high voltage is just turned back on. Record the background outputs of A, B and C. Turn off the sun gun and replace the black cloth.

Reset the experiment. Record the time required for the instrument to recover (Channel C). Record the peak, area and reset levels of several flashes. Repeat two more times. Remove the filter and record peak, area and reset levels of three flashes.

5.2.7 Noise Level

Equipment Required

Tektronix Oscilloscope with Type E Preamplifier

Procedure

Cover the MFA with black cloths. Apply power to the instrument and record the background outputs. Connect the video output monitor to the oscilloscope. Set the bandpass of the preamplifier for .06 - 50 cps. Display A, B, and C video outputs on the oscilloscope and record the peak to peak voltage with the gain setting at 4.16 V.

This completes the calibration and testing of the Meteor Flash Analyzer.

6. CALIBRATION TEST RESULTS

6.1 ELECTRONIC TEST RESULTS

6.1.1 Temperature Monitor

<u>Temperature</u>	<u>Monitor Voltage</u>
-10° C	3.73
27° C	1.28
50° C	0.693

These three voltages determine the temperature-voltage line for the thermistor monitor.

6.1.2 Signal Channel Response

The data are shown in Tables 8a, 8b, and 8c, and graphically in Figures 20-31. When the sensor unit is connected, this data is required to determine voltage outputs of the detector load resistors. Coupled with the optical calibration, this information determines the absolute value of irradiance at the instrument aperture.

The memory hold test verifies that the voltage outputs fall less than .020V in a 10 second period.

6.1.3 Experiment Status Voltage

The data of Table 9 demonstrate that the logic which determines the state of each gain switched amplifier for a given experiment status functions properly. The accompanying Table 10 shows the desired status in terms of high, medium, and low gain, as well as the actual gain. The values 1.75, .70 and .20 were observed on an oscilloscope and merely correspond to H, M and L, and do not constitute an accurate measurement of the ratio, 53:21:6.

Table 8a. Signal Channel Response Data

α	Attenuation db	Peak Volts E_p	Intergal, $f = E_p/\alpha$	Peak A	Area A	Peak B	Area B	Peak C	Area C
5	60	3.33×10^{-4}	6.66×10^{-5}	.574	.683	.659	.642	.679	.567
5	50	1.06×10^{-3}	2.12×10^{-4}	1.26	1.29	1.39	1.26	1.38	1.17
5	40	3.33×10^{-3}	6.66×10^{-4}	2.00	1.93	2.14	1.90	2.12	1.82
5	30	1.06×10^{-2}	2.12×10^{-3}	2.74	2.56	2.85	2.55	2.83	2.48
5	20	3.33×10^{-2}	6.66×10^{-3}	3.48	3.22	3.57	3.21	3.56	3.17
5	10	1.06×10^{-1}	2.12×10^{-2}	4.23	3.89	4.29	3.89	4.29	3.86
5	0	3.33×10^{-1}	6.66×10^{-2}	4.98	4.56	5.00	4.57	5.02	4.56
3.2	60	3.33×10^{-4}	1.04×10^{-4}	.558	.791	.655	.756	.665	.661
3.2	50	1.06×10^{-3}	3.31×10^{-4}	1.24	1.45	1.38	1.43	1.36	1.33
3.2	40	3.33×10^{-3}	1.04×10^{-3}	1.99	2.11	2.12	2.08	2.10	2.00
3.2	30	1.06×10^{-2}	3.31×10^{-3}	2.72	2.75	2.83	2.73	2.82	2.67
3.2	20	3.33×10^{-2}	1.04×10^{-2}	3.47	3.41	3.56	3.40	3.54	3.36
3.2	10	1.06×10^{-1}	3.31×10^{-2}	4.21	4.08	4.27	4.07	4.26	4.05
3.2	0	3.33×10^{-1}	1.04×10^{-1}	4.96	4.76	4.99	4.76	5.00	4.76
1.4	60	3.33×10^{-4}	2.38×10^{-4}	.491	.930	.576	.860	.578	.781
1.4	50	1.06×10^{-3}	7.57×10^{-4}	1.15	1.70	1.28	1.67	1.27	1.58
1.4	40	3.33×10^{-3}	2.38×10^{-3}	1.89	2.39	2.02	2.37	2.00	2.29
1.4	30	1.06×10^{-2}	7.57×10^{-3}	2.62	3.05	2.74	3.04	2.72	2.98
1.4	20	3.33×10^{-2}	2.38×10^{-2}	3.37	3.72	3.46	3.71	3.44	3.67
1.4	10	1.06×10^{-1}	7.57×10^{-2}	4.11	4.39	4.18	4.39	4.17	4.37
1.4	0	3.33×10^{-1}	2.38×10^{-1}	4.87	4.93	4.90	4.92	4.90	4.90
Memory Hold Voltage				3.377	3.731	3.469	3.750	3.451	3.679
for 10 sec. period				3.369	3.723	3.458	3.741	3.446	3.669

Temperature 27°C

Table 8b. Signal Channel Response Data

α	Attenuation db	Peak Volts E_p	Integral $f = E_p / \alpha$	Peak A	Area A	Peak B	Area B	Peak C	Area C
5	60	3.33×10^{-4}	6.66×10^{-5}	.53	.701	.633	.651	.675	.676
5	50	1.06×10^{-3}	2.12×10^{-4}	1.24	1.33	1.38	1.37	1.39	1.25
5	40	3.33×10^{-3}	6.66×10^{-4}	1.98	1.97	2.12	2.04	2.12	1.87
5	30	1.06×10^{-2}	2.12×10^{-3}	2.72	2.61	2.84	2.68	2.83	2.52
5	20	3.33×10^{-2}	6.66×10^{-3}	3.44	3.22	3.52	3.32	3.53	3.17
5	10	1.06×10^{-1}	2.12×10^{-2}	4.20	3.93	4.27	4.02	4.28	3.89
5	0	3.33×10^{-1}	6.66×10^{-2}	4.95	4.60	4.99	4.70	5.01	4.59
3.2	60	3.33×10^{-4}	1.04×10^{-4}	.535	.805	.623	.746	.671	.739
3.2	50	1.06×10^{-3}	3.31×10^{-4}	1.23	1.49	1.36	1.52	1.37	1.40
3.2	40	3.33×10^{-3}	1.04×10^{-3}	1.97	2.15	2.10	2.20	2.10	2.05
3.2	30	1.06×10^{-2}	3.31×10^{-3}	2.705	2.80	2.82	2.86	2.82	2.72
3.2	20	3.33×10^{-2}	1.04×10^{-2}	3.42	3.46	3.54	3.53	3.54	3.39
3.2	10	1.06×10^{-1}	3.31×10^{-2}	4.19	4.13	4.25	4.20	4.26	4.09
3.2	0	3.33×10^{-1}	1.04×10^{-1}	4.94	4.80	4.97	4.88	4.98	4.78
1.4	60	3.33×10^{-4}	2.38×10^{-4}	.450	.938	.520	.783	.577	.652
1.4	50	1.06×10^{-3}	7.57×10^{-4}	1.13	1.74	1.27	1.75	1.27	1.60
1.4	40	3.33×10^{-3}	2.38×10^{-3}	1.87	2.43	2.01	2.48	2.00	2.33
1.4	30	1.06×10^{-2}	7.57×10^{-3}	2.60	3.09	2.72	3.15	2.71	3.01
1.4	20	3.33×10^{-2}	2.38×10^{-2}	3.34	3.76	3.44	3.82	3.43	3.70
1.4	10	1.06×10^{-1}	7.57×10^{-2}	4.09	4.42	4.15	4.50	4.16	4.39
1.4	0	3.33×10^{-1}	2.38×10^{-1}	4.84	4.96	4.87	5.02	4.88	4.92
Memory Hold Voltage				3.350	3.768	3.452	3.833	3.448	3.713
For 10 Sec. Period				3.347	3.765	3.448	3.830	3.444	3.710

Temperature -10°C

Table 8c. Signal Channel Response Data

α	Attenuation db	Peak Volts E_p	Integral, $\int = E_p / \alpha$	Peak A	Area A	Peak B	Area B	Peak C	Area C
5	60	3.33×10^{-4}	6.66×10^{-5}	.560	.632	.638	.990	.666	.544
5	50	1.06×10^{-3}	2.12×10^{-4}	1.26	1.24	1.37	1.57	1.37	1.13
5	40	3.33×10^{-3}	6.66×10^{-4}	2.00	1.88	2.11	2.20	2.10	1.81
5	30	1.06×10^{-2}	2.12×10^{-3}	2.72	2.52	2.84	2.85	2.83	2.46
5	20	3.33×10^{-2}	6.66×10^{-3}	3.49	3.19	3.57	3.52	3.56	3.15
5	10	1.06×10^{-1}	2.12×10^{-2}	4.24	3.86	4.29	4.20	4.29	3.84
5	0	3.33×10^{-1}	6.66×10^{-2}	5.00	4.54	5.02	4.89	5.02	4.54
3.2	60	3.33×10^{-4}	1.04×10^{-4}	.562	.737	.613	1.08	.650	.662
3.2	50	1.06×10^{-3}	3.31×10^{-4}	1.26	1.39	1.35	1.73	1.36	1.31
3.2	40	3.33×10^{-3}	1.04×10^{-3}	2.00	2.06	2.10	2.38	2.10	1.98
3.2	30	1.06×10^{-2}	3.31×10^{-3}	2.74	2.71	2.83	3.04	2.82	2.66
3.2	20	3.33×10^{-2}	1.04×10^{-2}	3.49	3.38	3.56	3.71	3.55	3.35
3.2	10	1.06×10^{-1}	3.31×10^{-2}	4.24	4.05	4.28	4.39	4.28	4.05
3.2	0	3.33×10^{-1}	1.04×10^{-1}	4.99	4.74	5.00	5.08	5.01	4.75
1.4	60	3.33×10^{-4}	2.38×10^{-4}	.477	.840	.527	1.16	.539	.759
1.4	50	1.06×10^{-3}	7.57×10^{-4}	1.16	1.62	1.23	1.94	1.23	1.52
1.4	40	3.33×10^{-3}	2.38×10^{-3}	1.89	2.31	1.97	2.63	1.96	2.22
1.4	30	1.06×10^{-2}	7.57×10^{-3}	2.63	2.98	2.69	3.30	2.69	2.91
1.4	20	3.33×10^{-2}	2.38×10^{-2}	3.37	3.65	3.41	3.97	3.41	3.60
1.4	10	1.06×10^{-1}	7.57×10^{-2}	4.12	4.32	4.14	4.65	4.14	4.30
1.4	0	3.33×10^{-1}	2.38×10^{-1}	4.88	4.88	4.86	5.20	4.87	4.83

Temperature 50°C

Table 9. Experiment Status Voltage Data

Gain Status Steps	Gain Status Voltage	Output at 25° C		
		Video A	Video B	Video C
1	.1730	.20	.20	1.75
2	.3416	.20	.20	.70
3	.5031	.20	1.75	.20
4	.6716	.20	1.75	1.75
5	.8339	.20	1.75	.70
6	1.003	.20	.70	.20
7	1.164	.20	.70	1.75
8	1.333	.20	.70	.70
9	1.466	1.75	.20	.20
10	1.635	1.75	.20	1.75
11	1.796	1.75	.20	.70
12	1.964	1.75	1.75	.20
13	2.127	1.75	1.75	1.75
14	2.295	1.75	1.75	.70
15	2.457	1.75	.70	.20
16	2.625	1.75	.70	1.75
17	2.756	1.75	.70	.70
18	2.924	.70	.20	.20
19	3.086	.70	.20	1.75
20	3.254	.70	.20	.70
21	3.416	.70	1.75	.20
22	3.585	.70	1.75	1.75
23	3.746	.70	1.75	.70
24	3.914	.70	.70	.20
25	4.048	.70	.70	1.75
26	4.216	.70	.70	.70
27	5.205	.20	.20	.20

Table 10. Gain State Data

Gain Status Steps	CHANNEL			Status Output Volts
	A	B	C	
1	L	L	H	.173
2	L	L	M	.346
3	L	H	L	.503
4	L	H	H	.671
5	L	H	M	.833
6	L	M	L	1.00
7	L	M	H	1.16
8	L	M	M	1.33
9	H	L	L	1.46
10	H	L	H	1.63
11	H	L	M	1.79
12	H	H	L	1.96
13	H	H	H	2.12
14	H	H	M	2.29
15	H	M	L	2.45
16	H	M	H	2.62
17	H	M	M	2.75
18	M	L	L	2.92
19	M	L	H	3.08
20	M	L	M	3.25
21	M	H	L	3.41
22	M	H	H	3.58
23	M	H	M	3.74
24	M	M	L	3.91
25	M	M	H	4.04
26	M	M	M	4.21
27	L	L	L	5.20

Low Gain (L) = 6

Medium Gain (M) = 21

High Gain (H) = 53

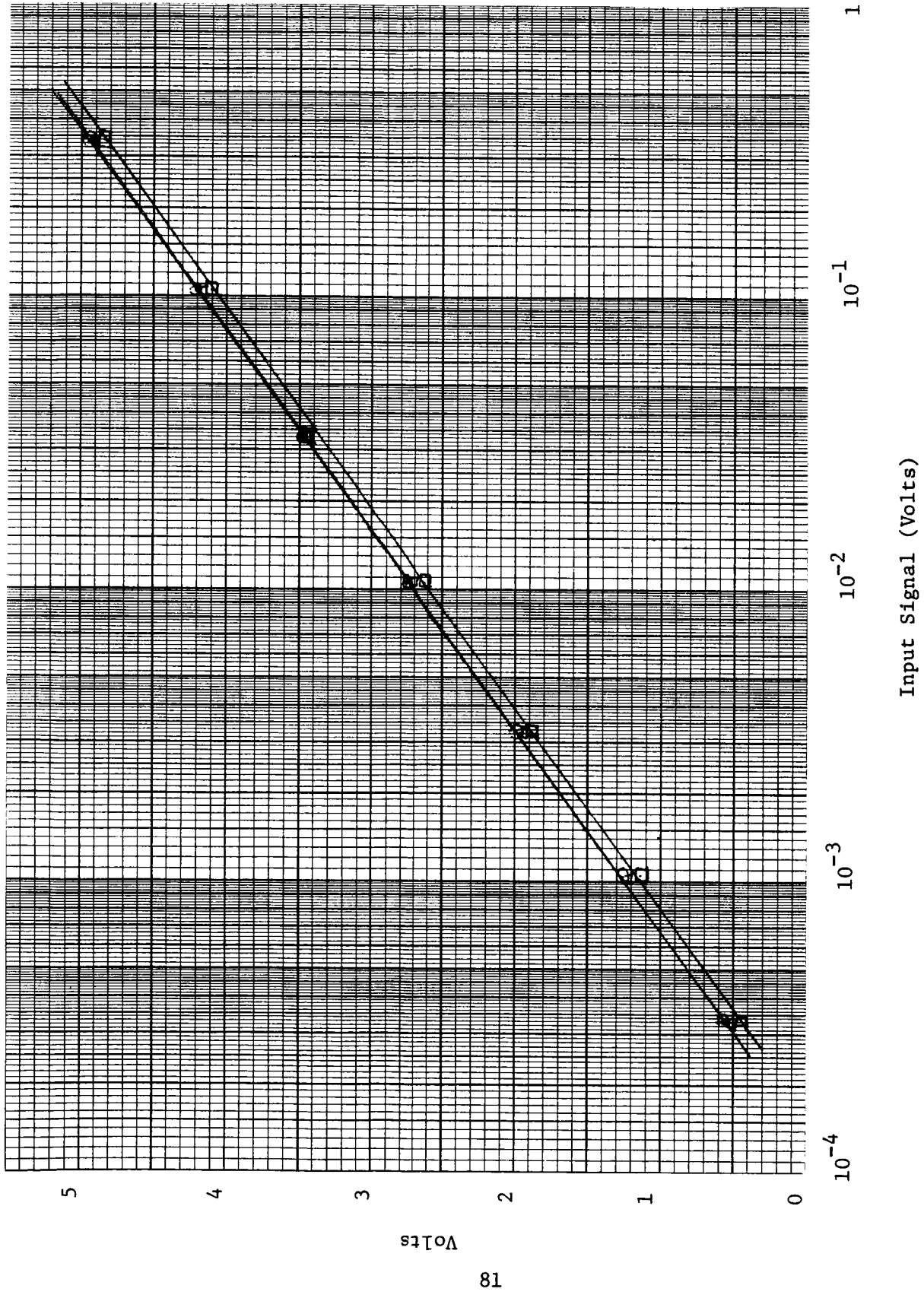


Figure 20. Electronic Calibration, Peak A. Ambient Temperature and 3 Values of α
 Abscissa for Gain 21; x 21/6 for Gain 6; x 21/53 for Gain 53.

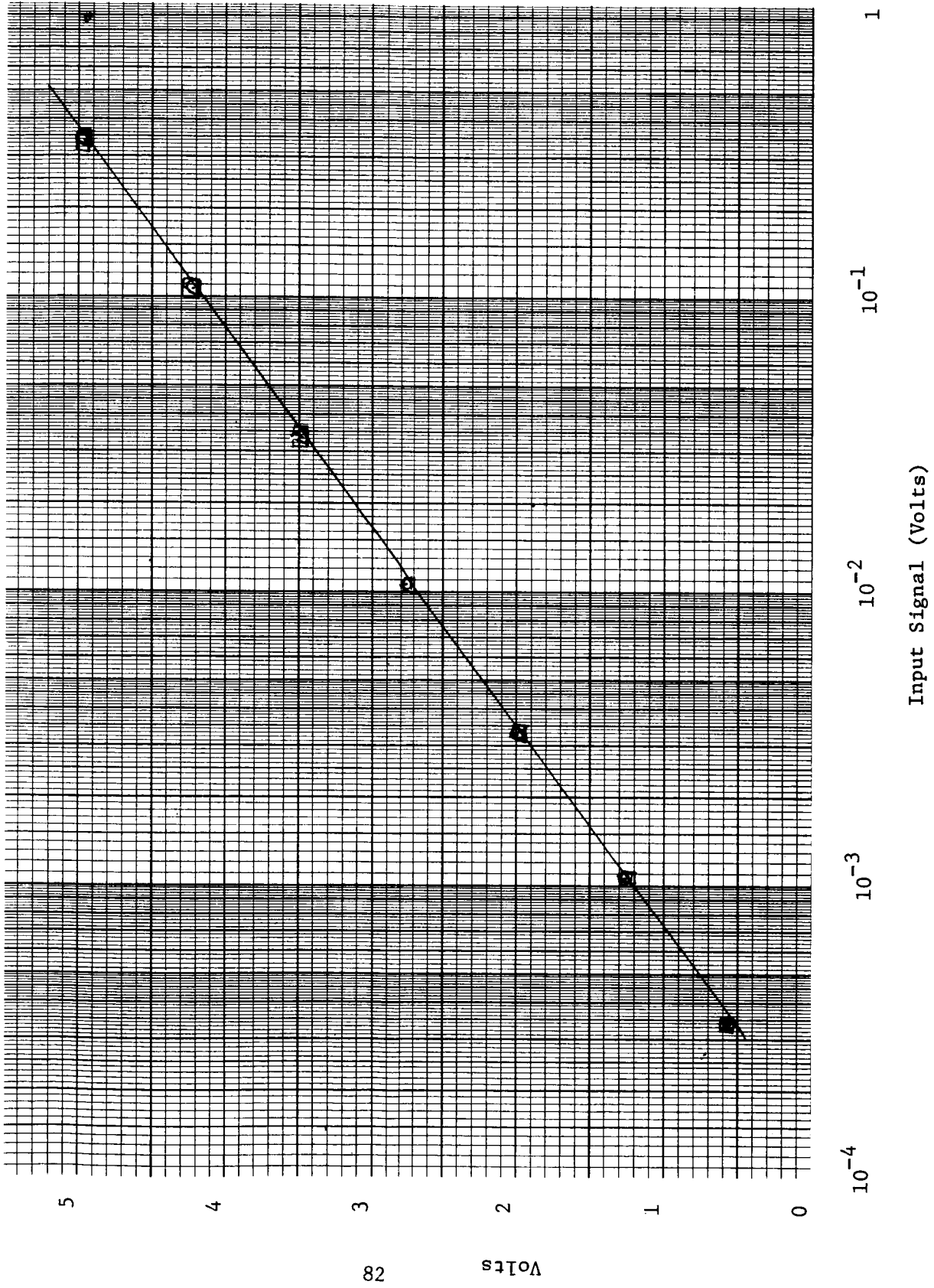


Figure 21. Electronic Calibration, Peak A. 1 Value of α , 3 Temperatures. Abscissa for Gain 21; x 21/6 for Gain 6; x 21/53 for Gain 53.

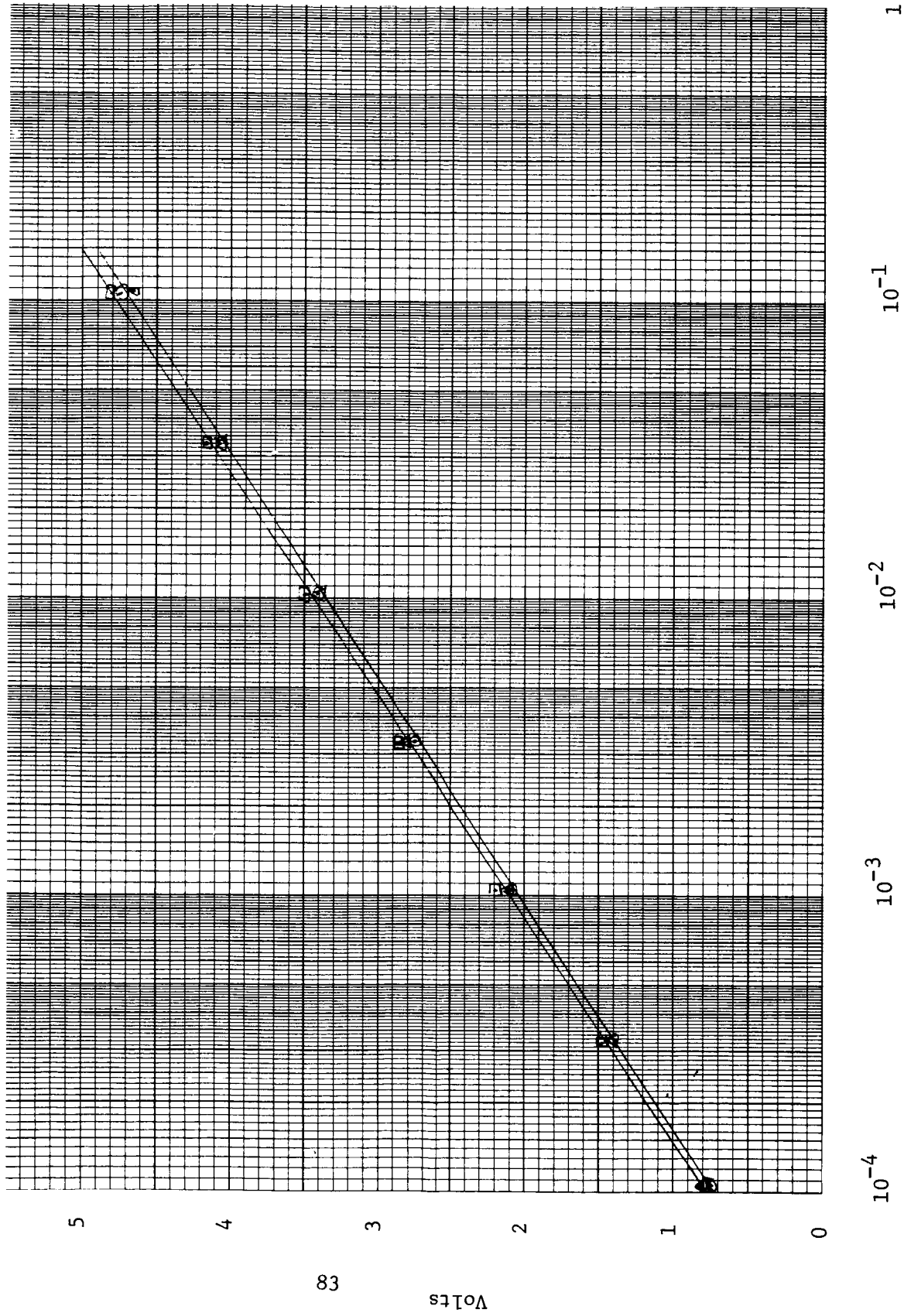


Figure 22. Electronic Calibration, Area A. 1 Value of α , 3 Temperatures. Abscissa for Gain 21; x 21/6 for Gain 6; x 21/53 for Gain 53.

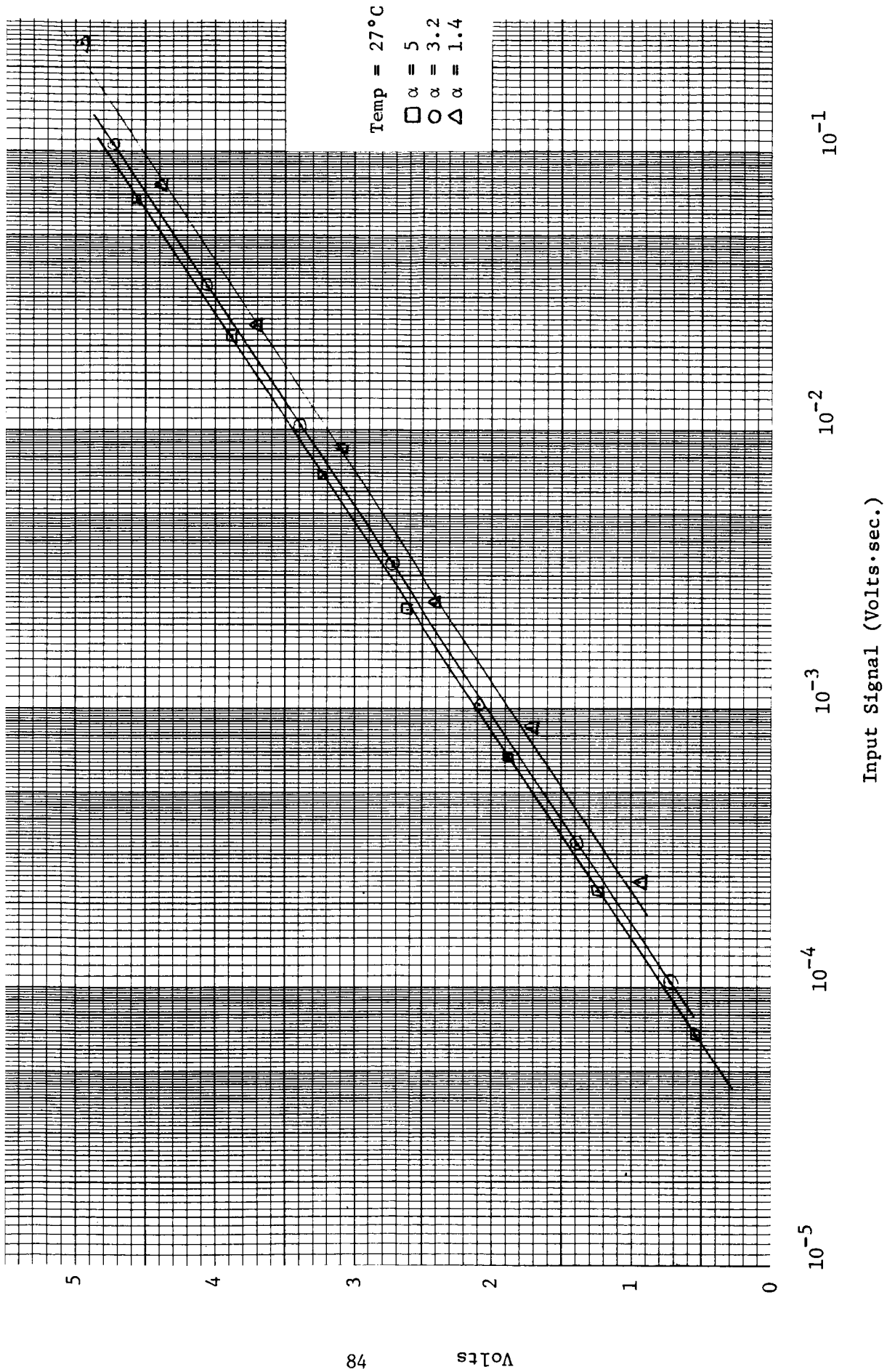


Figure 23. Electronic Calibration, Area A. Ambient Temperature and 3 Values of α .
 Abscissa for Gain 21; x 21/6 for Gain 6; x 21/53 for Gain 53.

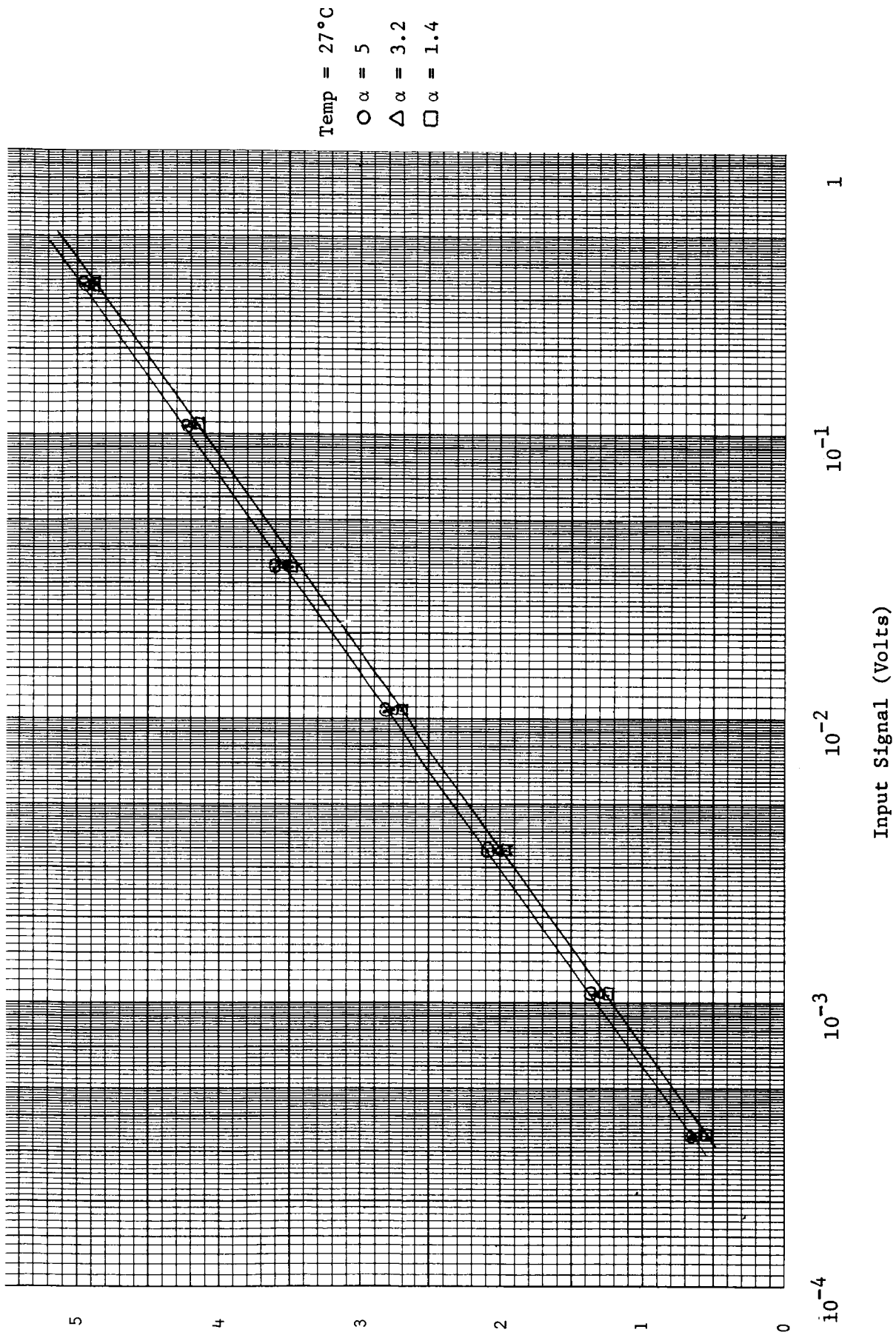


Figure 24. Electronic Calibration, Peak B. Ambient Temperature and 3 Values of α .
 Abscissa for Gain 21; x 21/6 for Gain 6; x 21/53 for Gain 53.

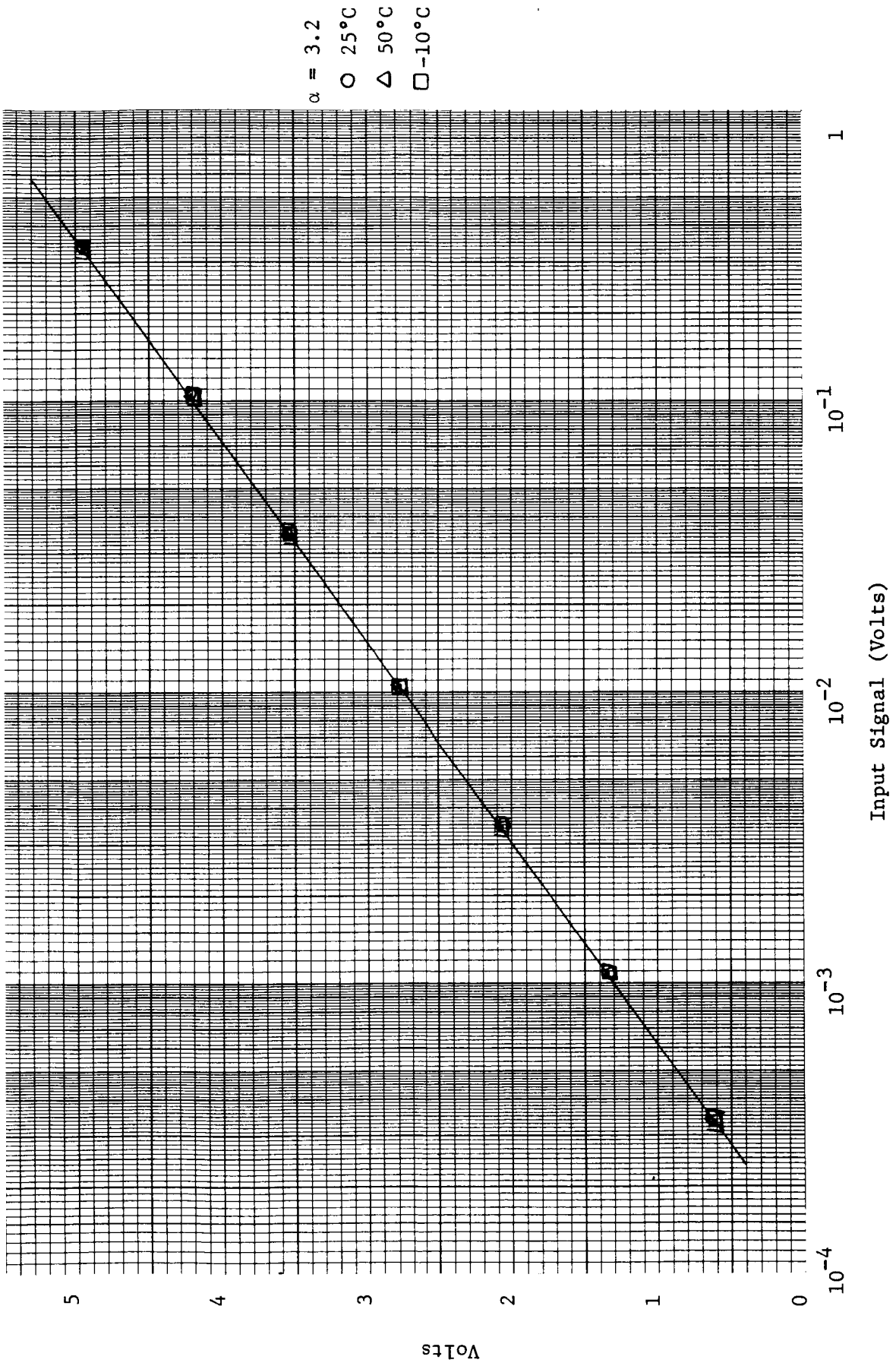


Figure 25. Electronic Calibration, Peak B. 1 Value of α , 3 Temperatures. Abscissa for Gain 21; x 21/6 for Gain 6; x 21/53 for Gain 53.

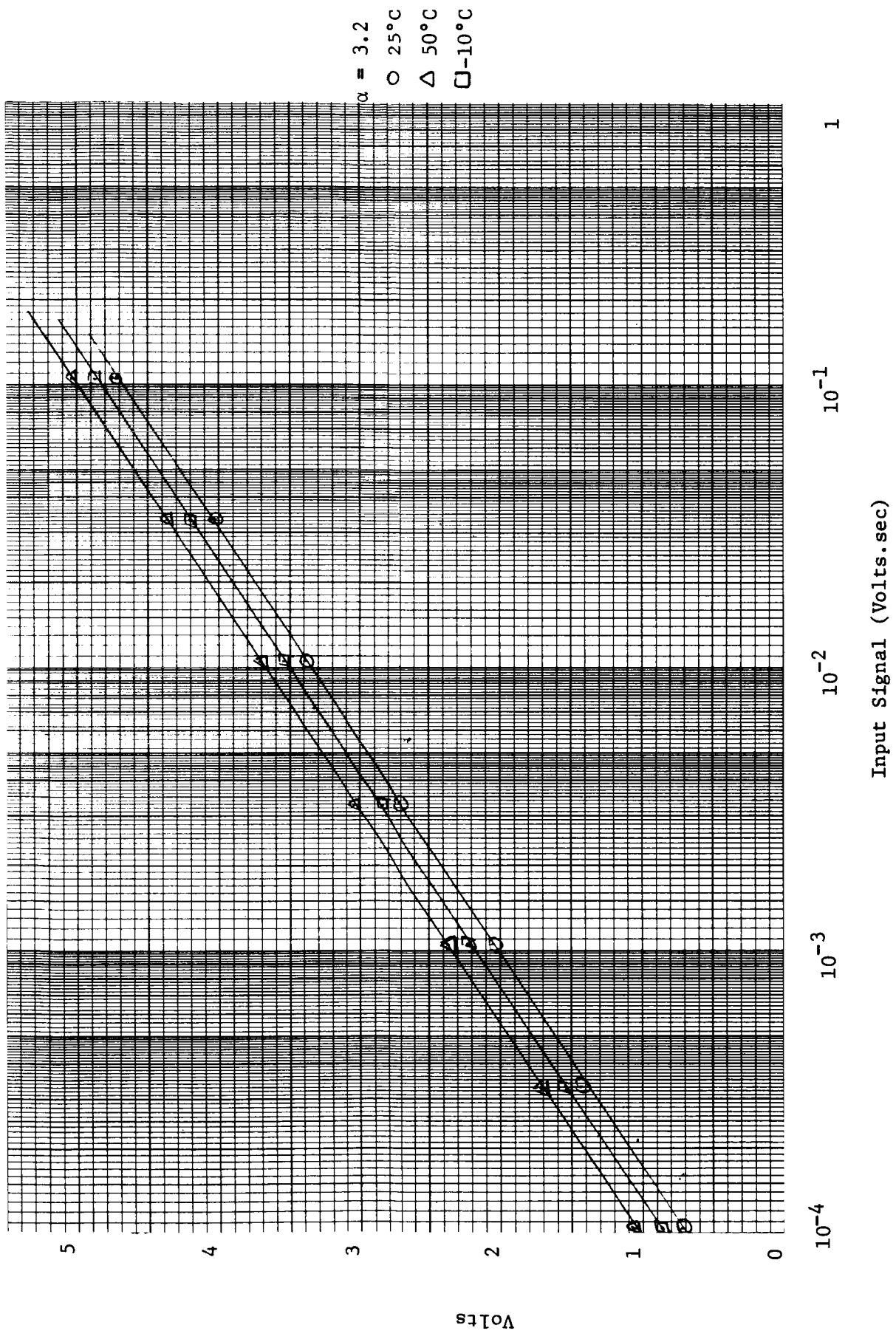


Figure 26. Electronic Calibration, Area B. 1 Value of α , 3 Temperatures. Abscissa for Gain 21; x 21/6 for Gain 6; x 21/53 for Gain 53.

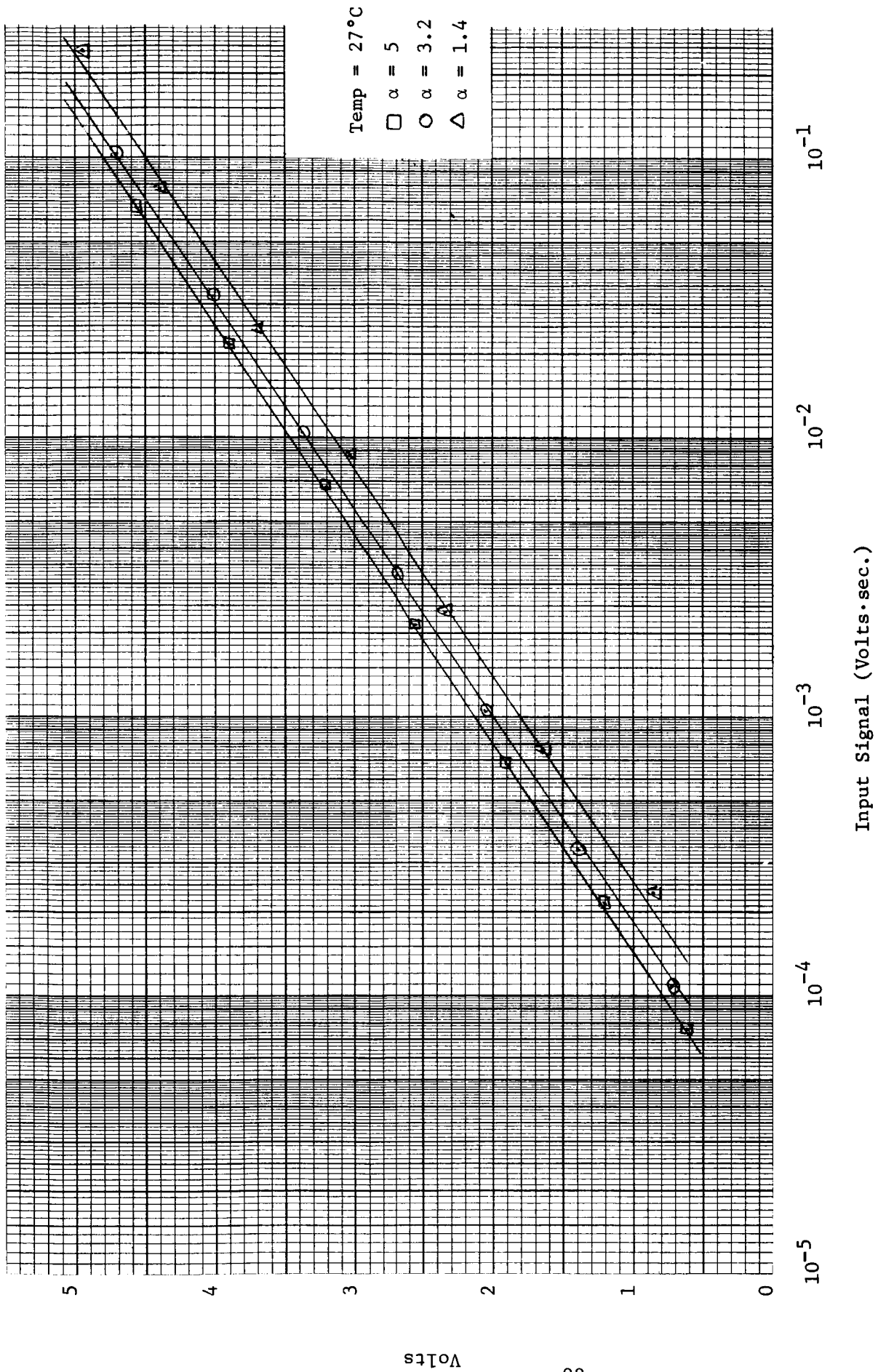


Figure 27. Electronic Calibration, Area B. Ambient Temperature and 3 Values of α .
 Abscissa for Gain 21; x 21/6 for Gain 6; x 21/53 for Gain 53.

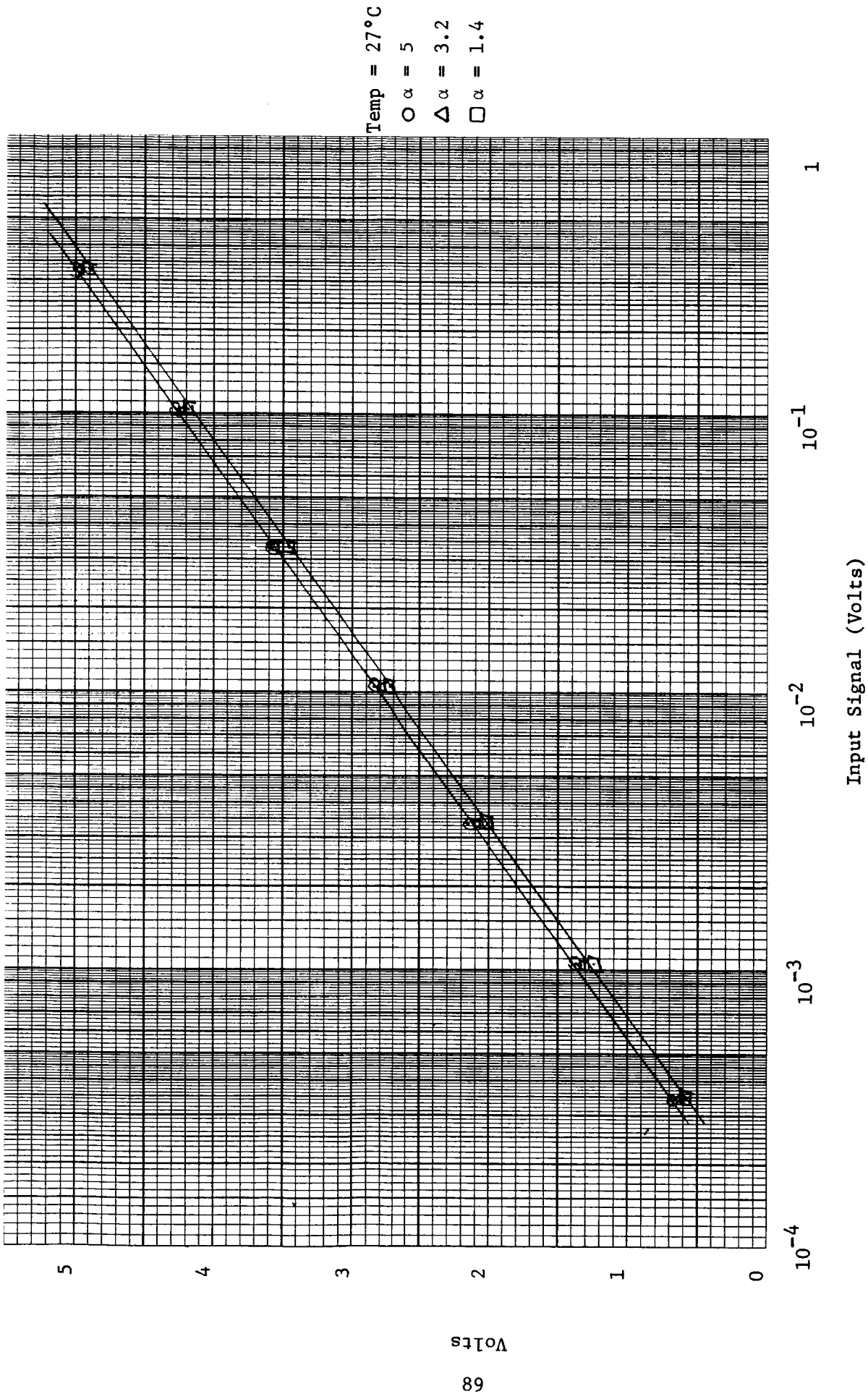


Figure 28. Electronic Calibration, Peak C. Ambient Temperature and 3 Values of α .
 Abscissa for Gain 21; x 21/6 for Gain 6; x 21/53 for Gain 53.

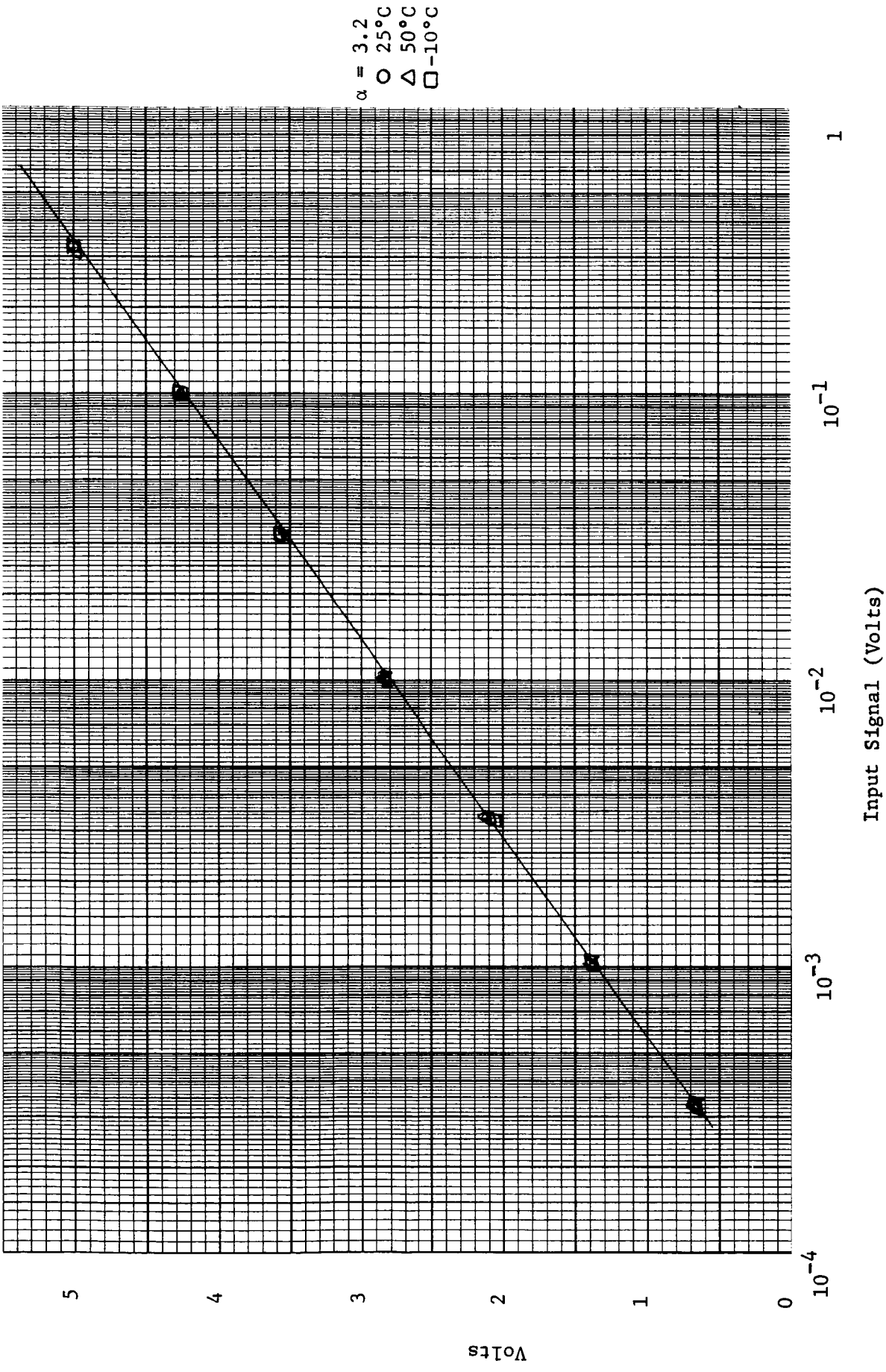


Figure 29. Electronic Calibration, Peak C. 1 Value of α , 3 Temperatures. Abscissa for Gain 21; x 21/6 for Gain 6; x 21/53 for Gain 53.

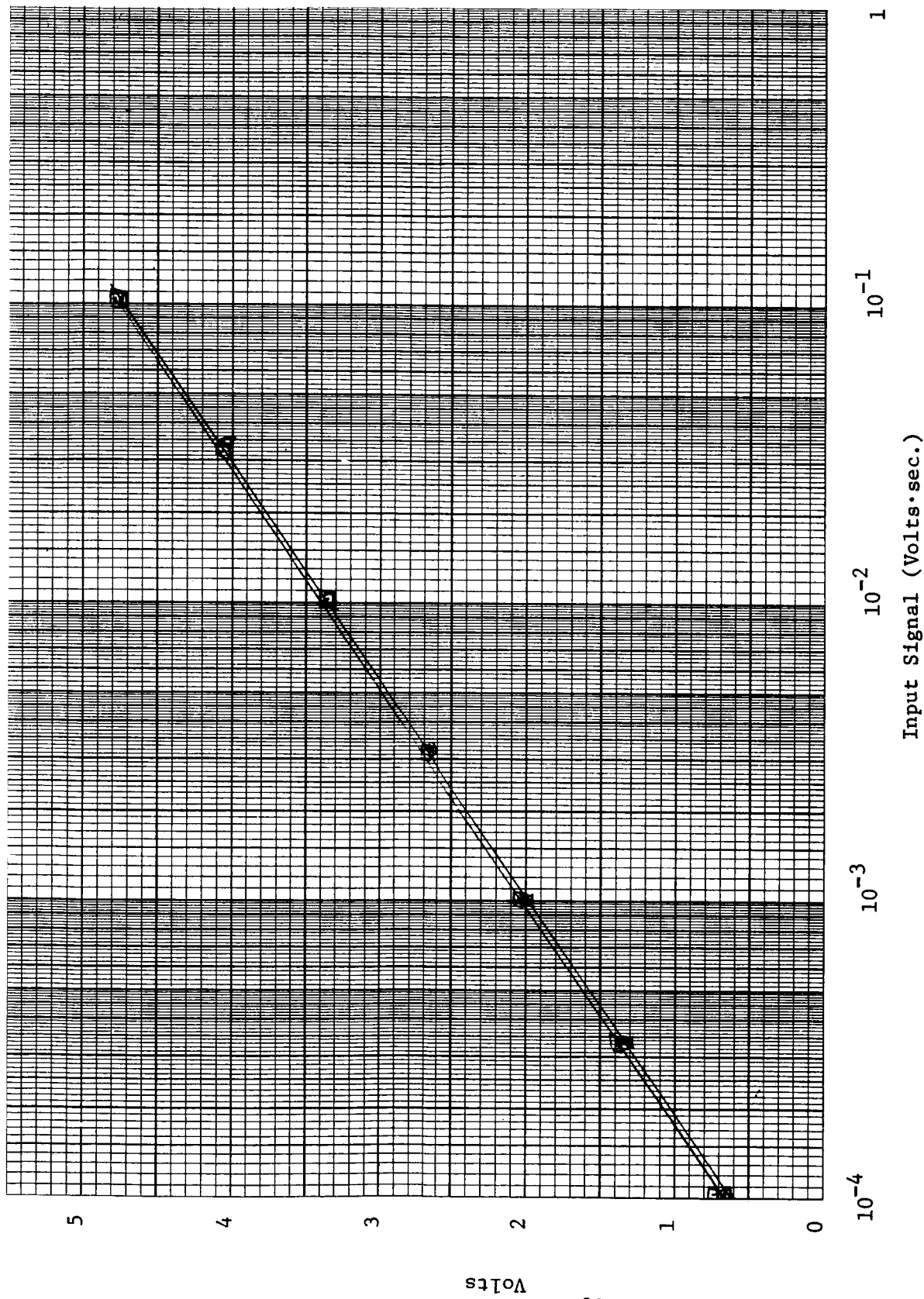


Figure 30. Electronic Calibration, Area C. 1 Value of α , 3 Temperatures. Abscissa for Gain 21; x 21/6 for Gain 6; x 21/53 for Gain 53.

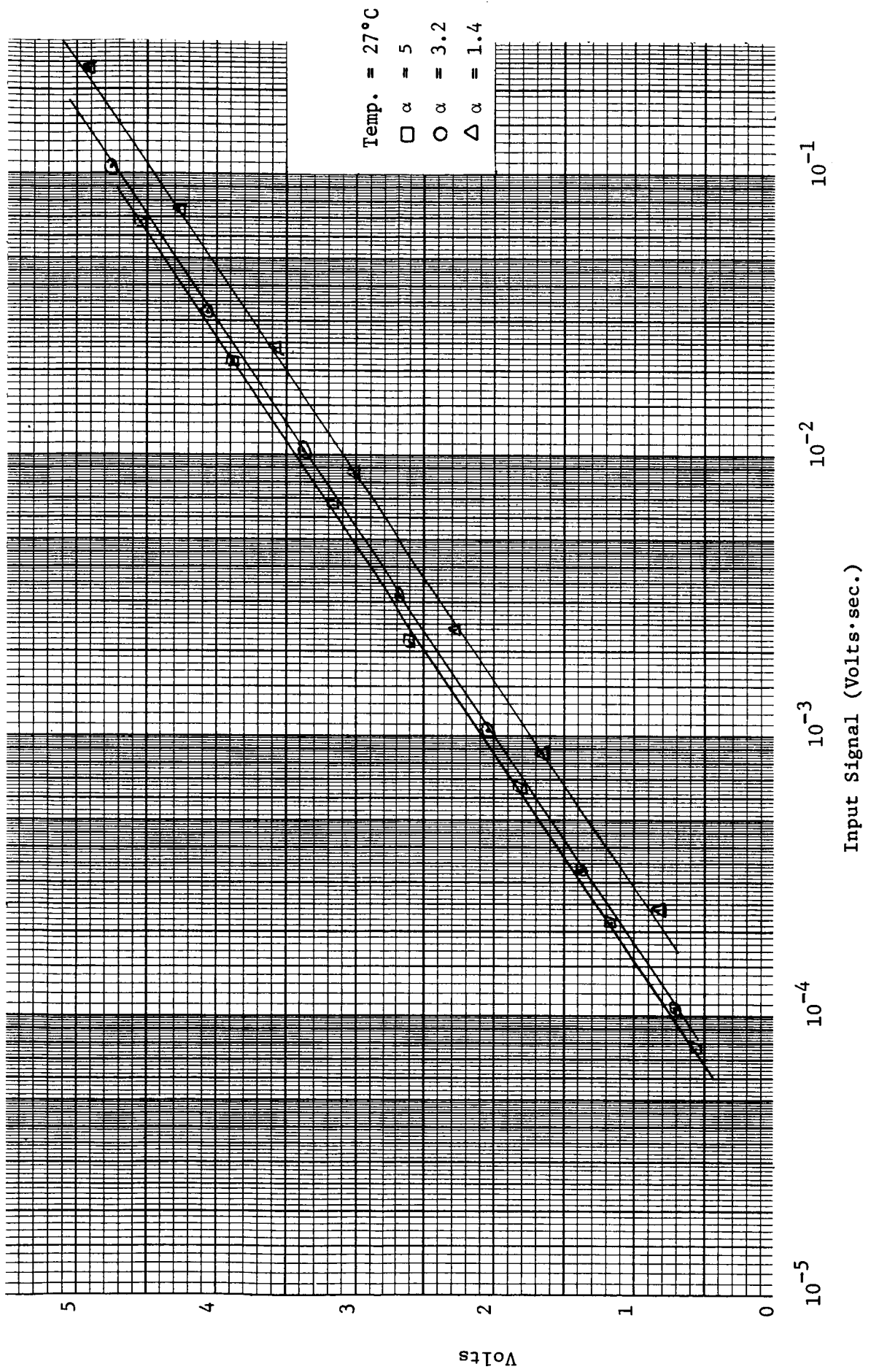


Figure 31. Electronic Calibration, Area C. Ambient Temperature and 3 Values of α .
 Abscissa for Gain 21; x 21/6 for Gain 6; x 21/53 for Gain 53.

6.1.4 Photodiode Circuit Tests

The photodiode circuit test data are given below. All functions perform as designed for this circuit. The input current should drop to $\sim .1A$ when the + 12V and - 12V are turned off.

Input Voltage for Turn Off	49.23 mv	-10° C
	51.72 mv	27° C
	49.7 mv	50° C

Experiment Status Voltage, On State	3.746 V
Experiment Status Voltage, Off State	- .336 V
Experiment Status Voltage, Photodiode Voltage Returned to 0	3.746 V

28 V	Input Current, Photodiode < 53 mv (Exp. on)	.160 A
------	--	--------

28 V	Input Current, Photodiode > 53 mv (Exp. off)	.110 A
------	---	--------

6.1.5 Calibration Lamp Circuit Test

Pulse Duration	2 sec
Pulse Amplitude	.9 V
Pulse Repetition Time	6 minutes

6.2 SPECTRAL RESPONSE

The chart records from test 5.2.2 are shown in Figures 32-35. To determine the relative response, the data in the first four columns of Table 11 are taken from the spectral scans. Column T.C. is the thermocouple output normalized to identical system gain. The thermocouple is a "black" detector, i.e., its response is independent of wavelength. Therefore, when the MFA output voltages of columns A, B, and C are divided by the T.C. output, the result is the relative response of the experiment data channels to identical power levels at each wavelength. The last three columns are the results normalized to the maximum value which occurs in each column. This information will be used in conjunction with the absolute responsivity measurement and displayed graphically in a later section.

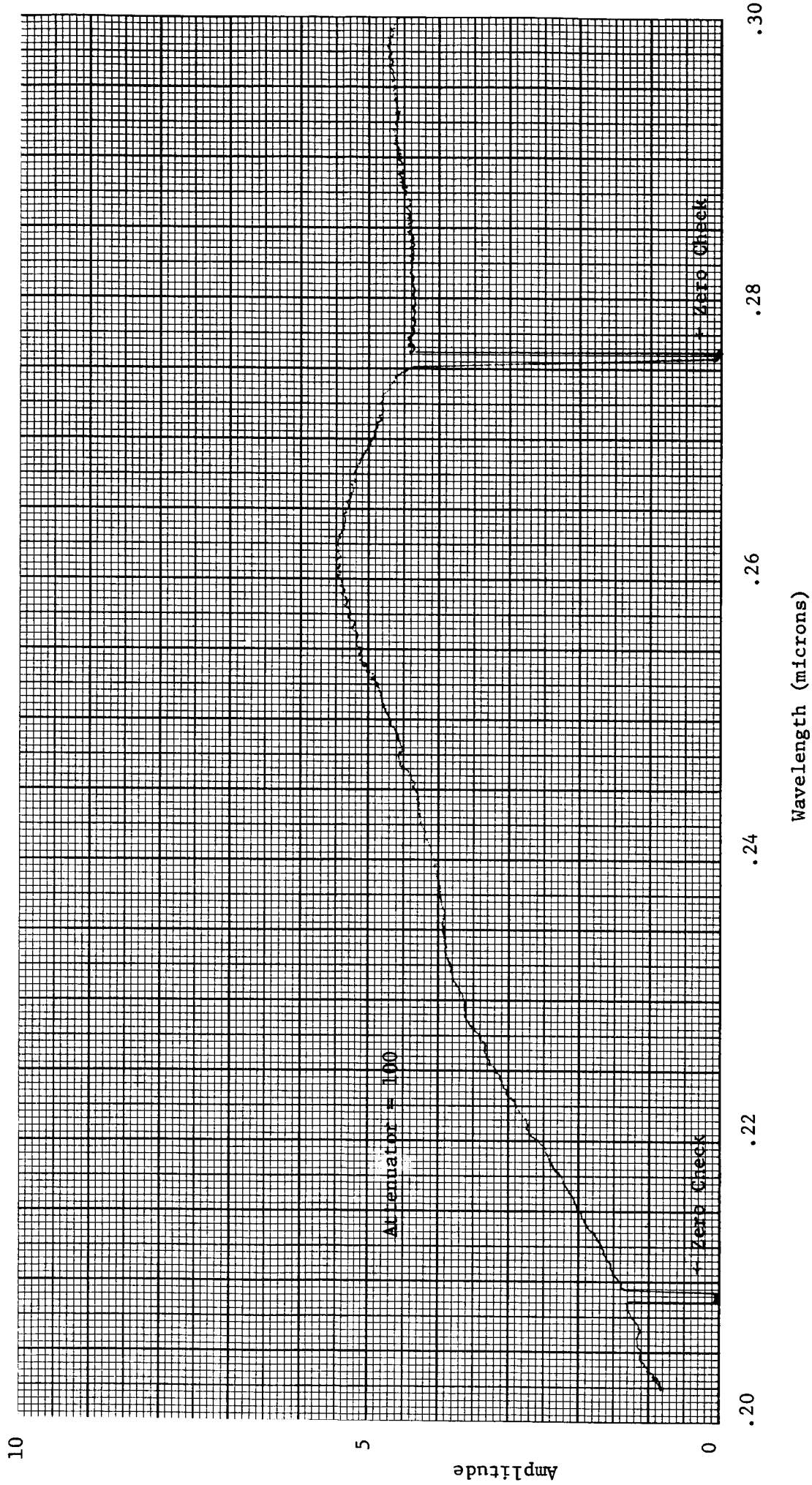


Figure 32A. Relative Response Test Data. Optical System Output Measured with Thermocouple Detector.

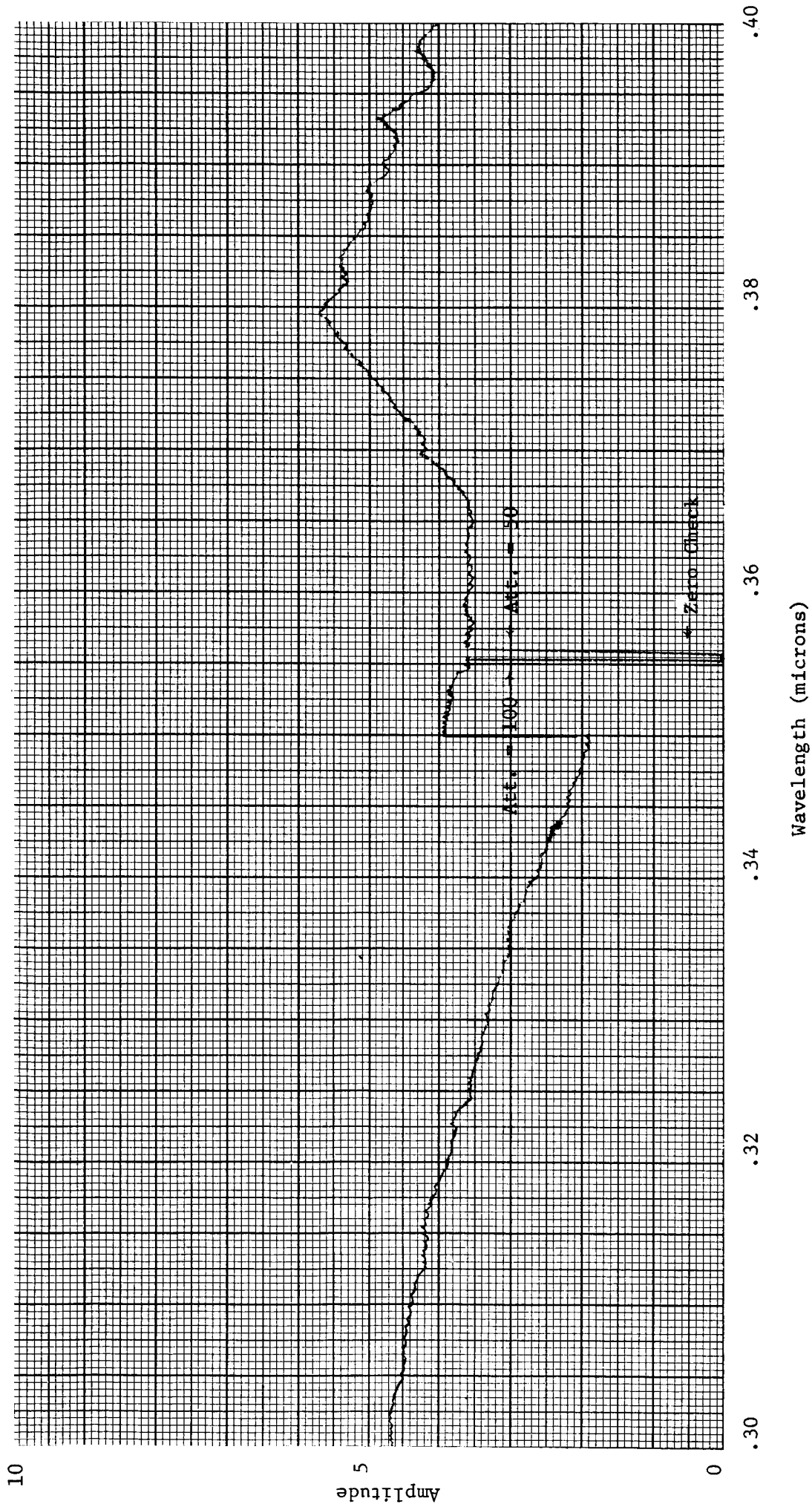


Figure 32B. Relative Response Test Data. Optical System Output Measured with Thermocouple Detector.

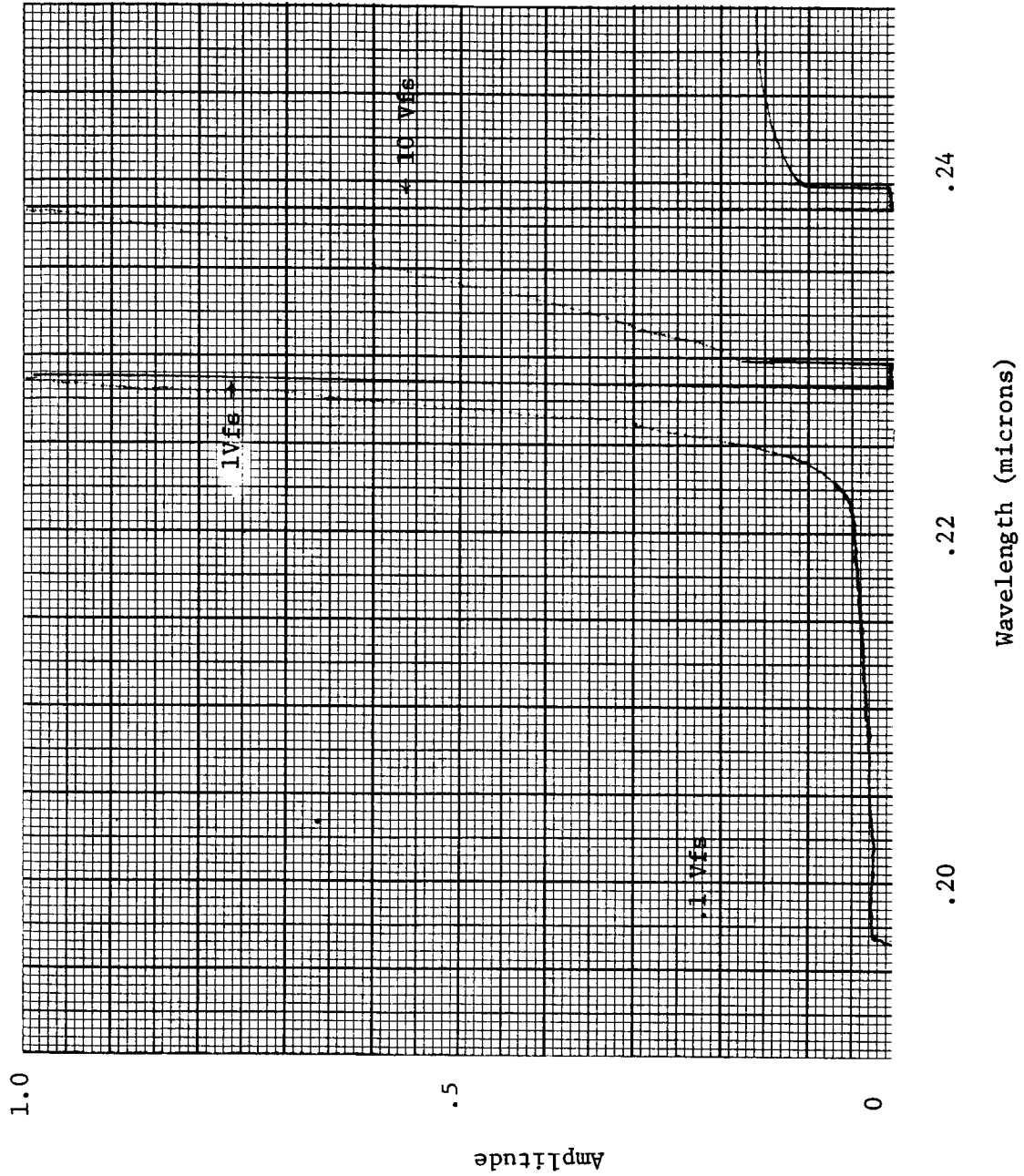


Figure 33A. Relative Response Test Data. Channel A Output Signal.

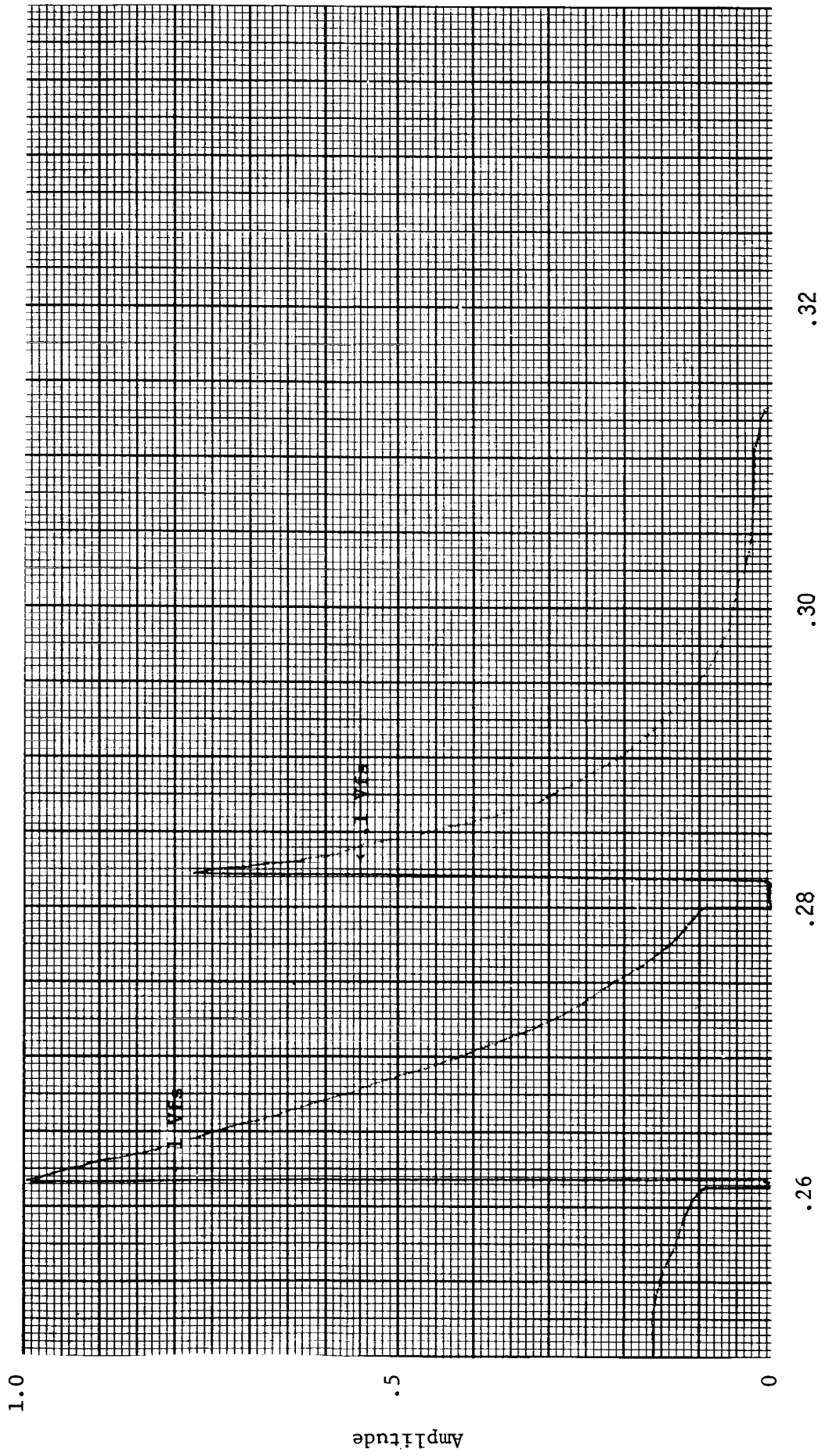


Figure 33B. Relative Response Test Data. Channel A Output Signal

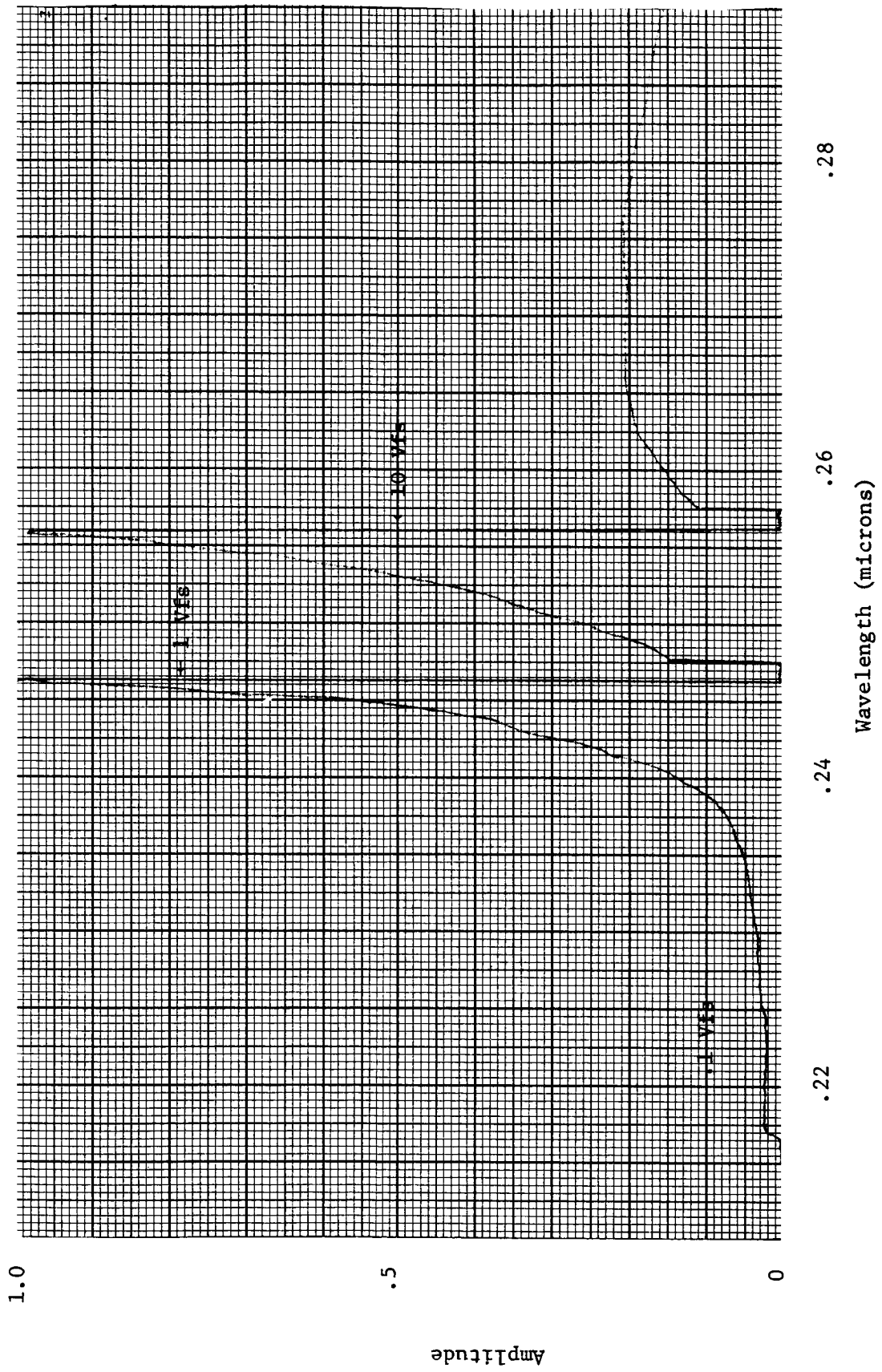


Figure 34A. Relative Response Test Data. Channel B Output Signal.

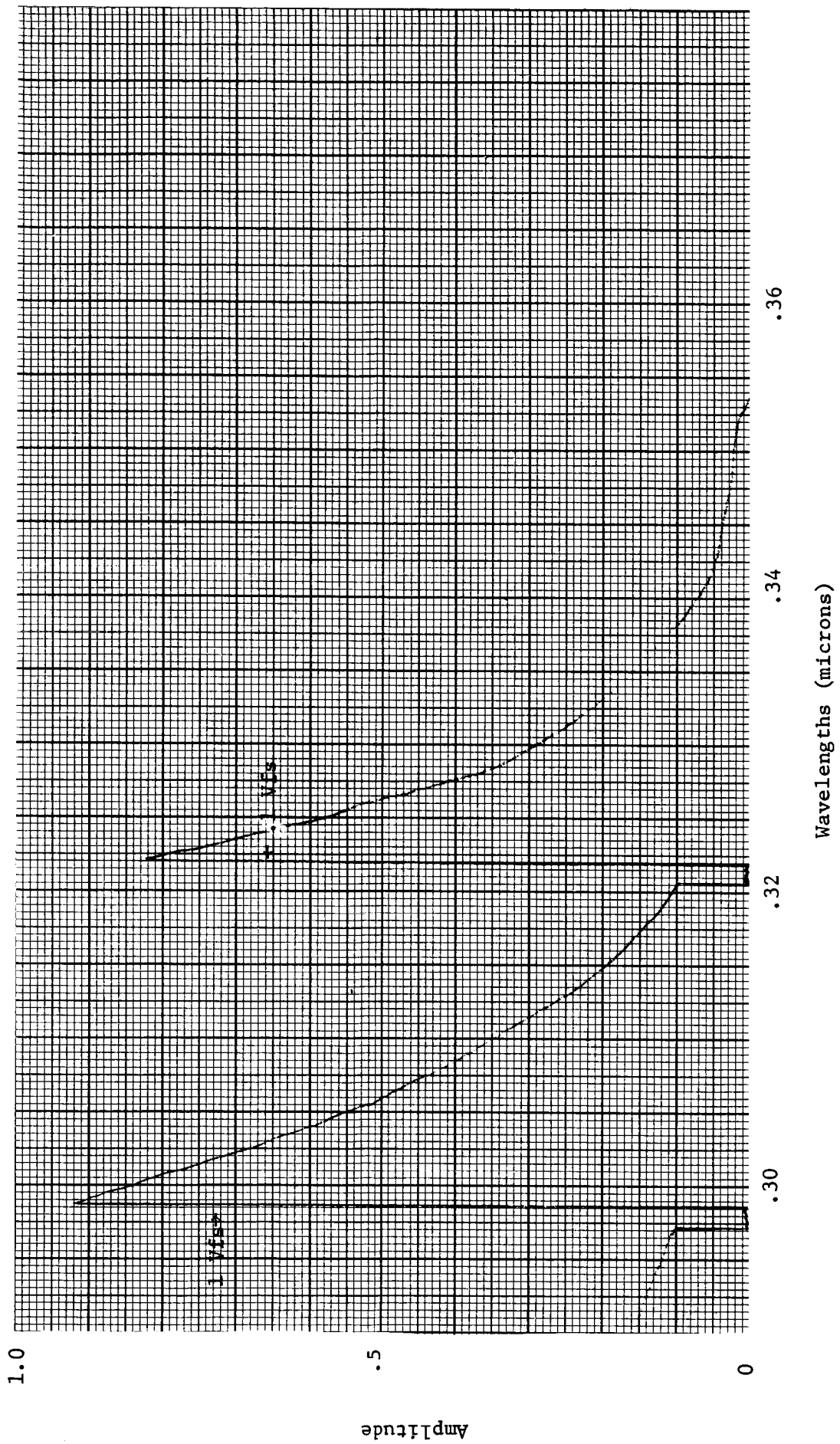


Figure 34B. Relative Response Test Data. Channel B Output Signal.

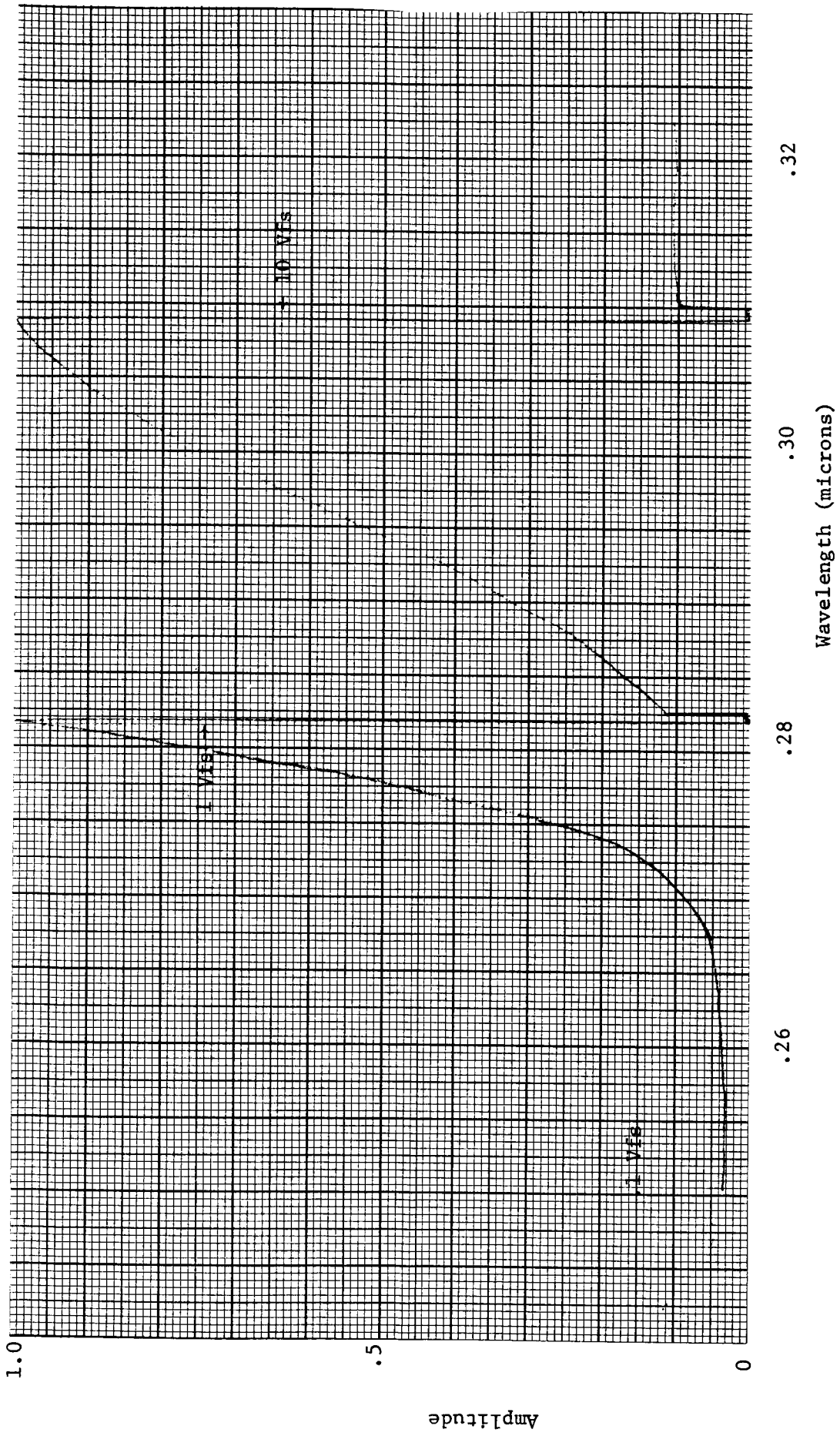


Figure 35A. Relative Response Test Data. Channel C Output Signal.

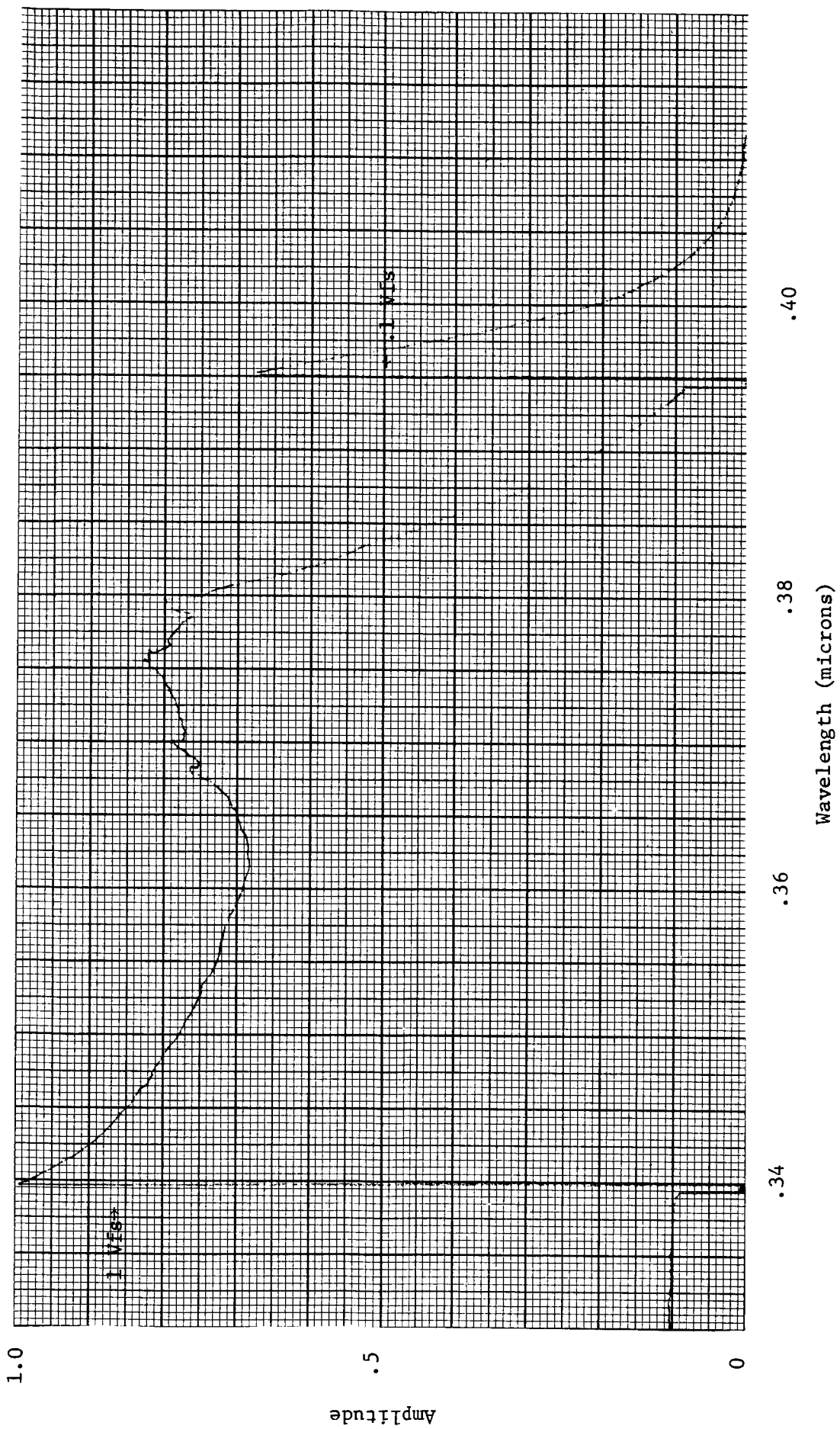


Figure 35B. Relative Response Test Data. Channel C Output Signal.

Table 11. Relative Spectral Response

λ , microns	T.C.	A, volts	B, volts	C, volts	A'	B'	C'
.2200	25.5	.004			.0047		
.2300	38	0.17	.004		.0133	.0024	
.2350	39	0.60			.456		
.2400	42	1.05	.015		.741	.008	
.2450	43	1.45	.067		1.00	.035	
.2500	47	1.55	0.26	.003	.978	.125	.0016
.2550	52	1.41		.003	.804		.0015
.2600	54	1.08	1.58	.0035	.593	.660	.0017
.2650	53		2.08	.0047		.886	.0023
.2700	49	0.41	2.10	.0078	.248	.967	.0041
.2750	45			.0265			.0151
.2800	44	.095	1.95	.075	.064	1.00	.0437
.2850	43	.045	1.70	.168	.031	.892	.1000
.2900	45	.021	1.48	.335	.014	.742	.191
.3000	46	.005	0.85	.760	.003	.417	.424
.3050	45		0.56	.920		.281	.524
.3100	43.5	.002	0.35	1.00	.0014	.182	.589
.3150	41		0.20	1.04		.110	.650
.3200	38.5		0.11	1.04		.064	.693
.3250	35		.058	1.04		.037	.762
.3300	32.5		.030	1.04		.021	.821
.3350	30		.015	1.04		.011	.889
.3400	26		.007	.965		.006	.952
.3500	20		.002	.780		.0023	1.00
.3600	18			.690			.983
.3700	20.5			.770			.963
.3800	27			.715			.679
.3900	23.5			.210			.229
.4000	20			.0205			.026
.4100	19.5			.0023			.003

6.3 FIELD-OF-VIEW

The experimental data observed for test 5.2.3 are tabulated (Table 12) on the following 20 pages. These data can be used to present a detailed field-of-view map, or if desired, to plot relative response vs. angle along a given axis. Several field-of-view contours are presented in Figures 36-39 for the three data channels and the photodiode. For the data channels, these are the contours at 50% and 10% of maximum response. They are derived by glancing through the data to locate the maximum voltage output, and then systematically searching at each azimuth setting for the elevation (+ and -) at which the response has reached the desired fraction of the maximum. The + and - directions of azimuth and elevation are defined as follows: + azimuth is a clockwise rotation about the vertical axis of the instrument as observed from the top of the test fixture; + elevation is a clockwise rotation about the horizontal axis, viewed from the first quadrant of the X-Y coordinate system established by the two axes. The response functions are quite uniform, and correspond closely to the optical system design calculations. Small irregularities in the contours are most likely due to non-uniform response across the sensitive area of the photocathode. Also, the optical axes could be precisely centered with additional alignment and testing. (It can be seen that the optical centers are 2-3° from mechanical center.)

The photodiode graph shows a single contour, which is the point to which the response does not change from maximum. Within 1-2° from this point, the response drops rapidly to less than 10% of maximum.

Table 12. Field-of-View Data

MFA Data Channel A

Azimuth 0

Elevation (+)	Millivolts	Elevation (-)	Millivolts
2.5	393	0	393
5	384	2.5	407
7.5	369	5	429
10	324	7.5	434
12.5	288	10	424
15	186	12.5	355
17.5	82.6	15	234
19	28	16	192
		17	146
		18	63.7
		19	7.8

Azimuth + 5

Elevation (+)	Millivolts	Elevation (-)	Millivolts
2.5	395	0	408
5	383	2.5	417
7.5	356	5	430
10	321	7.5	428
12.5	272	10	413
15	168	12.5	335
17.5	78.2	15	213
19	14.6	17.5	76
		18	36

Table 12

MFA Data Channel A

Azimuth + 10

Elevation (+)	Millivolts	Elevation (-)	Millivolts
2.5	363	0	382
5	350	2.5	387
7.5	334	5	397
10	269	7.5	372
12.5	185	10	307
15	99	12.5	211
16	67	15	97.5
16.5	42	16	20

Azimuth + 15

Elevation (+)	Millivolts	Elevation (-)	Millivolts
2.5	268	0	275
5	233	2.5	269
7.5	182	5	244
10	125	7.5	196
12	72	10	139
13	34	12	42.3
		12.5	24

Table 12

MFA Data Channel A

Azimuth + 17.5

Elevation (+)	Millivolts	Elevation (-)	Millivolts
2.5	144	0	153
5	123	2.5	154
7.5	83	5	136
10	15	7.5	72
		8.5	34
		9	26

Azimuth + 19

Elevation (+)	Millivolts	Elevation (-)	Millivolts
2.5	76	0	80
5	45	2.5	52.5
6	25	3	45
		4	30

Table 12

MFA Data Channel A

Azimuth + 19.5

Elevation (+)	Millivolts	Elevation (-)	Millivolts
1	29	0	50
		1	26

Azimuth - 5

Elevation (+)	Millivolts	Elevation (-)	Millivolts
2.5	392	0	404
5	366	2.5	411
7.5	337	5	418
10	313	7.5	424
12.5	230	10	377
15	126	12.5	289
17.5	45	15	190
18	28	17.5	18

Table 12

MFA Data Channel A

Azimuth - 10

Elevation (+)	Millivolts	Elevation (-)	Millivolts
2.5	343	0	380
5	300	2.5	381
7.5	273	5	363
10	200	7.5	329
12.5	116	10	246
15	43	12.5	156
16	8	14	55.6
		15	15.6

Azimuth - 15

Elevation (+)	Millivolts	Elevation (-)	Millivolts
2.5	181	0	191
5	157	2.5	189
7.5	108	5	162
8	95	7.5	86.6
9	60	9	31.8
10	19		

Table 12

MFA Data Channel A

Azimuth - 17

Elevation (+)	Millivolts	Elevation (-)	Millivolts
2.5	70	0	79.5
5	29	2.5	50
		4	31.9

Azimuth - 18

Elevation (+)	Millivolts	Elevation (-)	Millivolts
		0	12

Table 12

MFA Data Channel B

Azimuth 0

Elevation (+)	Millivolts	Elevation (-)	Millivolts
5	488	0	484
10	463	5	500
12.5	430	7.5	465
15	290	10	421
16	254	12.5	281
17	221	14	221
18	120	15	168
19	34.5	16	100
		17	29.5

Azimuth + 5

Elevation (+)	Millivolts	Elevation (-)	Millivolts
5	528	0	525
7.5	528	5	517
10	503	7.5	483
12.5	443	10	460
15	300	12.5	266
17.5	187	15	150
18	109	16	48
18.5	59		

Table 12

MFA Data Channel B

Azimuth + 10

Elevation (+)	Millivolts	Elevation (-)	Millivolts
2.5	526	0	520
5	522	2.5	508
7.5	465	5	481
10	415	7.5	395
12.5	300	10	284
15	210	12.5	128
16	110	14	45
17	20		

Azimuth +15

Elevation (+)	Millivolts	Elevation (-)	Millivolts
5	293	0	322
7.5	263	2.5	270
10	185	5	232
12	60	7.5	126
		9	40

Table 12

MFA Data Channel B

Azimuth + 17

Elevation (+)	Millivolts	Elevation (-)	Millivolts
2.5	208	0	230
5	130	2.5	226
6	85	5	194
7	26	7.5	109
		8	76
		9	28

Azimuth - 5

Elevation (+)	Millivolts	Elevation (-)	Millivolts
5	456	0	466
7.5	433	5	438
10	418	10	308
12.5	323	12.5	208
14	265	15	94
15	230	16	18
16	198		
17	120		
18	30		

Table 12

MFA Data Channel B

Azimuth - 10

Elevation (+)	Millivolts	Elevation (-)	Millivolts
5	350	0	367
7.5	299	5	300
10	229	7	232
12.5	196	10	166
15	60	12.5	49
18	9	15	8

Azimuth - 12.5

Elevation (+)	Millivolts	Elevation (-)	Millivolts
5	177	0	233
7.5	139	5	220
10	56	7.5	192
		10	175
		12.5	64
		13	40

Table 12

MFA Data Channel B

Azimuth - 15

Elevation (+)	Millivolts	Elevation (-)	Millivolts
2.5	109	0	128
5	63	2.5	131
6	40	5	122
		7.5	75
		8	60
		9	30

Azimuth - 16.5

Elevation (+)	Millivolts	Elevation (-)	Millivolts
2	51	0	50
4	38	2	33

Table 12

MFA Data Channel C

Azimuth 0

Elevation (+)	Millivolts	Elevation (-)	Millivolts
2.5	996	0	983
5	992	2.5	976
7.5	995	5	968
10	984	7.5	975
12.5	915	10	905
15	824	12.5	754
17.5	597	15	489
19	438	17.5	250
20	350	18	95
21.5	100		

Azimuth + 5

Elevation (+)	Millivolts	Elevation (-)	Millivolts
2.5	1072	0	1026
5	1064	2.5	986
7.5	1102	5	1007
10	1084	7.5	947
12.5	1039	10	907
15	882	12.5	707
17.5	615	15	445
20	300	17.5	110
21	64	18	49

Table 12

MFA Data Channel C

Azimuth +10

Elevation (+)	Millivolts	Elevation (-)	Millivolts
7.5	1102	0	1050
5	1106	2.5	1002
7.5	1113	5	947
10	1114	7.5	840
12.5	964	10	664
15	720	12.5	425
17.5	434	15	193
19	74	16	60

Azimuth + 15

Elevation (+)	Millivolts	Elevation (-)	Millivolts
2.5	998	0	940
5	1003	2.5	832
7.5	981	5	712
10	855	7.5	520
12.5	645	10	371
15	290	12.5	120
16	81	13	45
17	40		

Table 12

MFA Data Channel C

Azimuth + 17.5

Elevation (+)	Millivolts	Elevation (-)	Millivolts
2.5	748	0	686
5	738	2.5	588
7.5	692	5	447
10	586	7.5	308
11	437	10	70
12	298		
13	142		
14	43		

Azimuth + 19.5

Elevation (+)	Millivolts	Elevation (-)	Millivolts
2.5	603	0	548
5	598	2.5	449
7.5	480	5	265
10	208	7	116
11	63	8	57

Table 12

MFA Data Channel C

Azimuth + 21

Elevation (+)	Millivolts	Elevation (-)	Millivolts
1	284	0	237
2	299	1	199
3	290	2	154
4	270	3	100
5	234	4	43
6	171		
7	83		
8	40		

Azimuth +22

Elevation (+)	Millivolts	Elevation (-)	Millivolts
		0	36

Table 12

MFA Data Channel C

Azimuth -5

Elevation (+)	Millivolts	Elevation (-)	Millivolts
2.5	851	0	871
5	804	2.5	887
7.5	804	5	922
10	861	7.5	873
12.5	810	10	811
15	596	12.5	587
17	445	15	400
18	379	17	77
19	295		
20	131		
20.5	58		

Azimuth - 10

Elevation (+)	Millivolts	Elevation (-)	Millivolts
2.5	796	0	746
5	783	2.5	712
7.5	701	5	626
10	563	7.5	616
12.5	427	10	450
15	318	12.5	353
17	100	15	35

Table 12

MFA Data Channel C

Azimuth - 15

Elevation (+)	Millivolts	Elevation (-)	Millivolts
2.5	396	0	397
5	384	2.5	372
7.5	319	5	317
10	226	7.5	245
11	167	9	100
12	90		
12.5	58		

Azimuth - 17.5

Elevation (+)	Millivolts	Elevation (-)	Millivolts
2.5	150	0	168
5	103	2.5	91
6	71		

Table 12

MFA Data Channel C

Azimuth - 18

Elevation (+)	Millivolts	Elevation (-)	Millivolts
1	88	0	91
2	85	1	71
3	76		
5	47		

Azimuth - 19

Elevation (+)	Millivolts	Elevation (-)	Millivolts
		0	31

Table 12

MFA Photodiode Sun Sensor

Azimuth - 7.5

Elevation (+)	Millivolts	Elevation (-)	Millivolts
11.5	537	0	537
12	363	8	537
12.5	120	9	132
13	42	10	36

Azimuth (+)	Millivolts	Azimuth (-)	Millivolts
14.5	537	11.5	537
15	195	12	283
15.5	39	12.5	48

Table 12

MFA Photodiode Sun Sensor

Azimuth 0

Elevation (+)	Millivolts	Elevation (-)	Millivolts
14	537	0	537
15	427	11	537
15.5	53	12	301
		12.5	79

Azimuth + 7.5

Elevation (+)	Millivolts	Elevation (-)	Millivolts
13.5	537	0	537
14	323	10	537
14.5	85	10.5	401
15	39	11	93
		11.5	

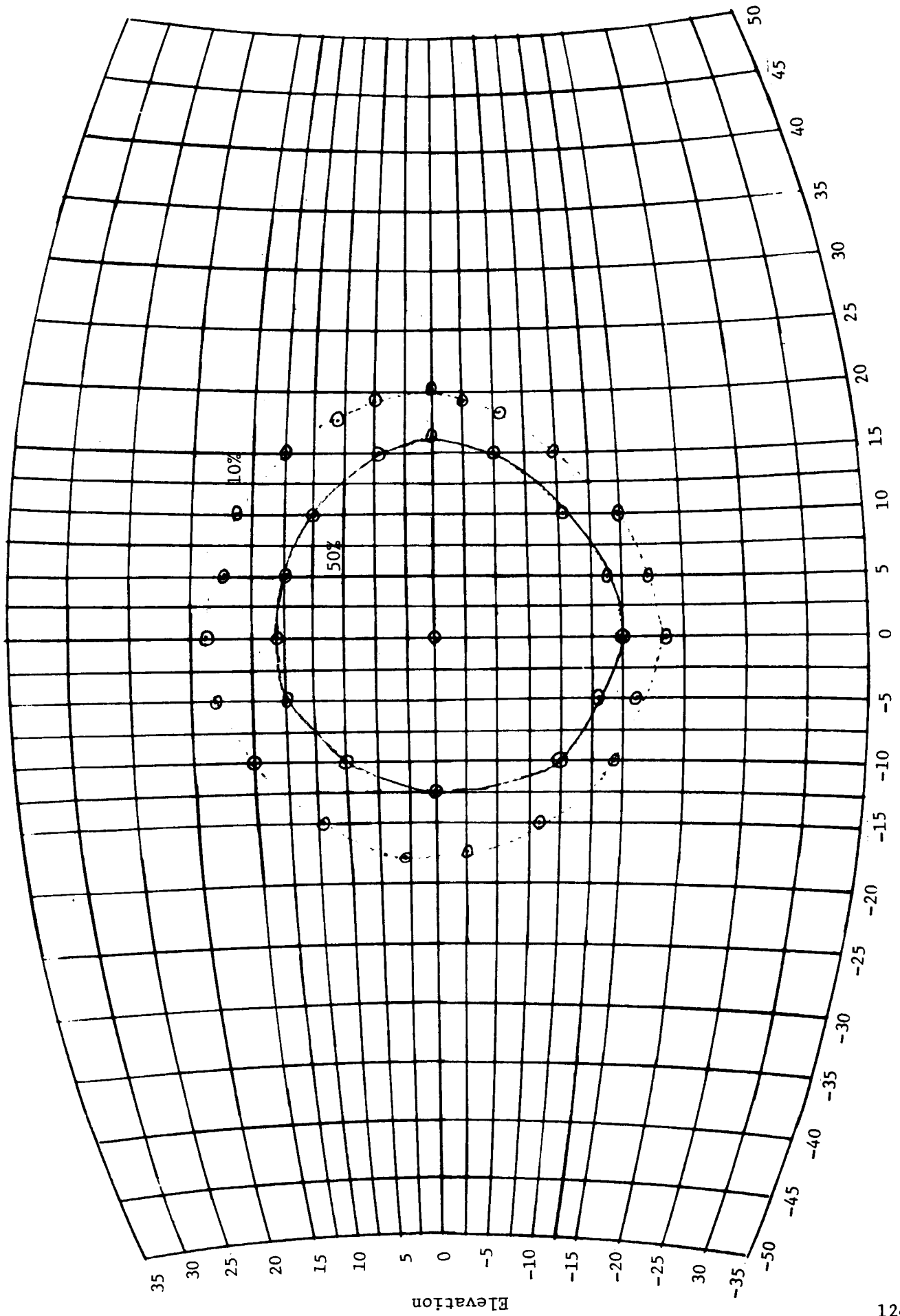


Figure 36. Field-of-View Contours, Channel A

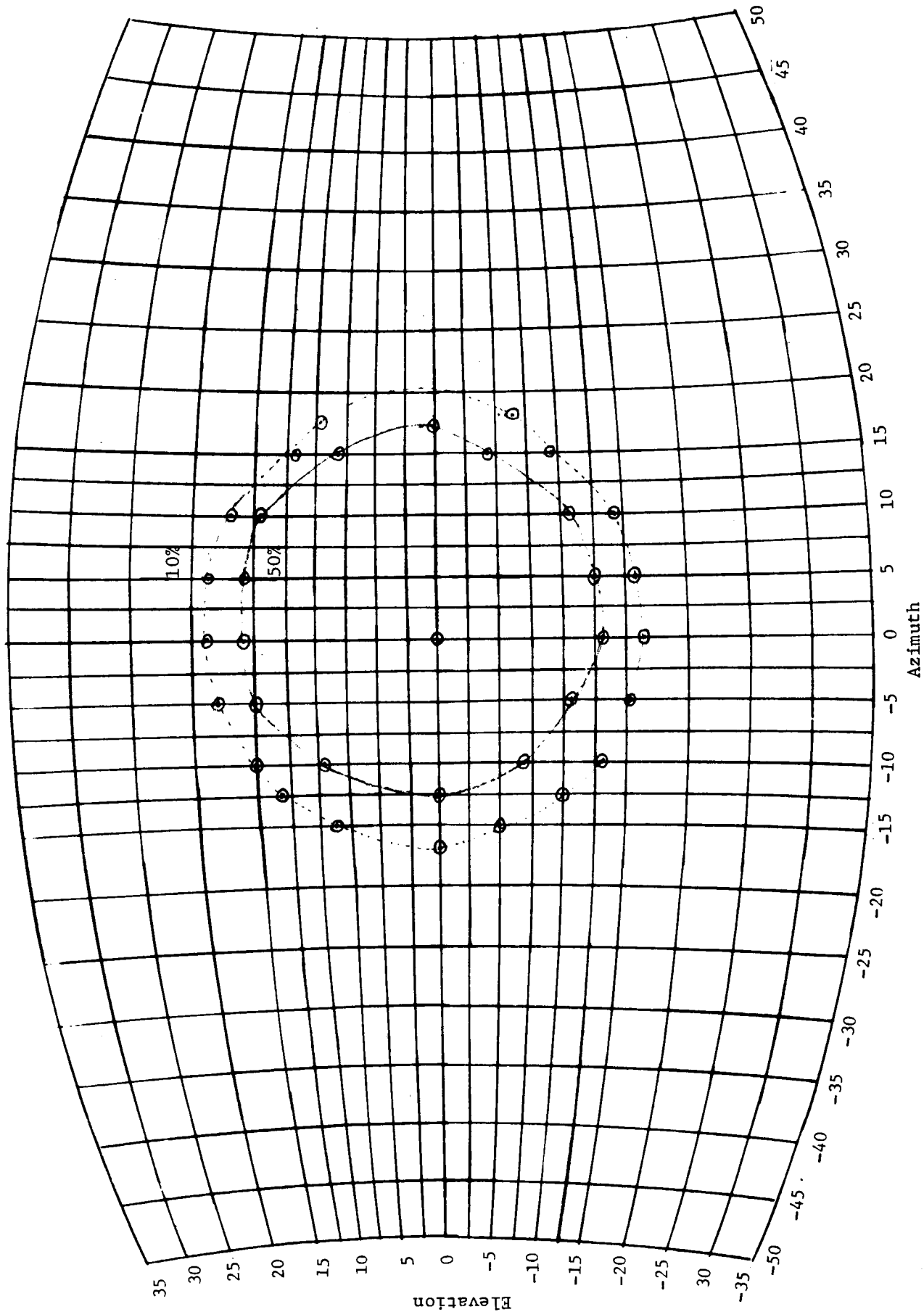


Figure 37. Field-of-View Contours, Channel B

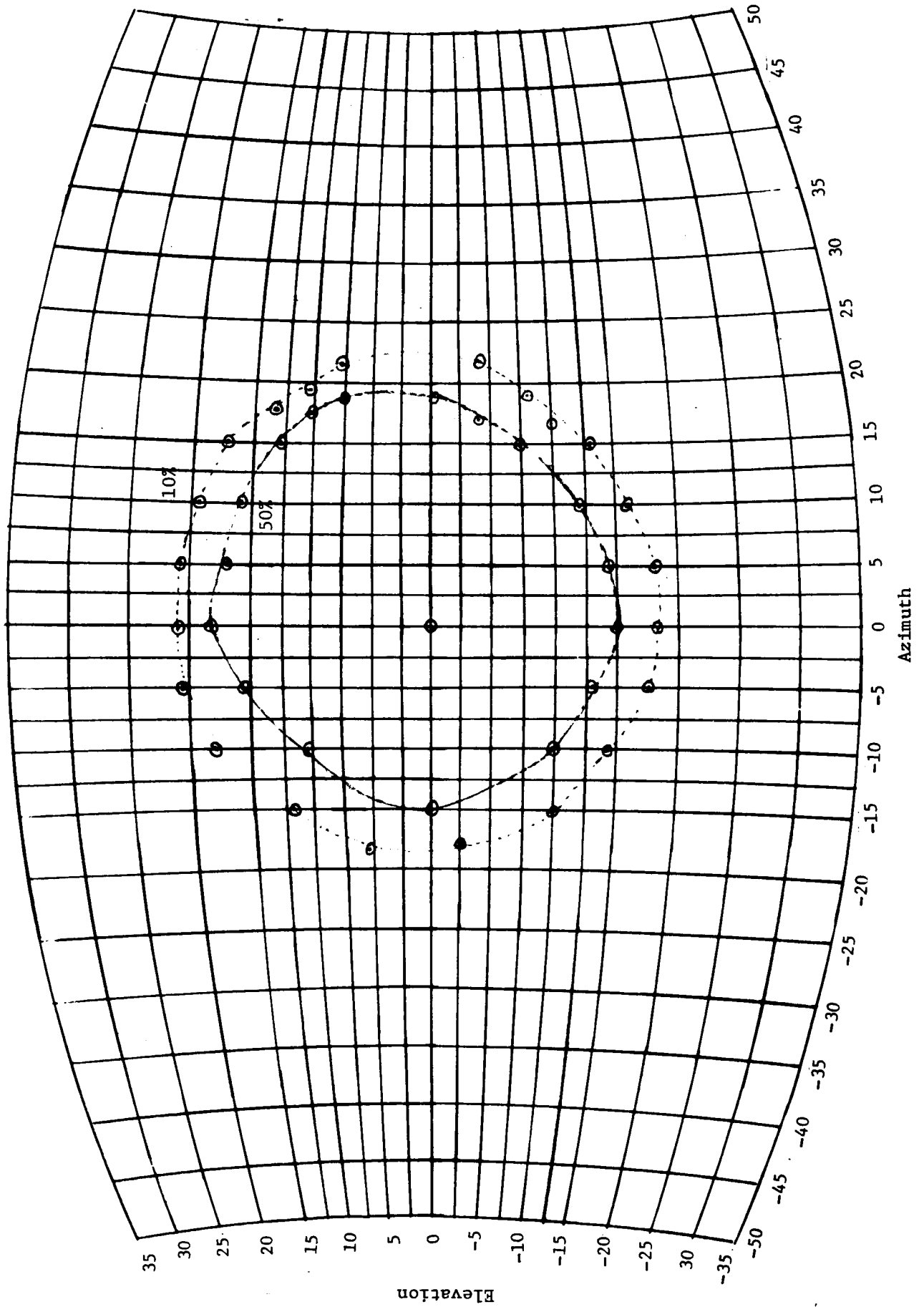


Figure 38. Field-of-View Contours. Channel C

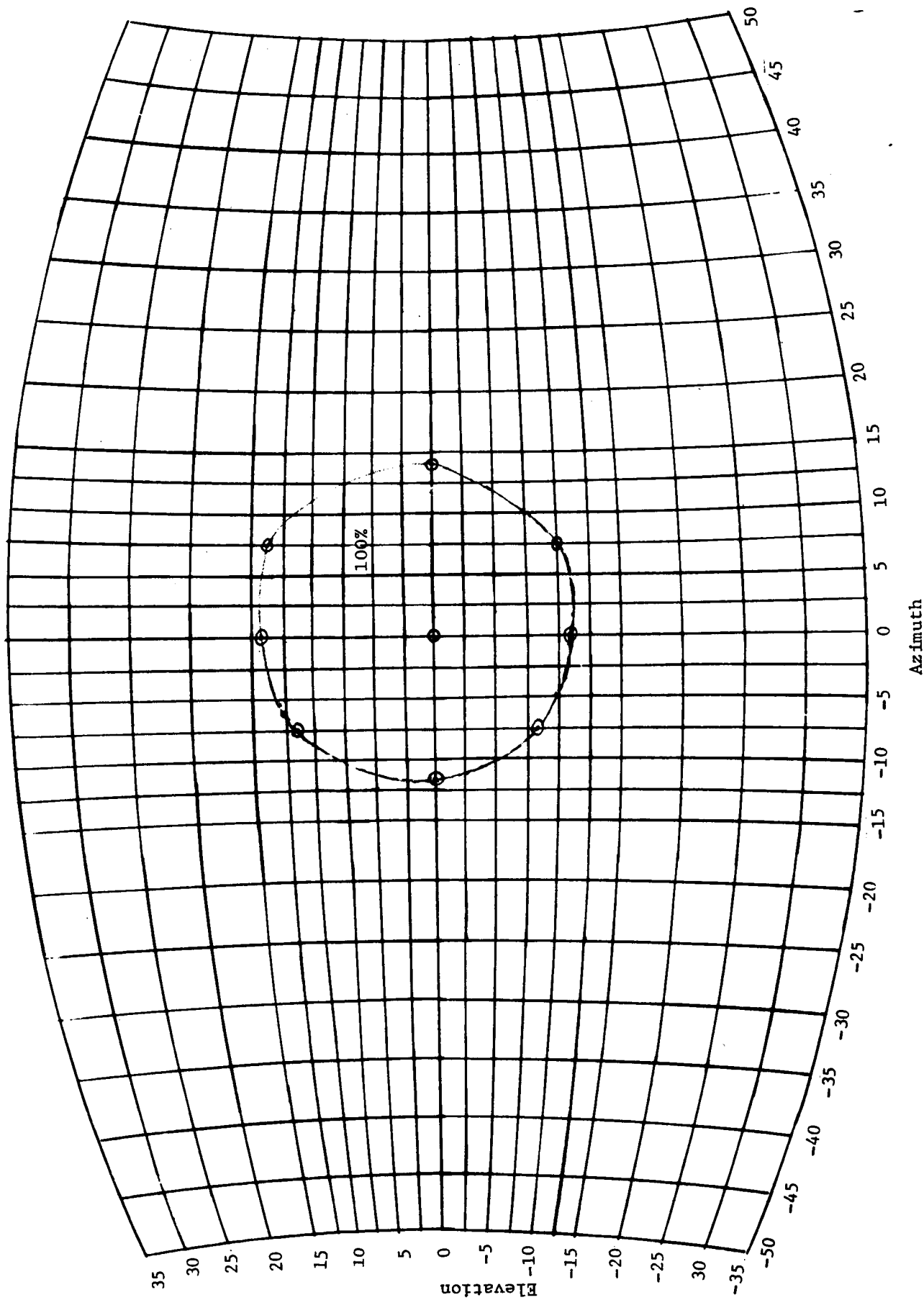


Figure 39. Field-of-View Contours, Photodiode

6.4 ABSOLUTE RESPONSIVITY

The responsivity results are shown in Table 13. The irradiance at the instrument aperture is determined as follows. The basic standard is an Eppley thermopile whose output is calibrated in microvolts/microwatt/cm², to an accuracy of $\pm 2\%$. Its sensitivity is not sufficient, however, to reliably measure the irradiance from the 2537 Å Hg line in the pen ray lamp (because of thermal fluctuations which disturb the D. C. measurement). To solve this problem, the total irradiance at the thermopile was measured with a lamp-detector distance of 6 cm and a stable signal. The thermopile, whose response time constant is quite long, was replaced by a thermocouple, chopper and synchronous amplifier. The 2537 Å interference filter was placed in the path, and the ratio of the lock-in output with and without the filter was observed. This ratio gives the fraction of the total irradiance (measured by the thermopile) in the 2537 Å line. The validity of $1/r^2$ intensity variation to 6 cm was checked independently. The thermocouple was removed from the path, allowing the beam to illuminate the MFA. The irradiance at the aperture was calculated from the $1/r^2$ attenuation (286 cm to the MFA). The result is

$$H(2537) = 1.73 \times 10^{-10} \text{ watts/cm}^2 .$$

The 3650 Å signal from the Osram lamp at 20 cm from the thermopile provided a D.C. measurement with 10% reproducibility. After calibration of the lamp, the thermopile was removed, allowing the beam to illuminate the MFA, 1500 cm away. The irradiance at the aperture is found to be

$$6.3 \times 10^{-9} \text{ watts/cm}^2 .$$

From these numbers, and the data of Table 13, the responsivities of the three data channels are:

- A: 1.85×10^{10} Volts/watt/cm² at 2537 Å
- B: $.345 \times 10^{10}$ Volts/watt/cm² at 2537 Å
- C: 4.8×10^{10} Volts/watt/cm² at 3650 Å

Table 13. Absolute Responsivity Data

Background A 16.4 millivolts

Background B 17.0 millivolts

No change with instrument blinded

Signal A 3.20 volts

Signal B .597 volts

Lamp-aperture distance 9 ft, 4-1/2 inches

Background C - 9.3 millivolts (instrument blinded)

Background C - 4.4 millivolts (ambient illumination)

Signal C .310 volts

Lamp-aperture distance 49 ft, 2-3/4 inches

The relative response data in Table 11 can now be converted to absolute values, as shown in Table 14 and Figures 40-42. To derive an N.E.I., it is necessary to know the noise level of the instrument. Anticipating the results of test 5.2.7, the peak-peak noise fluctuations are on the order of a few tenths of a millivolt, which is also the dark current of the photomultipliers. The N.E.I. values at the peak of the response curves are:

$$\begin{aligned} \text{A: } & 5 \times 10^{-4} / 2.2 \times 10^{10} = 2.3 \times 10^{-14} \text{ watts/cm}^2 \\ \text{B: } & 5 \times 10^{-4} / 1.3 \times 10^{10} = 3.8 \times 10^{-14} \text{ watts/cm}^2 \\ \text{C: } & 5 \times 10^{-4} / 5 \times 10^{10} = 1 \times 10^{-14} \text{ watts/cm}^2 , \end{aligned}$$

for the instrument functioning as a D.C. radiometer, 5×10^{-4} V peak-peak noise.

6.5 OPTICAL FLASH SIMULATION

The data from the optical flash simulation test are shown in Table 15 on 9 pages. The purpose of these tests was to verify operation of the unit with a voltage input to the electronics system derived from the photomultipliers. In view of the difficulty of obtaining the desired exponential waveform from an arbitrary light source, the relatively simple electronically controlled W pin-lite was used. In order to stimulate the ultraviolet channels A and B, the interference filters were removed. Thus, the flash testing is not an absolute measurement. The results may be compared with the electronically measured calibration curves, which accurately determine the input voltage required to produce a given output at the peak and area detectors. When the electronic calibration curves are used in conjunction with the responsivity curves of Figures 40-42, the absolute intensity and intensity-time functions of an unknown signal can be determined.

The reproducibility of measurement of a flash can be determined from the tabulated data. For all measurements within two decades of the upper limit of the peak and area amplifiers, the reproducibility is 1-2% or better. The measurements at three decades below maximum become somewhat more erratic, fluctuating by up to 10%. This is quite reasonable, since the photomultiplier dark current signals are in this range.

Table 14. Absolute Spectral Response,²
Units of 10¹⁰ Volts/watt/cm

λ , microns	A	B	C
.2200	.010		
.2300	.029	.003	
.2350	1.00		
.2400	1.63	.010	
.2450	2.2	.045	
.2500	2.15	.160	.0075
.2550	1.77		.0075
.2600	1.31	.845	.0085
.2650		1.13	.01
.2700	.546	1.24	.02
.2750			.075
.2800	.141	1.28	.215
.2850	.068	1.14	.5
.2900	.031	.95	.955
.3000	.006	.534	2.12
.3050		.36	2.62
.3100	.003	.233	2.95
.3150		.141	3.25
.3200		.082	3.47
.3250		.047	3.81
.3300		.027	4.11
.3350		.014	4.45
.3400		.008	4.76
.3500		.003	5
.3600			4.9
.3700			4.82
.3800			3.40
.3900			1.15
.4000			.13
.4100			.015

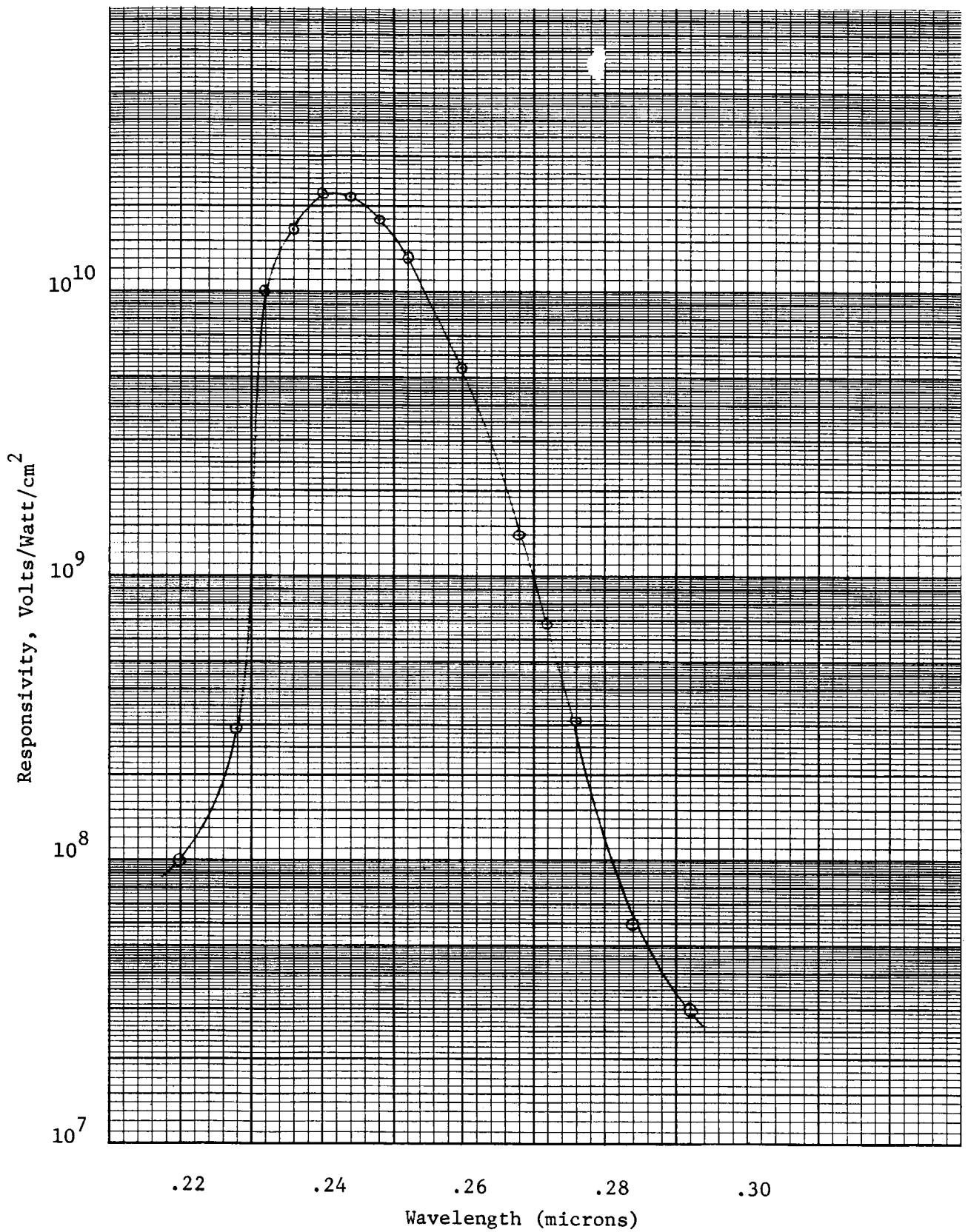


Figure 40. Absolute Spectral Responsivity, Channel A.

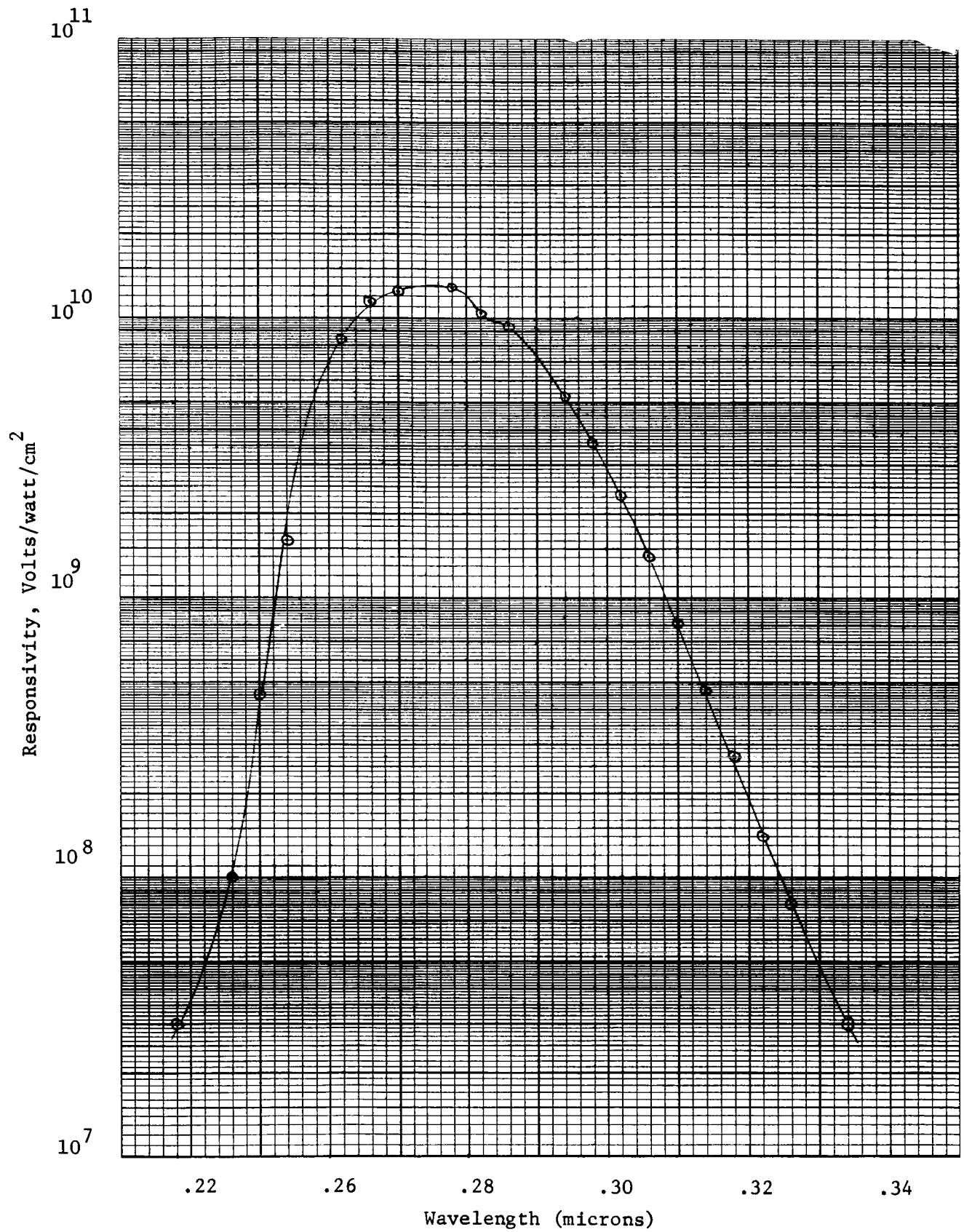


Figure 41. Absolute Spectral Responsivity, Channel B

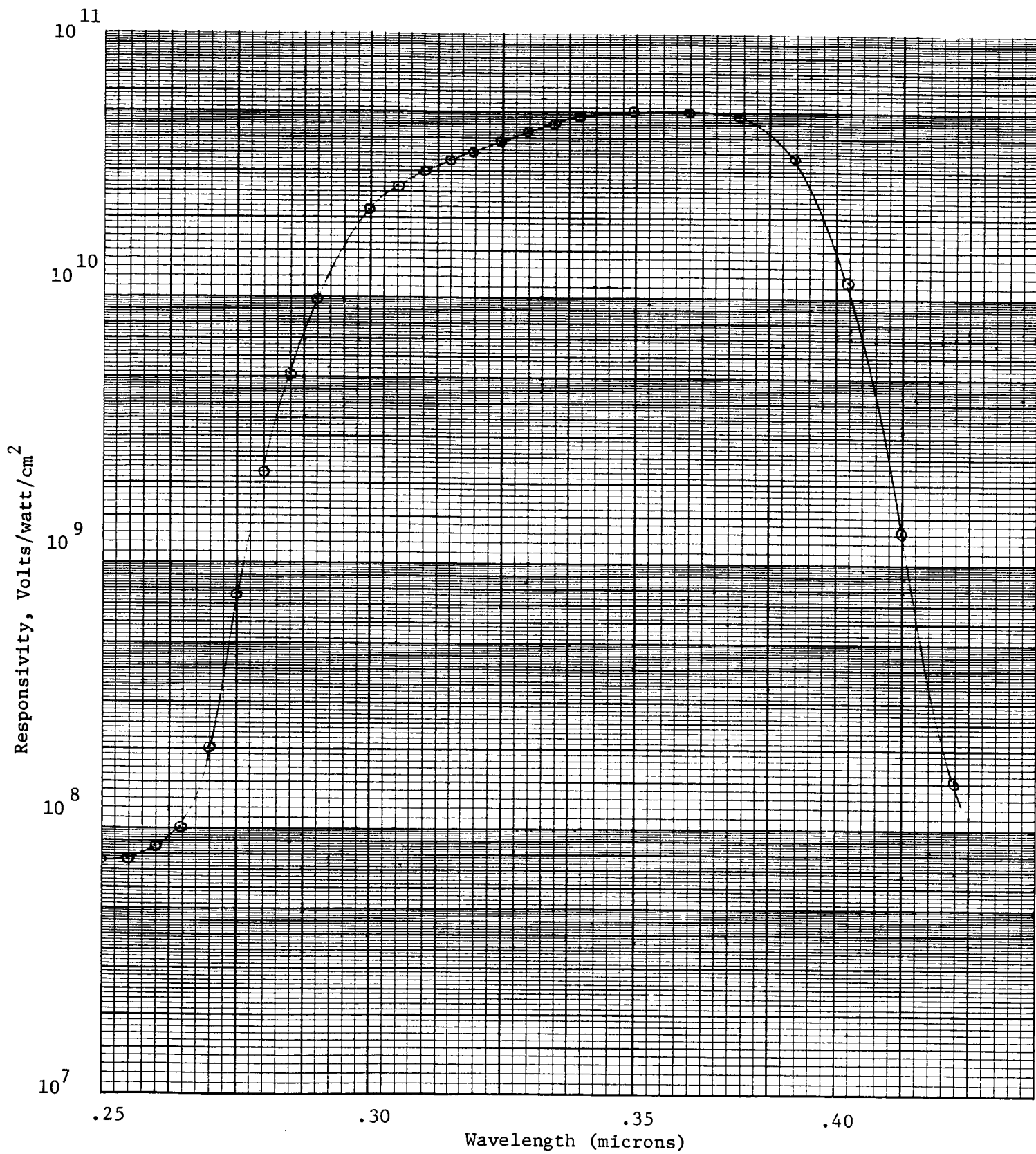


Figure 42. Absolute Spectral Responsivity, Channel C.

Table 15. Optical Flash Simulation Data

Data Channel	A
Background, millivolts	38
α	3.2
Neutral Density	--

Flash No.	Peak	Area	Reset, peak	Reset, Area
1	4.802	4.696	1.2	1.5
2	4.799	4.699	1.4	1.9
3	4.803	4.693	1.4	1.9

Data Channel	A
Background, millivolts	17.66
α	3.2
Neutral Density	1

Flash No.	Peak	Area	Reset, peak	Reset, Area
1	3.197	3.270	.560	.695
2	3.223	3.286	.597	.935
3	3.226	3.275	.432	.714

Table 15. Optical Flash Simulation Data

Data Channel	A
Background, millivolts	16.40
α	3.2
Neutral Density	2

Flash No.	Peak	Area	Reset, peak	Reset, Area
1	1.885	2.094	.408	.229
2	1.845	2.077	.766	.274
3	1.904	2.084	.433	.260

Data Channel	A
Background, millivolts	16.30
α	3.2
Neutral Density	3

Flash No.	Peak	Area	Reset, peak	Reset, Area
1	.653	.880	.432	.013
2	.553	.848	.130	.056
3	.512	.903	.077	.012
4	.587	.831	.131	-.057

Table 15. Optical Flash Simulation Data

Data Channel	B
Background, millivolts	19.0
α	3.2
Neutral Density	--

Flash No.	Peak	Area	Reset, peak	Reset, Area
1	4.895	4.945	.015	.307
2	4.894	4.942	.118	.225
3	4.891	4.937	-.042	.350

Data Channel	B
Background, millivolts	17.30
α	3.2
Neutral Density	1

Flash No.	Peak	Area	Reset, peak	Reset, Area
1	3.409	3.561	-.452	-.125
2	3.407	3.560	-.450	-.127
3	3.416	3.560	-.472	-.116

Table 15. Optical Flash Simulation Data

Data Channel	B
Background, millivolts	17.02
α	3.2
Neutral Density	2

Flash No.	Peak	Area	Reset, peak	Reset, Area
1	2.159	2.423	-.168	-.130
2	2.156	2.417	-.449	-.127
3	2.171	2.425	-.470	-.130

Data Channel	B
Background, millivolts	16.98
α	3.2
Neutral Density	3

Flash No.	Peak	Area	Reset, peak	Reset, Area
1	.485	.882	-.230	.056
2	.443	.872	-.465	-.125
3	.446	.829	-.063	-.120

Table 15. Optical Flash Simulation Data

Data Channel	C
Background, millivolts	-4.25
α	3.2
Neutral Density	--

Flash No.	Peak	Area	Reset, peak	Reset, Area
1	4.935	4.744	.849	.780
2	4.938	4.750	.856	.860
3	4.935	4.745	.816	.786

Data Channel	C
Background, millivolts	-9.35
α	3.2
Neutral Density	1

Flash No.	Peak	Area	Reset, peak	Reset, Area
1	3.530	3.395	.171	.099
2	3.544	3.410	.170	.170
3	3.538	3.409	.116	.120

Table 15. Optical Flash Simulation Data

Data Channel	C
Background, millivolts	-10.10
α	3.2
Neutral Density	2

Flash No.	Peak	Area	Reset, peak	Reset, Area
1	2.303	2.236	-.157	-.160
2	2.272	2.225	-.262	-.166
3	2.318	2.251	-.235	-.020

Data Channel	C
Background, millivolts	-10.10
α	3.2
Neutral Density	3

Flash No.	Peak	Area	Reset, peak	Reset, Area
1	.734	.761	-.218	-.160
2	.722	.856	-.272	-.160
3	.725	.770	-.420	-.162

Table 15. Optical Flash Simulation Data

Data Channel	C
Background, millivolts	11.1
α	3.2
Neutral Density	--

Flash No.	Peak	Area	Reset, peak	Reset, Area
1	4.960	4.768	1.142	1.378
2	4.957	4.768	1.189	1.269
3	4.960	4.769	1.236	1.212

Data Channel	C
Background, millivolts	10.7
α	3.2
Neutral Density	1

Flash No.	Peak	Area	Reset, peak	Reset, Area
1	3.506	3.379	1.185	1.046
2	3.511	3.368	1.185	1.051
3	3.503	3.371	1.192	1.029

Table 15. Optical Flash Simulation Data

Data Channel	C
Background, millivolts	10.8
α	3.2
Neutral Density	2

Flash No.	Peak	Area	Reset, peak	Reset, Area
1	2.267	2.170	1.193	1.072
2	2.279	2.312	1.234	1.168
3	2.273	2.293	1.084	1.006

Data Channel	C
Background, millivolts	102
α	3.2
Neutral Density	--

Flash No.	Peak	Area	Reset, peak	Reset, Area
1	4.939	4.758	1.866	1.784
2	4.934	4.756	1.749	1.424
3	4.936	4.749	1.723	1.784

Table 15. Optical Flash Simulation Data

Data Channel	C
Background, millivolts	102
α	3.2
Neutral Density	1

Flash No.	Peak	Area	Reset, peak	Reset, Area
1	3.523	3.418	1.649	1.667
2	3.506	3.422	1.610	1.598
3	3.520	3.423	1.667	1.403

Data Channel	C
Background, millivolts	102
α	3.2
Neutral Density	2

Flash No.	Peak	Area	Reset, peak	Reset, Area
1	2.322	2.379	1.756	1.783
2	2.324	2.263	1.711	1.537
3	2.334	2.318	1.743	1.575

Figures 43-48 show the flash data compared with the electronic calibration curves. The voltages required for correlation with peak and area readings are derived as follows. The peak voltages are read from the oscilloscope photographs of the unattenuated signals which appear at the video amplifier outputs. Several of the photographs are shown in Figure 49. This peak voltage is divided by 21 in order to obtain the equivalent signal on the electronic calibration curve (measured at gain = 21). The signal at ~ 5 V falls on the electronic line in all cases except Area B, for which all points deviate from the line. (This channel showed a large temperature dependence during calibration of the electronic unit, and the deviation of the optical results is probably due to this inherent instability of the channel.) For the other measurements, the fraction of the maximum signal required by the nominal value of the neutral density filter is plotted against the observed peak or area. Some of these points deviate from the curve, a fact which should be interpreted as uncertainties in the flasher and its peripheral equipment, e.g., deviations of N.D. values from nominal, variation of pinlite performance, changes in the electronic controller, etc. In fact, the observed peak and area readouts can be used to determine the instantaneous performance for a given flash.

In practice, this is the manner in which to use the calibration data: an observed output is correlated with the voltage which produced it, correcting for the gain state of the channel. This voltage is divided by the responsivity, Figures 40-42, to derive the irradiance at the aperture. The same procedure can be applied to the area detector output, resulting in an absolute quantity in terms of watts \cdot sec/cm².

From the plots of Figures 43, 45, and 47, it appears that optical signals of $\sim 3 \times 10^{-4}$ V peak intensity are detectable with reasonable precision ($\pm 10\%$).

This corresponds to

$$\begin{aligned}
 &1.4 \times 10^{-14} \text{ watts/cm}^2 \\
 &2.9 \times 10^{-14} \text{ watts/cm}^2 \\
 &\text{and } .6 \times 10^{-14} \text{ watts/cm}^2
 \end{aligned}$$

irradiance at the apertures of channels A, B, and C, respectively.

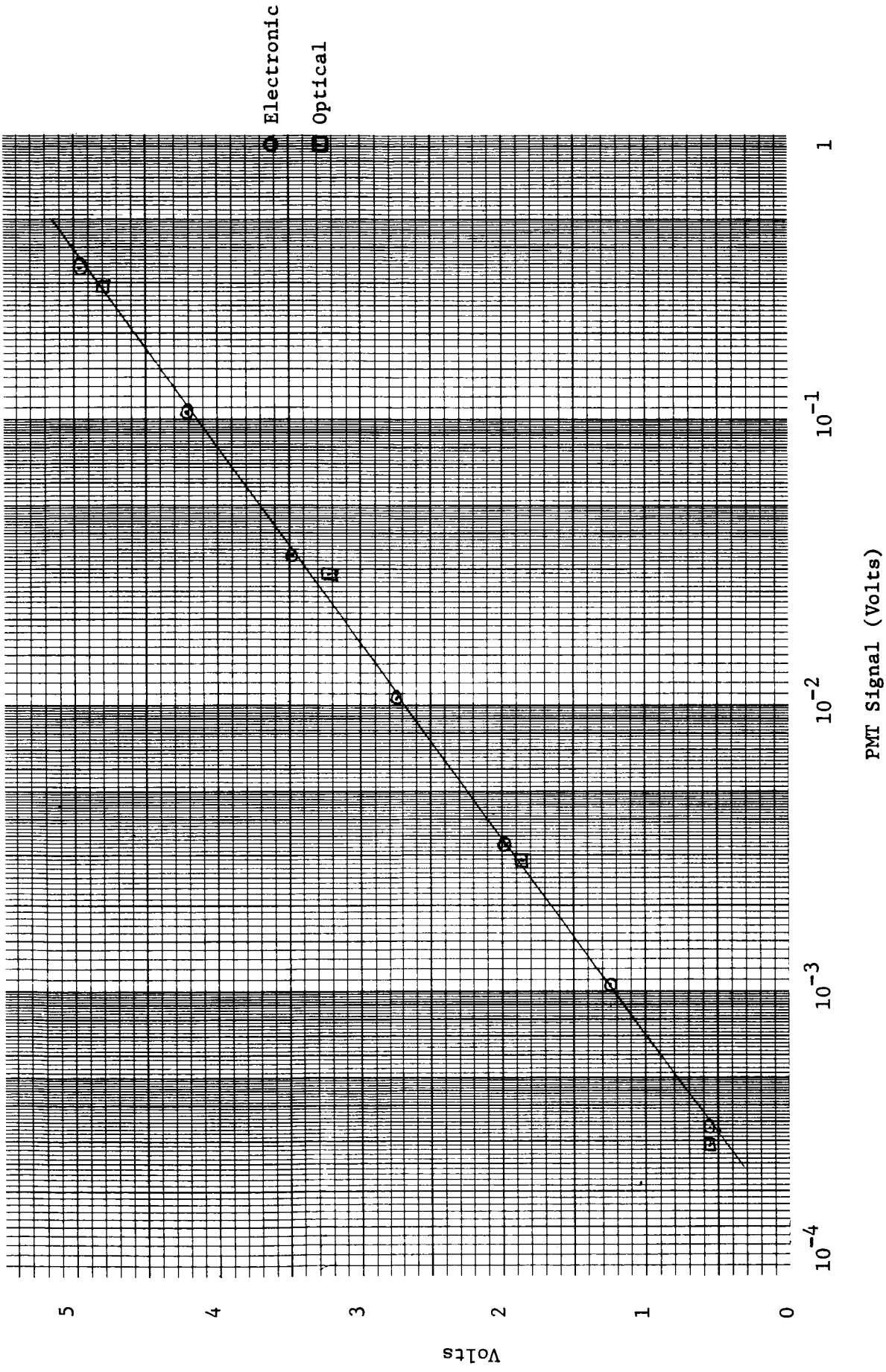


Figure 43. Comparison of Optical Flash Data and Electronic Calibration.
 Peak A, $\alpha \approx 3.2$ for Gain 21.

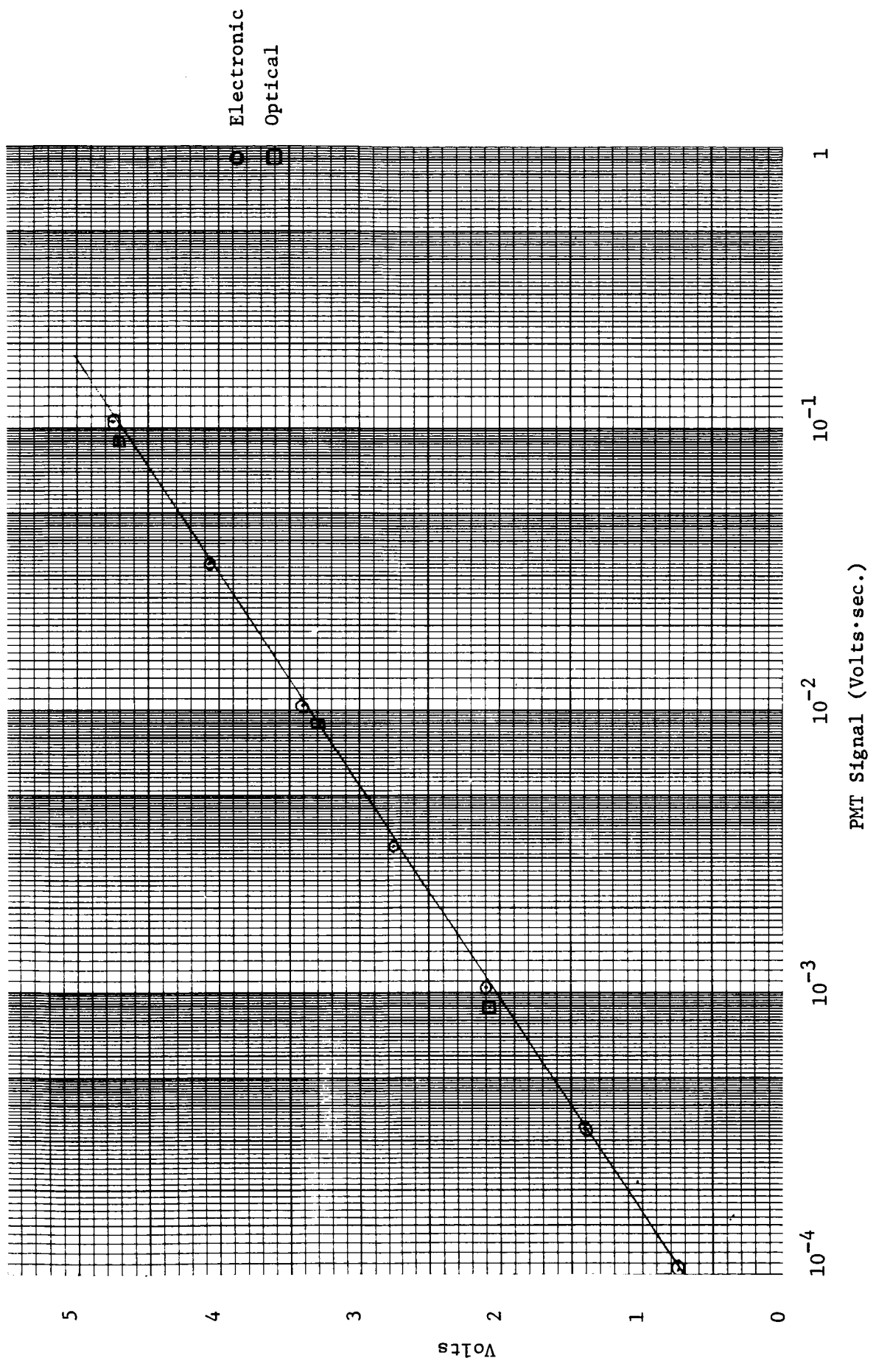


Figure 44. Comparison of Optical Flash Data and Electronic Calibration.

Area A, $\alpha = 3.2$ for Gain 21.

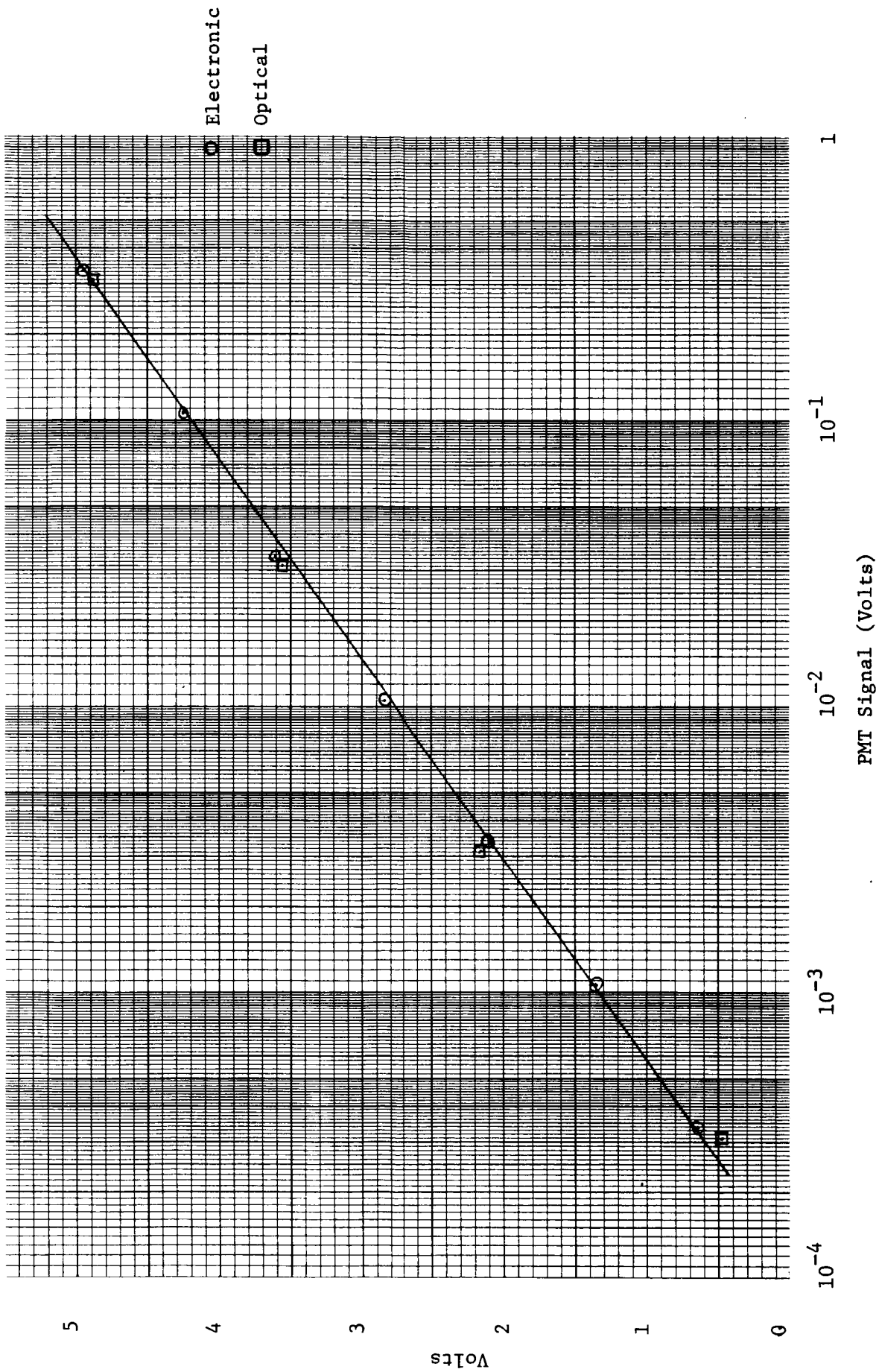


Figure 45. Comparison of Optical Flash Data and Electronic Calibration.

Peak B, $\alpha = 3.2$ for Gain 21.

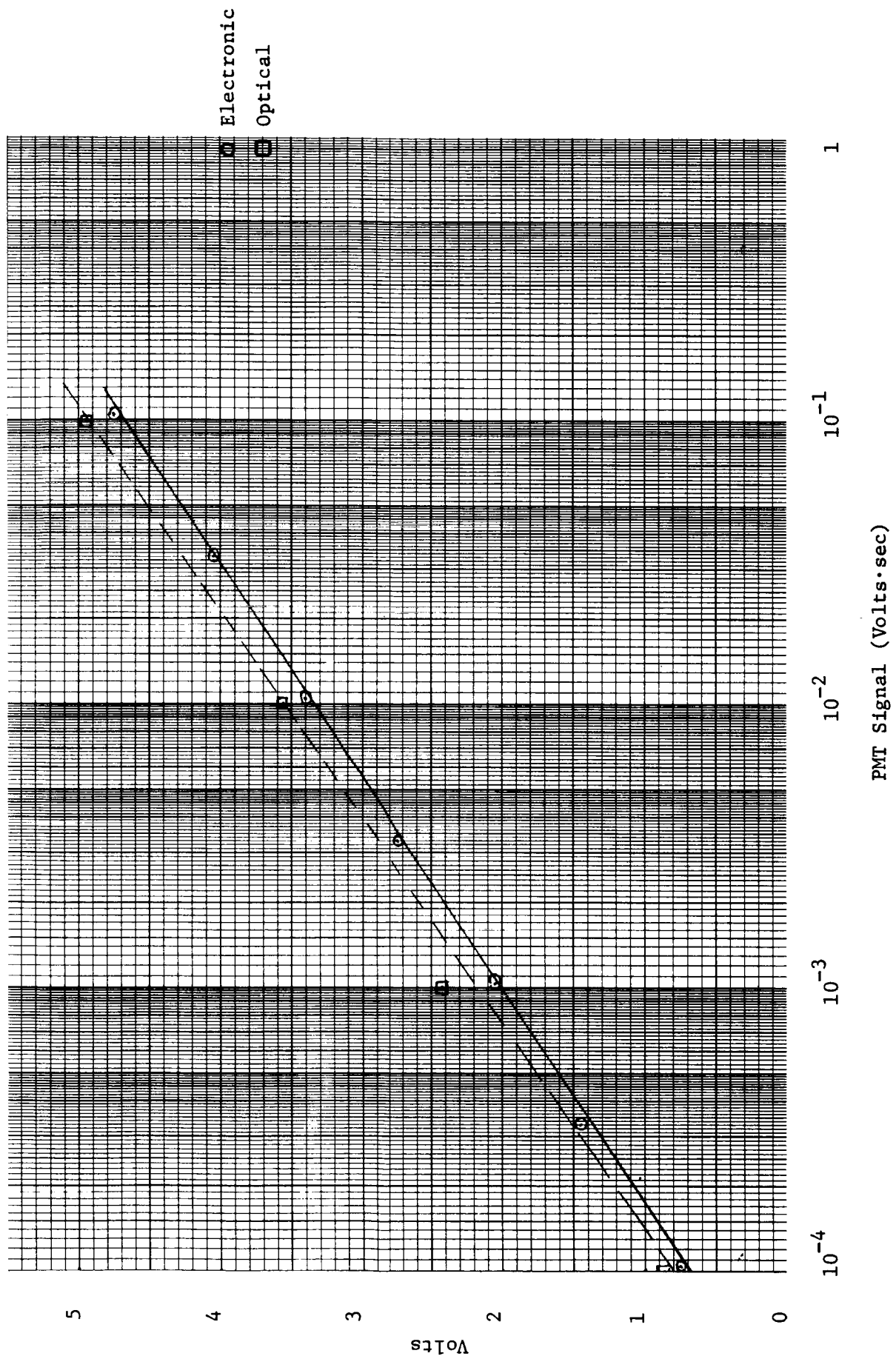


Figure 46. Comparison of Optical Flash Data and Electronic Calibration
 Area B, $\alpha = 3.2$ for Gain 21.

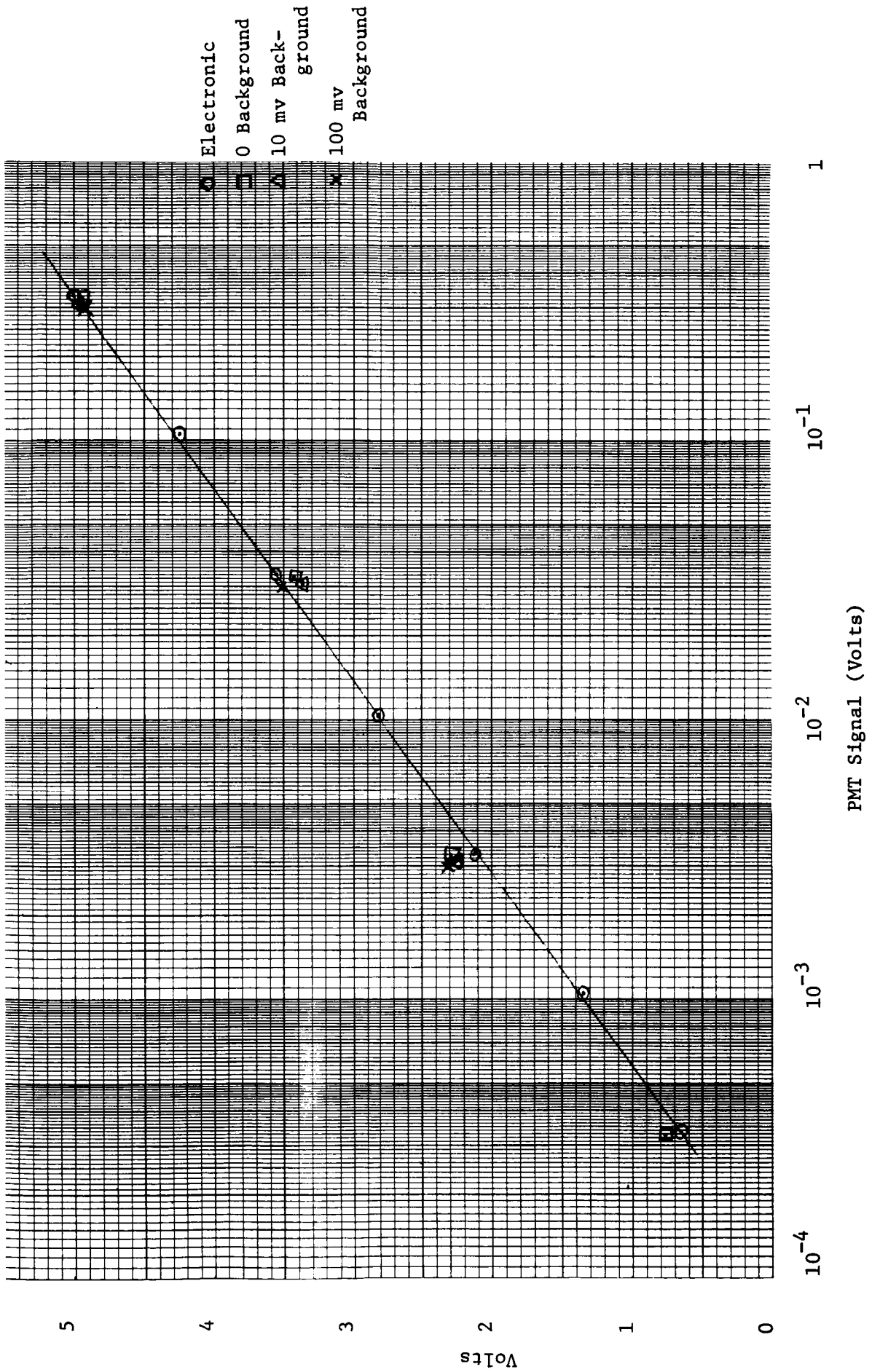


Figure 47. Comparison of Optical Flash Data and Electronic Calibration.
Peak C, $\alpha = 3.2$ for Gain 21.

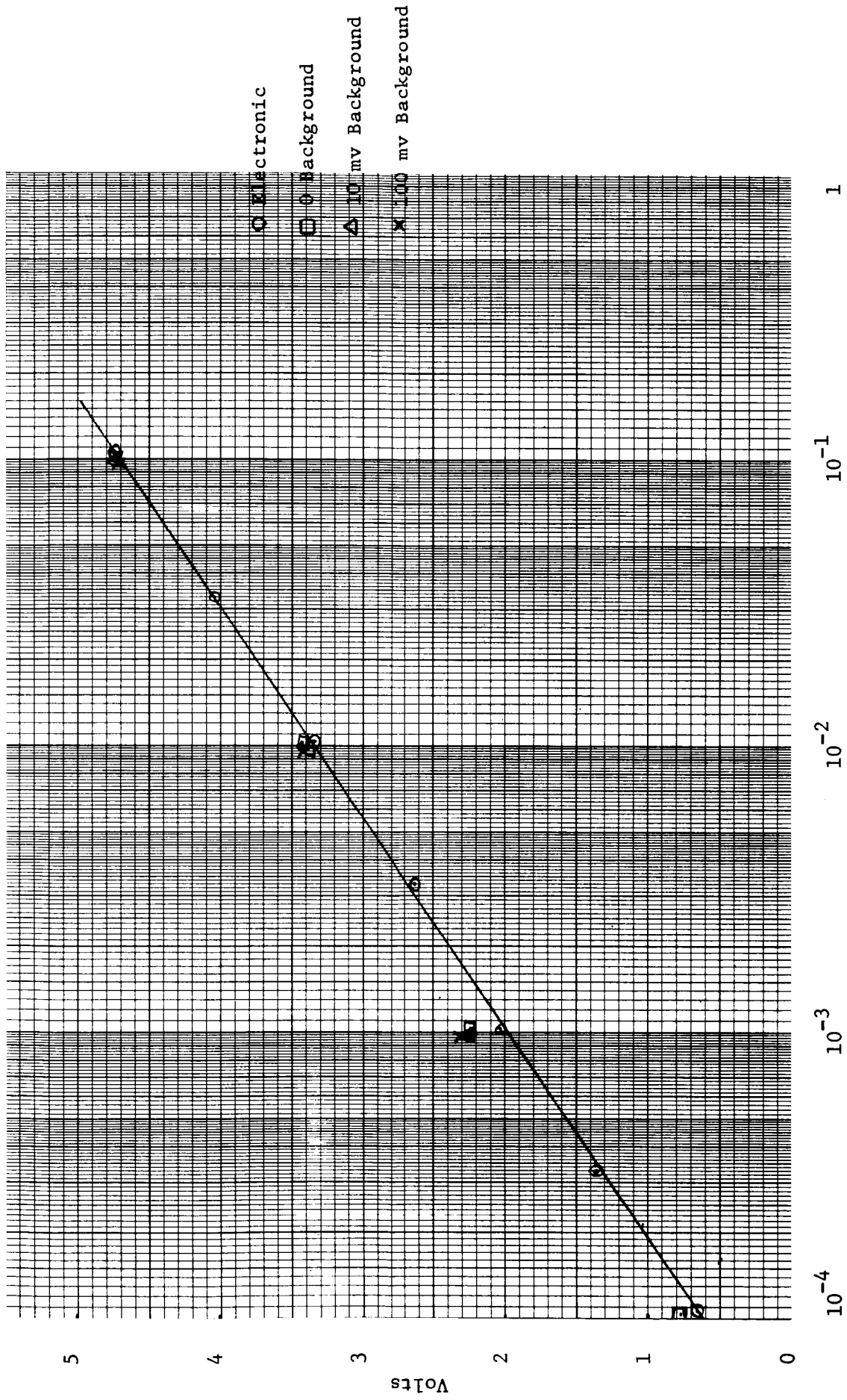
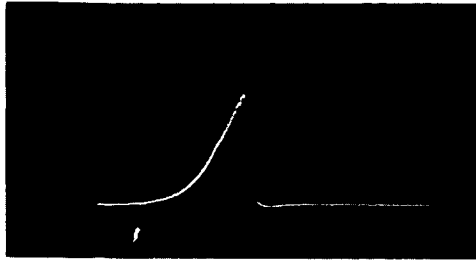
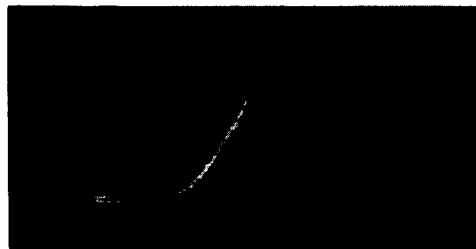


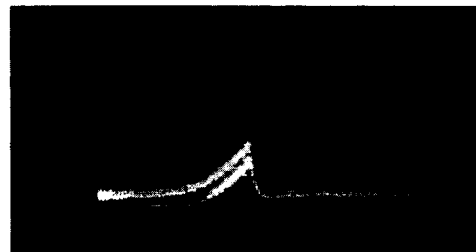
Figure 48. Comparison of Optical Flash Data and Electronic Calibration.
 Area C, $\alpha = 3.2$ for Gain 21.



a. Channel A, .5 cm/sec, 2 V/cm
Zero Attenuation



b. Channel A, .5 cm/sec, .2 V/cm
Neutral Density = 1



c. Channel A, .5 cm/sec, .050 V/cm
Neutral Density = 2

Figure 49. Oscilloscope Traces for Some Flash Simulation Tests

The upper limit is 3 decades higher, plus a factor of $21/6 = 3.3$ from gain switching:

A:	4.6×10^{-11}	watts/cm ²
B:	9.6×10^{-11}	watts/cm ²
C:	2×10^{-11}	watts/cm ²

This is for the condition of dark current limited operation. As the background current is increased, the noise voltage of the peak and area detectors increases to ~ 2 V at 0.10 V background (see data in Table 15). This background is ~ 300 times the minimum detectable signal, which should cause a deterioration of ~ 17 in signal/noise. At two volts, the calibration curves do show a loss of about a decade in sensitivity.

6.6 SUN SENSOR TEST RESULTS

The results of illuminating the instrument, with a sun gun, to the level where the photodiode turns off the photomultiplier high voltage supply are in Table 16. It can be seen that the instrument output becomes somewhat erratic and unreliable at the minimum detectable signal level, while performance is maintained at high signal levels. It is normal for a photomultiplier dark current to increase following intense illumination and to require a period of darkness to fully recover. This is the behaviour exhibited by channel C. As expected, the signal levels at turn-off on channels A and B are well below channel C outputs showing that these tubes are well protected against sunlight.

6.7 NOISE TEST RESULTS

The observed peak-peak noise levels observed at the video outputs are:

A:	2	millivolts
B:	1.5	millivolts
C:	2	millivolts

At a gain of 20, these values correspond to 0.1 or less millivolts at the input to the amplifier. This is in agreement with optical flash results, where the minimum detectable signals were shown to be essentially at detector dark current levels, or ~ 0.3 millivolts at the amplifier input. The electronic system, therefore, is well matched to the characteristics of the optical detectors.

Table 16. Sun Sensor Test Data

Data Channel	C
Background, millivolts	-10.2
α	3.2
Neutral Density	3

Flash No.	Peak	Area	Reset, peak	Reset, Area
1	.549	.667	-.360	-.150
2	.580	.683	-.380	-.150
3	.530	.667	-.380	-.150

Data Channel	C
Background, millivolts	-5
α	3.2
Neutral Density	3

2 minutes to recover

Flash No.	Peak	Area	Reset, peak	Reset, Area
1	.628	.570	.104	-.147
2	.652	.625	-.046	-.145
3	.594	.556	-.150	-.130
4	.554	.590	-.500	-.150

Background at Turn-off: C: 5.5
 B: .044
 C: .037

Table 16. Sun Sensor Test Data

Data Channel	C
Background, millivolts	-6
α	3.2
Neutral Density	3

2 minutes to recover

Flash No.	Peak	Area	Reset, peak	Reset, Area
1	.286	.367	-.500	-.148
2	.407	.478		
3	.428	.422	-.500	
4	.421	.445		-.500
5	.369	.525	-.500	

Data Channel	C
Background, millivolts	-6
α	3.2
Neutral Density	3

2 minutes to recover

Flash No.	Peak	Area	Reset, peak	Reset, Area
1	.155	.190	-.529	-.129
2	.277	.342	-.238	+0.019
3	.384	.415	.450	-.139
4	.373	.378	-.360	-.150

Table 16. Sun Sensor Test Data

Data Channel	C
Background, millivolts	-7
α	3.2
Neutral Density	--

2 minutes to recover

Flash No.	Peak	Area	Reset, peak	Reset, Area
1	4.735	4.458	--	.875
2	4.729	4.459	.325	--
3	4.733	4.450	--	--

Data Channel	
Background, millivolts	
α	
Neutral Density	

Flash No.	Peak	Area	Reset, peak	Reset, Area
1				
2				
3				

7. RECOMMENDATIONS

The present program has resulted in the definition of a meaningful measurements program on optical meteors from a space platform and in the construction and testing of a flight prototype model Meteor Flash Analyzer apparatus for carrying out the required experiments. The next logical step would be a flight experiment. It is recommended that the following programs and missions applying the developed apparatus and concept be considered in the future:

1. Earth orbiting experiment to carry out the specific measurements tasks described in Section 2.
2. Mars orbiting experiment to determine massive meteor abundance at Mars.
3. Venus orbiting mission.

Continuation of data from missions 1, 2 and 3 should result in an advanced experimental understanding of the massive meteor abundance in the solar system (see discussion in Section 3.1).

APPENDIX A

MEASUREMENT OF RADIANT ENERGY DISTRIBUTION AND ABSOLUTE RADIATIVE EFFICIENCIES IN SIMULATED METEORS

by

J. C. Slattery and E. Tagliaferri

A-1. INTRODUCTION

This experiment was undertaken to investigate the spectral distribution of radiant energy and absolute radiant efficiencies from simulated meteors as function of target gas composition. Besides air, other target gases were chosen to simulate the composition of three different martian atmosphere models now most commonly used.^{A-1}

The basic techniques used are similar to those used in earlier experiments on meteor ionizing and luminous efficiencies.^{A-2,A-3} The high velocity particles used in these experiments were obtained from the TRW Systems' electrostatic particle accelerator.^{A-4} Particle velocities ranged from about 20 km/sec to 35 km/sec. The particles were injected into a low pressure gas target, where they were heated by the target gas to the vaporization temperature. Particles with initial velocities in excess of about 20 km/sec are completely vaporized in the chamber. The measurement of the spectrum was made using photomultiplier tubes (PMT) in conjunction with narrow pass band transmission filters. The relative radiant energy in each narrow wavelength band was measured relative to the total light emitted in the visible region as determined by an unfiltered monitor tube viewing a selected portion of the total trail. A different experimental arrangement which permitted viewing of total trail length was used for absolute radiant efficiencies.

A-2. APPARATUS

A-2.1 PARTICLE ACCELERATOR

The particle accelerator consists of a modified 2-million-volt Van de Graaff accelerator with a particle charging and injection mechanism. Solid particles (in this case, iron particles) of nominally one-micron diameter are inductively charged to a high positive potential (with surface electric fields in excess of 10^9 volts/meter), and are injected into the accelerating field of the Van de Graaff. The ratio of the charge deposited on a particle to the particle mass, q/m is given by

$$(q/m) \propto \frac{1}{r} \quad (\text{A-1})$$

where r is the particle radius. Hence, smaller particles have higher charge-to-mass ratios and are accelerated to higher velocities than larger ones. Typically, a one-micron diameter particle attains a final velocity of 6 to 8 km/sec, while the range of particle velocities obtainable from the accelerator varies from 0.5 km/sec (for particles of about 4-micron diameter) up to 45 or 50 km/sec (for particles of ~ 0.1 microm diameter).

The particle parameters, such as mass, radius, charge, etc., are measured electronically. In its simplest form, a particle detector is simply a hollow metal cylinder through which the particle passes. When the particle is inside the cylinder, it induces a voltage signal on the capacitance of the cylinder, the magnitude of which is proportional to the charge on the particle. The duration of the signal gives the time required to pass through the cylinder and, hence, is a measure of the

particle velocity. Given the charge on the particle q , its velocity v , and the accelerating voltage V , we have

$$qV = \frac{1}{2} mv^2 \quad (\text{A-2})$$

from which the particle mass and, therefore, the radius can be determined. All measurements are passive and in no way affect or interfere with the particle. All of the electronic particle detectors used in these experiments are variations or combinations of this simplest type of detector.

Ordinarily, it is not possible to predict in advance the exact mass and velocity of a particle from the accelerator. Since it is usually desirable to have particles in a fixed velocity range for a given set of experimental conditions, a particle velocity selection system is used. It consists of two of the basic detectors, as described above, placed a known distance apart. The experimenter dials the desired range of particle velocities into a logic circuit. The two pulses from the detectors are then fed to the logic circuit and if the particle velocity lies within the preselected range, a signal appears at the output. In practice, this signal is used to trigger one or more oscilloscope traces upon which are displayed the appropriate data to be recorded. A photograph of the traces is taken for a permanent record.

A-2.2 DIFFERENTIAL PUMPING SYSTEM AND TARGET CHAMBER FOR
RELATIVE RADIANT ENERGY DISTRIBUTION MEASUREMENTS

A differential pumping chamber is used to isolate the gas target chamber from the high vacuum of the accelerator. For this experiment, a one-stage differential system was used. Two channels are used, each 0.100" in diameter. A single two-inch diffusion pump placed in the intermediate chamber of the system will allow gas target pressures of up to several tenths Torr in the target chamber, while leaving the pressure in the accelerator tube undisturbed at about 10^{-5} Torr. During this experiment, the gas pressures ranged from 200 to 250 μ in the target chamber. The pressure was adjusted using a calibrated variable leak, and was monitored with a Pirani gauge.

Figure A-1 is a schematic diagram of the experimental setup. The target chamber has two PMT's viewing the same 2 cm long segment of the luminous trail of the ablating particle. One of these was an RCA 6199, which was used as a monitor throughout the experiment and viewed the trail through a glass window. The other was an EMI 6255 tube with extended response in the uv range. The spectral sensitivity of this tube is shown in Figure A-2. A quartz window is used to maintain vacuum, with a cut-off filter and an interference filter placed between the quartz window and the PMT. The current at the anode of both PMT's was integrated using a 1000 pfd capacitor in parallel with a 100K ohm resistor. The integrated signal was fed to a high input impedance source follower, through an emitter follower and then directly to the recording oscilloscope. The lifetime of the visible trail is much shorter than the decay time constant of the integrating circuit so that the amplitude of the output signal gives the

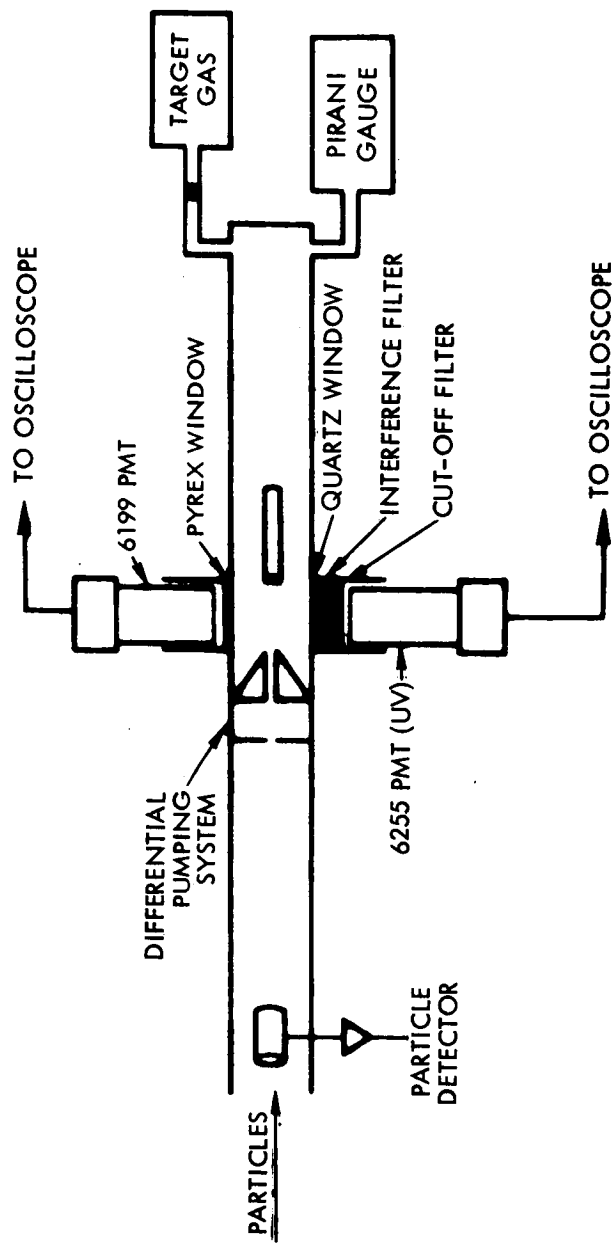


FIGURE A-1. BLOCK DIAGRAM OF EXPERIMENTAL ARRANGEMENT

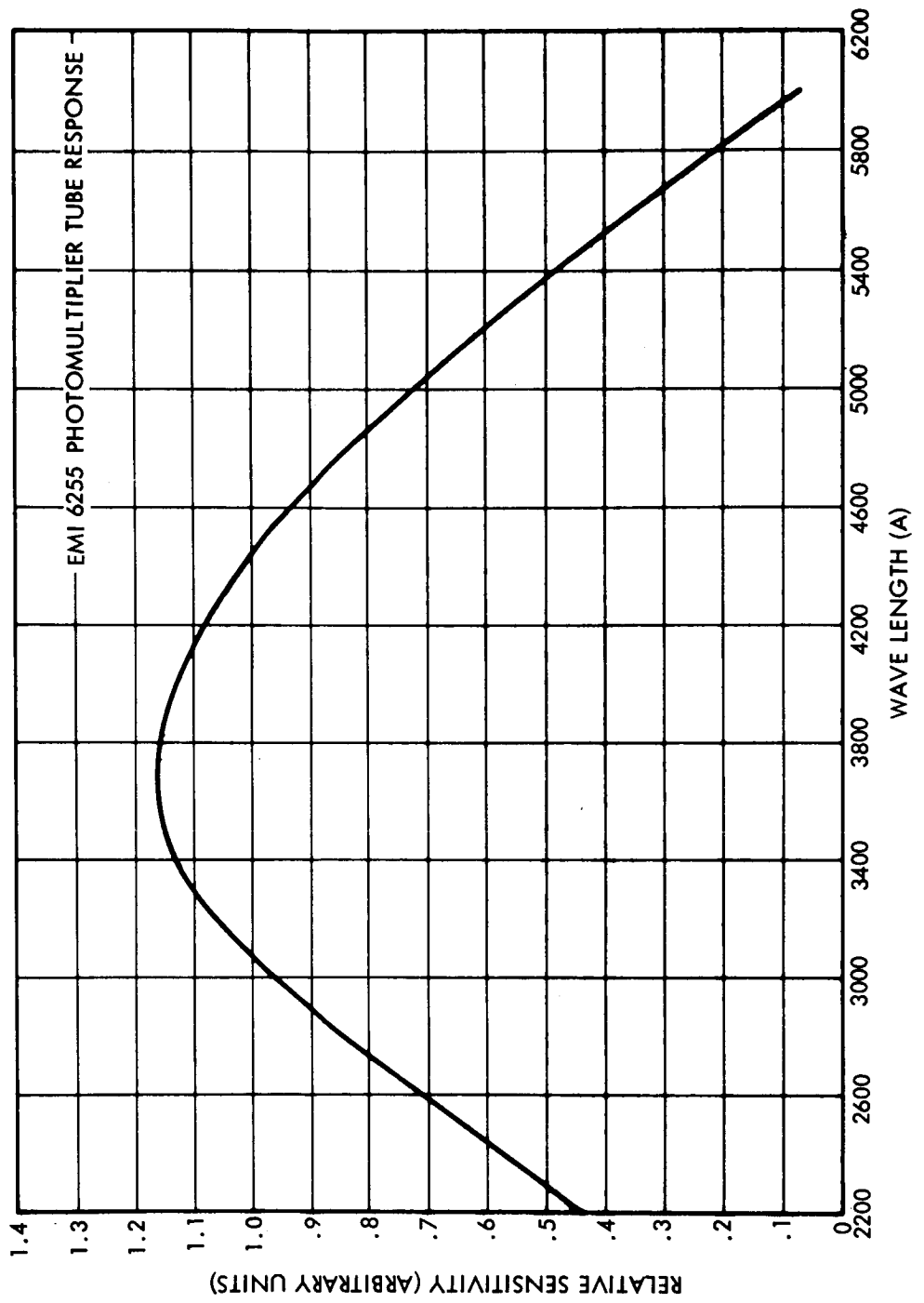


FIGURE A-2. RELATIVE SPECTRAL RESPONSE OF EMI 6255 uv PHOTOMULTIPLIER TUBE.

integral of the PMT current over the lifetime of the light signal. The signals from the two PMT's were displayed simultaneously on a Tektronix 555 dual beam oscilloscope. The oscilloscope was triggered by the signal from the velocity detector system, and knowing the distance from the detector system to the gas target, the particle velocity was determined by measuring the time from the beginning of the trace sweep to the beginning of the light signal from the PMT. Photographs were made of the signals for a permanent record.

Two cut-off filters were used. A uv cut-off filter, Corning Glass CS 3-74, was used when making measurements in the visible region of the spectrum, and a visible cut-off filter, Corning Glass CS 7-54, was used when making measurements in the uv region. Narrow pass band interference filters were used to further limit the region of the spectrum to be measured.

Clearly then, if the sensitivity of the PMT as a function of wavelength λ is given by $S(\lambda)$, the transmission of the cut-off filter by $C(\lambda)$ and the transmission of the narrow pass band filter by $g(\lambda)$, the current at the anode of the PMT is given by

$$Q = K \int_{\lambda} I(\lambda) S(\lambda) C(\lambda) g(\lambda) d\lambda \quad , \quad (A-3)$$

where $I(\lambda)$ is the intensity distribution of the radiation from the trail, and k is a constant to take into account solid angle factors, gain of the emitter follower, etc.

Unfortunately, this integral cannot be evaluated without knowledge of the function $I(\lambda)$, which is the object of the experiment. Therefore it was assumed that $I(\lambda)$ was a slowly varying function over the region covered by the interference filter, and further, could be represented by some average value \bar{I} . Then, if the region covered by the interference filter is from λ_1 to λ_2 ,

$$Q = K\bar{I} \int_{\lambda_1}^{\lambda_2} S(\lambda) C(\lambda) g(\lambda) d\lambda \quad . \quad (A-4)$$

The integral was carried out numerically for all of the interference filter-cut-off filter combinations.

Four different target gases were used. These were air, a CO_2 (75%) - A (25%) mixture, a CO_2 (44%) - N_2 (56%) mixture and pure CO_2 . Data were taken for all interference filters with all gases. Complete sets of data were taken for particles with velocities ranging from 20-28 km/sec and for particles with velocities from 28-34 km/sec. Because of variations in size and velocity, the total light produced was not the same from particle to particle, and therefore each measurement of Q by the uv tube was referenced to the corresponding quantity measured by the unfiltered monitor tube.

A-3. RESULTS

The two sets of interference filters used were both made by Optics Technology, Inc. The set of visible filters had pass bands centered at 5630 Å, 5300 Å, 4980 Å, 4650 Å, 4330 Å and 4100 Å. The ultraviolet set had pass bands centered at 3750 Å, 3600 Å, 3400 Å, 3180 Å, 2960 Å, 2780 Å, 2590 Å and 2420 Å, after folding in the PMT and cut-off filter response curves. With each interference filter in place (in front of the appropriate cut-off filter), two sets of 8 to 10 particles each were run, one at high velocities and one at low velocities.

The two oscilloscope sweeps for each particle were photographed and relevant distances measured on a Telereader (photographic projector) later. About 250 particles were photographed for each of the four target gases, so that in all over 1000 particles were recorded and analyzed.

The normalization procedure used was to take the signal from the uv tube and normalize it to the signal from the monitor tube (both signals measured in volts) for each particle. The average value of the ratio was then calculated for each gas-filter combination for each velocity range. The results are shown in Figures A-3, A-4, A-5, and A-6. Shown are the relative values of the quantity \bar{I} as a function of wavelength. The length of each vertical error bar is two standard deviations for that particular set of data. The length of each horizontal error bar is the full width at half maximum of that particular combination of filter-cut-off filter-PMT pass band. The units on the vertical scale are arbitrary. The data are listed in Table A-1. In principle it should be possible to determine the absolute intensity in each pass band, but this has not been done. The average velocity of the "high velocity" particles was 30 km/sec and the average velocity of the "low velocity" particles was 25 km/sec.

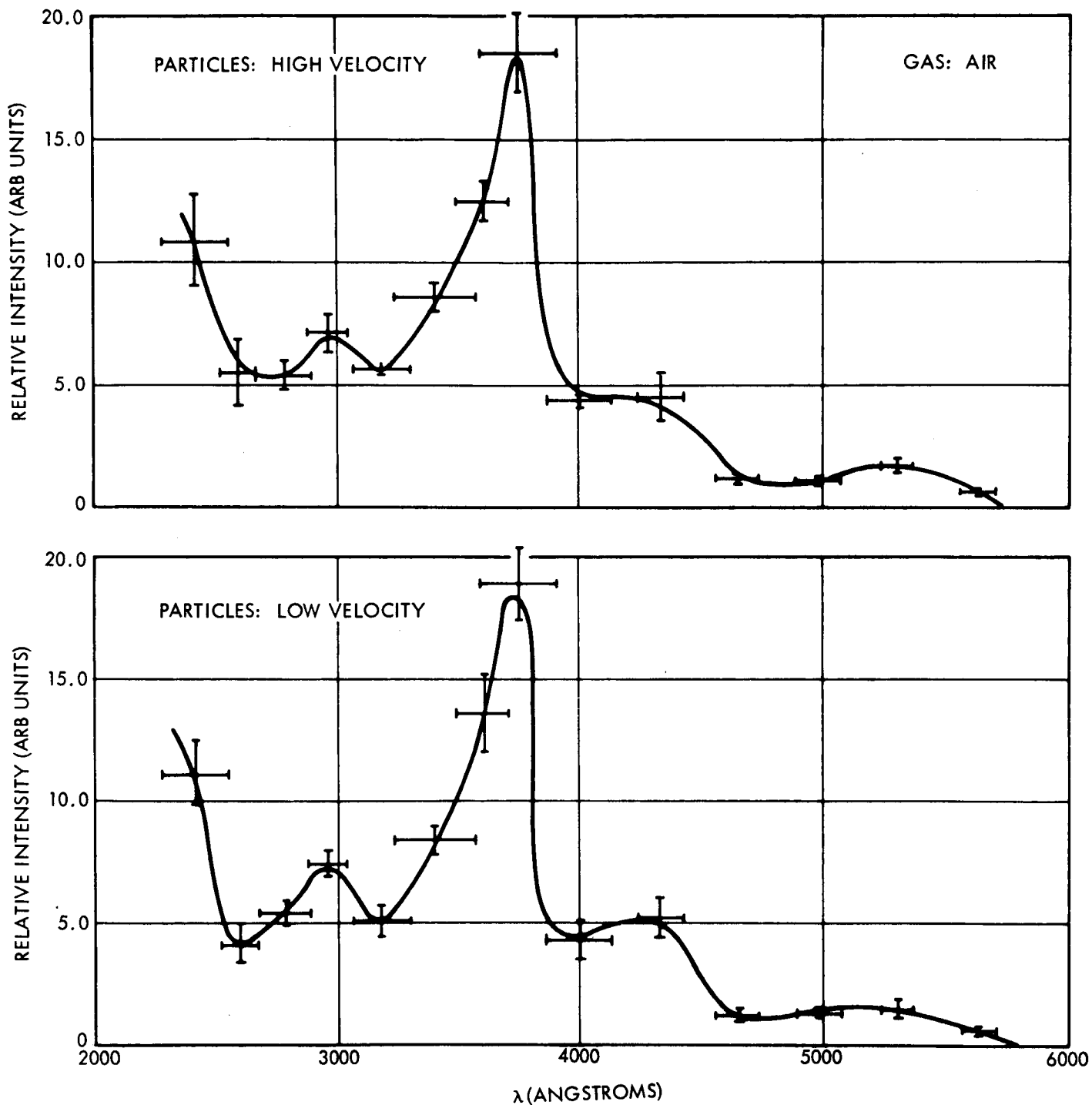


Figure A-3 Relative Intensity of Light Emission from Iron Particles in Air. High velocity particles are 30 km/sec average and low velocity particles are 25 km/sec average. Vertical error bars are two standard deviations and horizontal error bars are full-width-at-half-maximum of the filter-phototube combination.

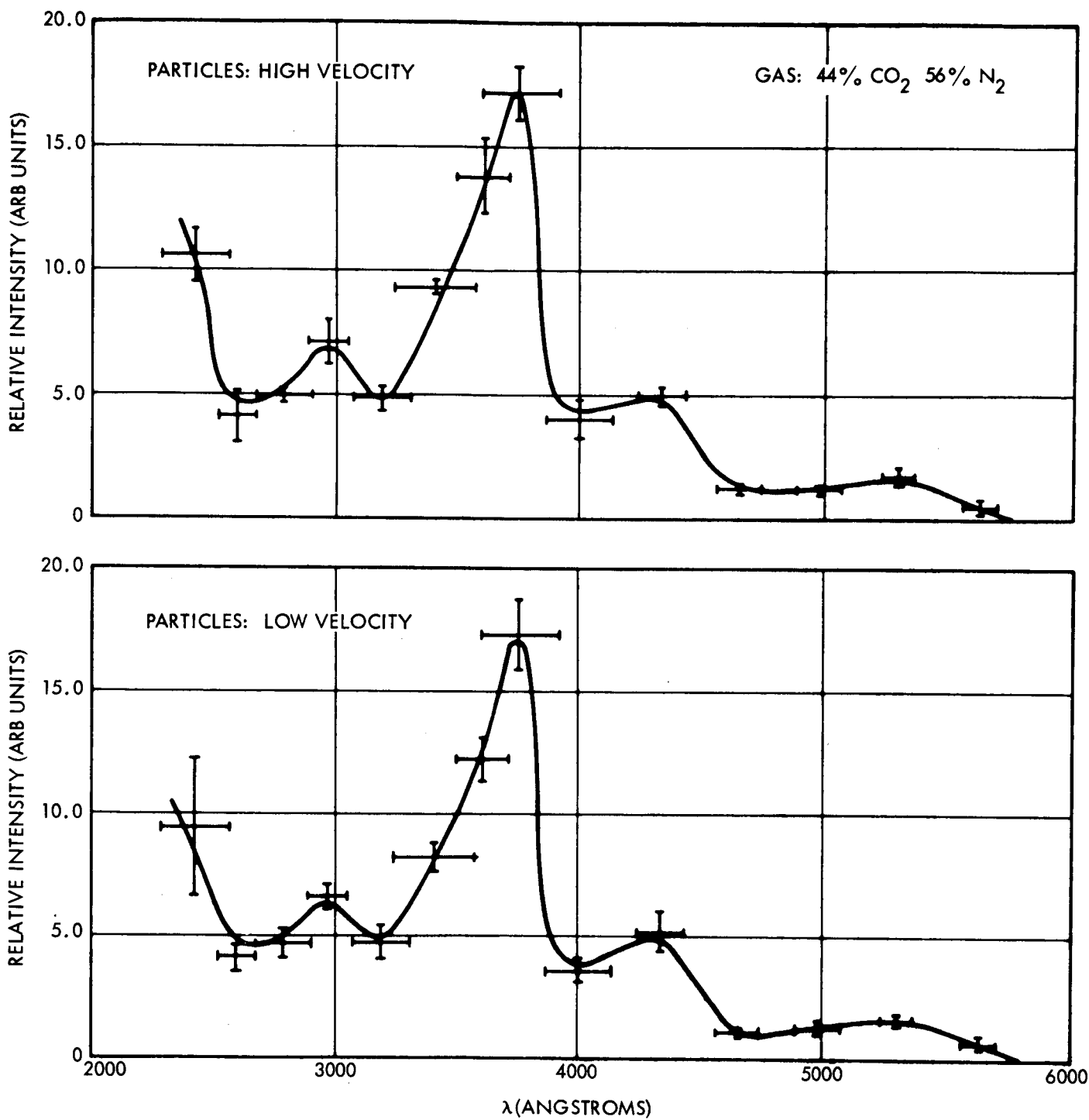


Figure A-4 Relative Intensity of Light Emission from Iron Particles in 44% CO₂ - 56% N₂. High velocity particles are 30 km/sec average and low velocity particles are 25 km/sec average. Vertical error bars are two standard deviations and horizontal error bars are full-width-at-half-maximum of the filter-phototube combination.

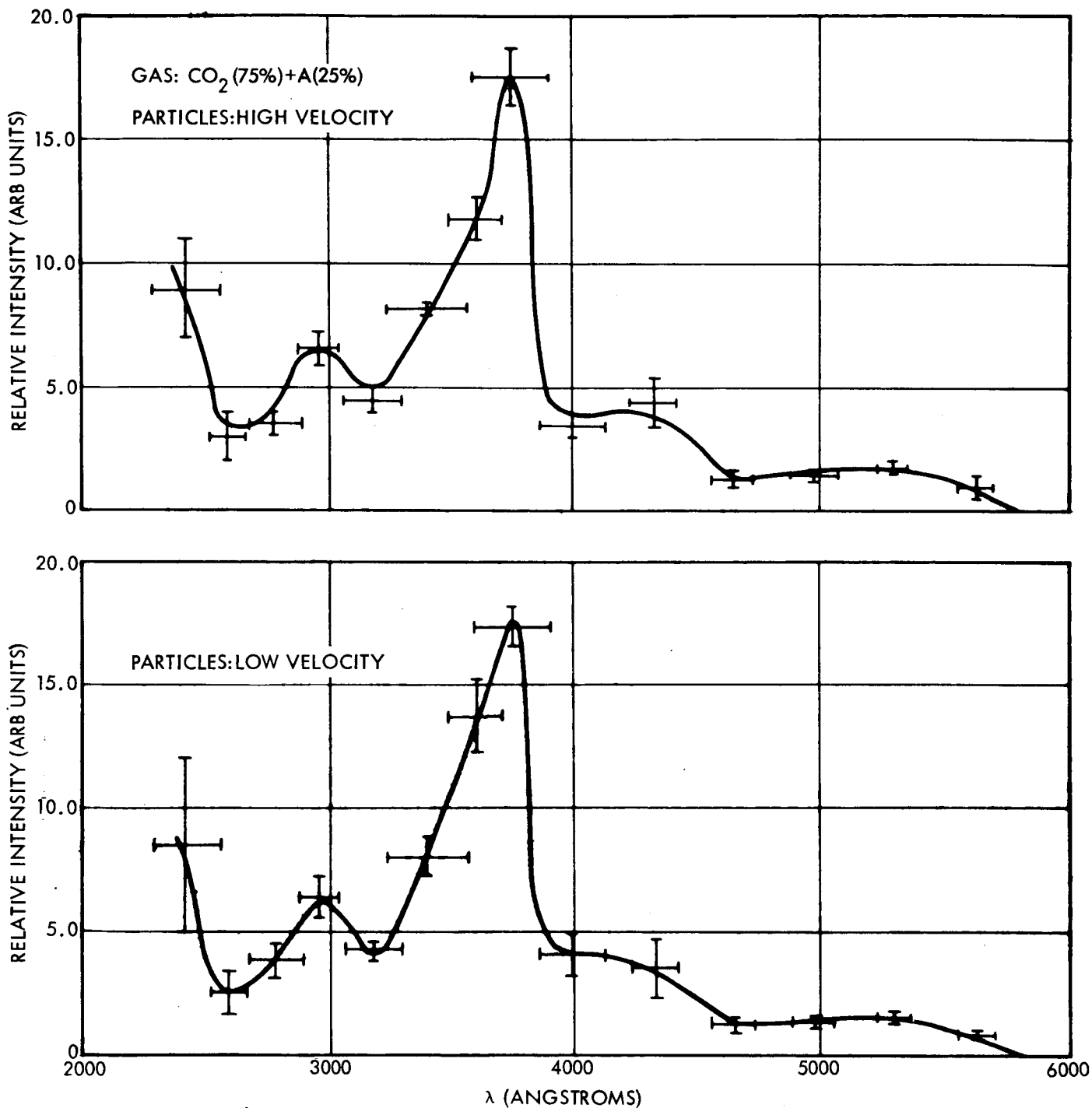


Figure A-5 Relative Intensity of Light Emission from Iron Particles in 75% CO₂ - 25% A. High velocity particles are 30 km/sec average and low velocity particles are 25 km/sec average. Vertical error bars are two standard deviations and horizontal error bars are full-width-at-half-maximum of the filter phototube combination.

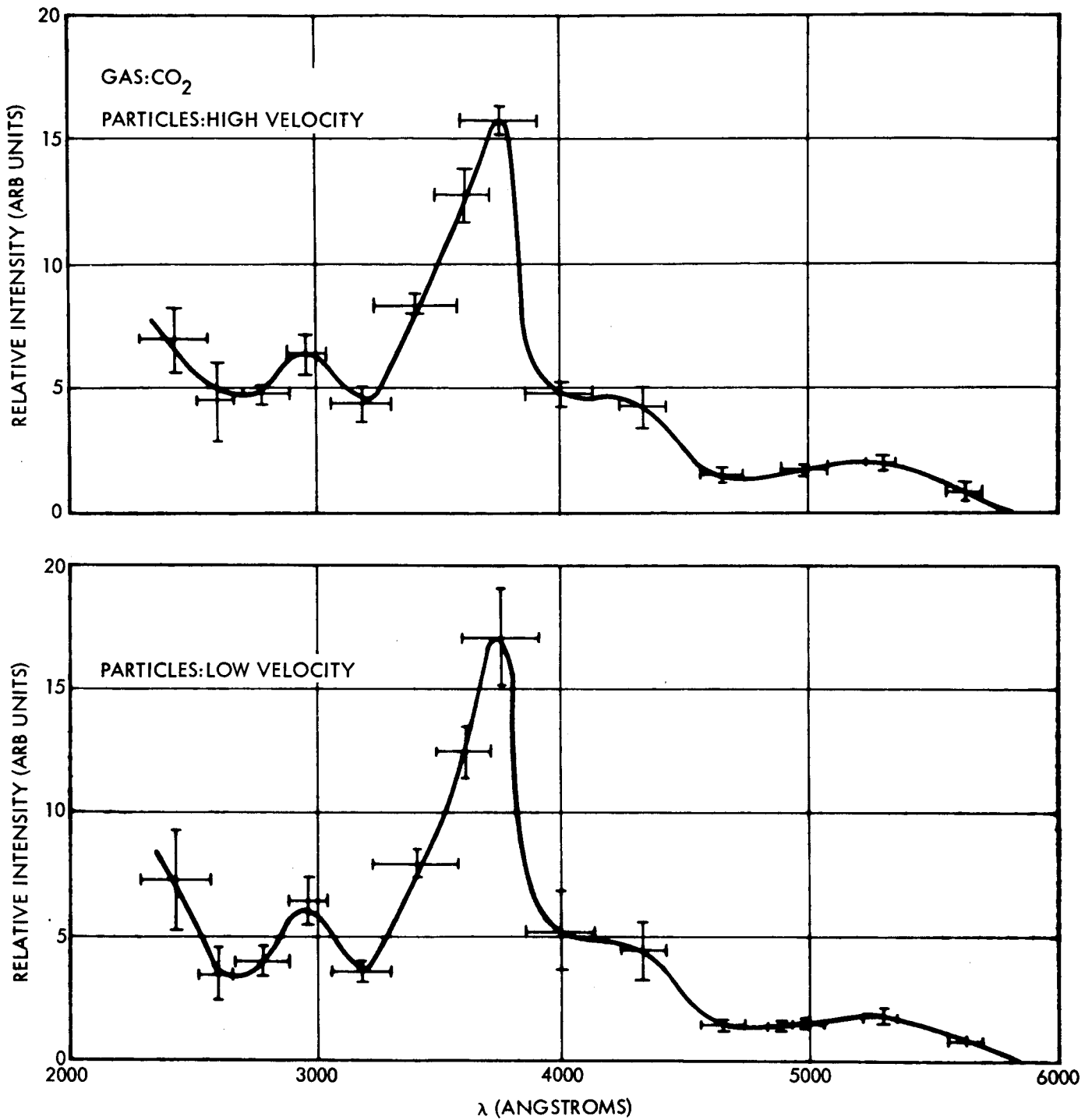


Figure A-6 Relative Intensity of Light Emission from Iron Particles in 100% CO₂. High velocity particles are 30 km/sec average and low velocity particles are 25 km/sec average. Vertical error bars are two standard deviations and horizontal error bars are full-width-at-half-maximum of the filter phototube combination.

Peak Wavelength	Air		75% CO ₂ - 25% A		44% CO ₂ - 56% N ₂		CO ₂	
	High Vel.	Low Vel.	High Vel.	Low Vel.	High Vel.	Low Vel.	High Vel.	Low Vel.
5630	.65 ± .12	.59 ± .18	1.00 ± .48	.77 ± .24	.53 ± .30	.71 ± .30	.82 ± .42	.82 ± .24
5300	1.67 ± .28	1.53 ± .37	1.75 ± .32	1.53 ± .28	1.67 ± .42	1.57 ± .23	1.99 ± .33	1.76 ± .28
4980	1.15 ± .12	1.26 ± .14	1.53 ± .22	1.31 ± .22	1.15 ± .20	1.26 ± .26	1.65 ± .19	1.45 ± .23
4650	1.18 ± .20	1.15 ± .34	1.34 ± .28	1.15 ± .29	1.17 ± .15	1.09 ± .12	1.49 ± .29	1.41 ± .21
4330	4.53 ± 1.05	5.15 ± .81	4.44 ± .95	3.51 ± 1.15	5.00 ± .30	5.17 ± .77	4.28 ± .89	4.46 ± 1.3
4100	4.37 ± .27	4.32 ± .81	3.46 ± .49	3.95 ± .87	3.95 ± .75	3.57 ± .54	4.81 ± .54	5.19 ± 1.5
3750	18.5 ± 1.58	18.9 ± 1.49	17.5 ± 1.15	17.3 ± .75	17.1 ± 1.07	17.3 ± 1.43	15.8 ± .62	17.0 ± 2.0
3600	12.5 ± .85	13.6 ± 1.55	11.8 ± .90	13.7 ± 1.5	13.8 ± 1.5	12.2 ± .93	12.8 ± 1.1	12.5 ± 1.1
3400	8.66 ± .62	8.42 ± .55	8.22 ± .23	7.97 ± .74	8.26 ± .27	8.16 ± .57	8.43 ± .44	7.87 ± .55
3180	5.71 ± .22	5.10 ± .68	4.47 ± .46	4.18 ± .40	4.84 ± .46	4.80 ± .62	4.40 ± .73	3.63 ± .37
2960	7.09 ± .78	7.39 ± .54	6.55 ± .65	6.37 ± .83	7.09 ± .89	6.61 ± .48	6.43 ± .83	6.37 ± 1.0
2780	5.40 ± .57	5.43 ± .48	3.64 ± .54	3.84 ± .74	4.89 ± .31	4.69 ± .60	4.83 ± .43	3.95 ± .57
2590	5.50 ± 1.4	4.1 ± .85	3.0 ± 1.0	2.5 ± .85	4.10 ± 1.1	4.2 ± .7	4.5 ± 1.6	3.5 ± 1.1
2420	10.9 ± 1.9	11.1 ± 1.3	8.9 ± 2.1	8.5 ± 3.5	10.6 ± 1.1	9.4 ± 2.8	7.0 ± 1.3	7.2 ± 2.0

TABLE A-1

Relative Intensity of Light Emission from Simulated Meteors

As can be seen from the data, the assumptions made above about the smoothness of the spectrum are not rigorously valid and therefore care must be taken in interpreting the data. Although the curve is drawn as a smooth one, it is clear that the spectrum may be highly structured with intense lines producing most of the energy. For example the combination of the FeI resonance multiplets listed in Table A-2 and the used Interference filters yield a very plausible explanation for the observed smoothed-out spectral energy distribution between 0.25 μ and 0.40 μ .

TABLE A-2

FeI Resonance Multiplets^{A-5}

FeI	$a^5D - Z^5F^\circ$	0.3649 μ - 0.3748 μ
	$a^5D - Z^5D^\circ$	0.3824 μ - 0.3930 μ
	$a^5D - Z^5P^\circ$	0.3441 μ - 0.3526 μ
	$a^5D - Y^5F^\circ$	0.2954 μ - 0.2973 μ
	$a^5D - Y^5D^\circ$	0.2984 μ - 0.3059 μ

There is also some question about the data point at 2400 Å. In this case the sensitivity curve of the PMT, the transmission curve of the cut-off filter and the transmission curve of the interference filter are all sharply falling, making the accurate evaluation of the integral in Eq.A-4 difficult.

During analyses of the data, an occasional point was found which did not agree well with the rest of the data in that set. A criterion was developed^{A-6} to form a statistical basis upon which to reject such spurious data. Whenever such a point was found in a set of data, the average value of the set and its standard deviation was recalculated leaving out the suspected data point. If the suspected point then lay more than 3 standard deviations from the new average, it was rejected. Out of more than 1000 data points taken, 37 were thus rejected. In rejecting a data point, the average value of the set usually was not changed significantly, but the standard deviation was.

The errors given are the standard deviations of the data taken. Errors in the reading of the photographs (which were read to 4 digits) were considered negligible and not included. The data for the transmission of the filters was taken from data supplied by the manufacturer for each filter. The relative response of the uv photomultiplier tube was calibrated at our facility using an Eppley standard light source and thermopile in the visible, and a Xenon arc lamp and a McPherson spectrograph in the uv region. It is estimated that the relative response is uncertain to within less than $\pm 15\%$.

A-4. TIME DEPENDENCE OF THE LIGHT EMISSION

No attempt was made to accurately measure the time dependence of the light emission, i.e., rise and fall times. However, the nature of the experiments permitted certain observations to be made.

The length of the segment of the trail viewed by the two PMT's was 2 cm, defined by two hollow tubes positioned coaxially with the particle trail. Given the particle velocities of about 20 to 30 km/sec, the particle itself was in the field of view for about one microsecond or less. Thus any light emission lasting more than a microsecond must be due to some delayed action effect.

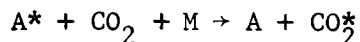
The outputs of the PMT's were integrated with an RC time constant of 50 to 100 μ secs, so that with no delayed emission the output pulse shape should have been a 1 μ sec risetime followed by an exponential decay. In fact this pulse shape was observed in the visible when the target gases were air, CO_2 , and $\text{CO}_2 + \text{N}_2$, or when observations were being made in the uv, regardless of the target gas.

However, when the target gas was the 75% $\text{CO}_2 + 25\%$ A mixture and observations were made in the visible, an anomalous pulse shape appeared. The PMT output pulse would rise to about 95% of its final value in the usual one microsecond but then instead of decaying exponentially it would continue to rise for about 5 μ secs more and then decay. While it was difficult to make any quantitative measurements under the experimental conditions, the effect was obvious, amounting to about 5% of the total light emission in the band under observation.

A few simple checks demonstrated it was not electronic in nature, and was associated only with the visible part of the spectrum obtained with the CO₂ - A gas mixture. For these reasons we concluded it was a delayed light emission, presumably due to the presence of the argon, since CO₂ was present in other mixtures not showing the same effect.

At this point a quick experiment was performed by substituting pure argon as the target gas. There was no evidence of delayed light emission in pure argon, so to first order the presence of both CO₂ and A is required.

This tentative explanation is suggested by the very close energy resonance of the AI metastable state AI: 3p⁵ (2P_{1/2}^o) 4p [1/2]^{A-5} at T_e = 104,102 cm⁻¹ with the CO₂ electronic states^{A-7} \tilde{H} (T_o = 100,650 cm⁻¹) and \tilde{I} (T_o = 100,940 cm⁻¹). Since the vibrational quantum energy of the ν_1 vibrational states is 1320 cm⁻¹ and the energy difference of the Argon metastable state and CO₂: \tilde{H} is only 3450 cm⁻¹, nearly exact energy resonance can be achieved with only one or two fundamental vibrational quanta excited. Subsequent cascading of the excited CO₂ by emitting a vacuum uv photon could yield delayed CO₂ emission in the wavelength range 0.28 μ \leftrightarrow 0.42 μ in accordance with observation. Symbolically, one can describe this delayed radiation by



The excited CO₂ decays by emission of a vacuum uv photon and subsequent emission of a second photon in the wavelength range being monitored by the PM tubes.

A-5. ABSOLUTE RADIANT EFFICIENCIES

The spectral measurements discussed above were done on a relative rather than an absolute basis. A short segment of trail was observed simultaneously by filtered and unfiltered photomultipliers and the signal from the filtered tube was normalized to the unfiltered tube signal. There was no need to know the amount of light from the total trail, or the mass of the particle causing the trail.

However, in order to make absolute measurements, it is necessary to measure the whole trail and to know the mass and velocity of the incoming particle. At sufficiently high velocities (> 20 km/sec) it may safely be assumed that the entire mass of the particle is vaporized. In this case, the luminous efficiency τ is given by

$$\int I dt = \tau (mv^2/2) \quad (A-5)$$

so that τ is the total light energy divided by the initial kinetic energy of the particle.

The large number of points desired for accurate spectral measurements made it impractical to try and measure absolute efficiencies at the same time, because of the extended data requirements and calculations necessary for the absolute measurements. Therefore, a second experiment was undertaken to measure the absolute luminous efficiencies for iron particles in the different target gases.

The experimental arrangement was identical to that described before^{A-3} in literature where the luminous efficiency for air was reported. The target

chamber is one containing two windows about 30 cm long each viewed by a photomultiplier tube about 35 cm away. The gas pressure was adjusted so that the particle trail was about 10 or 15 cm long and the signals at the photomultipliers integrated so that the output pulse was proportional to the total light produced. One of the windows was made of quartz and was viewed by a uv sensitive tube, an EMI 6255. The other window was made of plexiglass and viewed by a tube with a standard S-11 response, an RCA 6199.

With this arrangement, five particles of low velocity (20 to 25 km/sec) and five particles of high velocity (25 to 30 km/sec) were recorded for each of the four target gases. The data recorded for each particle were the particle mass and velocity and the total light output as measured by each of the two photomultipliers.

The signals from the photomultipliers were normalized to the particle initial kinetic energy, as in Eq. A-5. Given calibrated photomultipliers, these normalized signals could then be converted into an absolute efficiency. However, since the luminous efficiency for air is known^{A-2}, and the spectra in the different gases are identical to within the precision of our results, it was only necessary to measure the luminous efficiencies for the other gases relative to air. Care was taken to be sure the system gains remained constant during measurements for all gases.

In Table A-3 are listed the measured luminous efficiencies relative to air for the three target gases. The numbers marked "uv" are the results obtained with the EMI 6255 tube and those marked "visible" were obtained with the RCA 6199 tube. These relative efficiencies may be converted to

TABLE A-3

LUMINOUS EFFICIENCIES RELATIVE TO AIR

		Target Gas		
		$.75\text{CO}_2 + .25\text{A}$	$.56\text{N}_2 + .44\text{CO}_2$	CO_2
η (low velocity)	uv	$.30 \pm .09$	$.87 \pm .22$	$.39 \pm .09$
	vis.	$.31 \pm .11$	$.93 \pm .25$	$.44 \pm .11$
η (high velocity)	uv	$.56 \pm .11$	$.68 \pm .14$	$.43 \pm .09$
	vis.	$.60 \pm .13$	$.75 \pm .14$	$.46 \pm .09$
η (all velocities)	uv	$.43 \pm .15$	$.79 \pm .20$	$.41 \pm .09$
	vis.	$.45 \pm .17$	$.85 \pm .21$	$.45 \pm .09$

absolute efficiencies by multiplying by the absolute luminous efficiency for air in Reference A-3. This number for the visible is 0.005, valid for velocities between 20 and 40 km/sec.

The absolute efficiencies in the uv may be obtained for air by taking the area under the spectral curve in the wavelength band desired relative to the area under the curve from 3500 Å to 5800 Å. For example the area under the spectral curve for air from 2400 Å to 5800 Å divided by the area under the curve between 3500 Å and 5800 Å is 1.75. This means the total efficiency for air from 2400 Å to 5800 Å is $1.75 \times 0.005 \approx .009$.

The relative efficiencies listed in Table A-3 under "uv" may be converted to absolute efficiencies by multiplying by 0.009. They will then represent absolute efficiencies in the wavelength interval 2400 Å to 5800 Å.

As may be seen from Table A-3, there is an appreciable difference in the high and low velocity efficiencies in the .75 CO₂+ .25A gas mixture. The other gas mixtures showed no definite trend with velocity. Although this observational fact cannot be fully explained at this time because of lack of further experimental proof, the following consideration is offered: If one assumes that the excitation of metastable Argon can be an important factor in the total radiative efficiency in CO₂ - Argon mixture, then the expected decrease of excitation of the AI state (12.9 ev) for low velocities agrees with the observed facts. This explanation would be further supported by the observed afterglow in CO₂ - A mixtures discussed in Section A-4.

A-6. CONCLUSIONS

A-6.1 The relative spectral energy distribution of radiation from iron particles ablating at high and low velocities has been measured in the visible and ultraviolet regions. The spectra appear to be insensitive to particle velocity.

A-6.2 The gross features of the spectrum are three small peaks at about 5200 Å, 4200 Å, and 2900 Å, and a large peak at about 3700 Å. The large peak is approximately four times higher than the smaller ones. The observed spectra agree well with expected emission from FeI resonance multiplets.

A-6.3 Within the accuracy of the measurements the relative spectral energy distribution from the four different target gases are the same. This suggests that most of the radiation comes from excitation of the iron atoms with little excitation of the target gas. However, when one constituent of the target gas was argon, the presence of an afterglow (duration 5 to 10 μseconds) was noted in the visible portion of the spectrum. The afterglow was approximately 5% of the total emission and seemed to be spread uniformly through the visible spectral band. This may imply a small amount of target gas excitation with argon present.

A-6.4 The luminous efficiencies for iron particles in target gases of $.75\text{CO}_2 + .25\text{A}$, $.56\text{N}_2 + .44\text{CO}_2$, and CO_2 relative to the luminous efficiency for air have been measured and are listed in Table A-3. Radiative efficiencies marked "uv" are valid for the wavelength interval 2400 Å to 5800 Å, while those marked "visible" apply to the wavelength interval 3500 Å to 5800 Å. The absolute luminous efficiencies for air in these wavelength intervals are 0.009 and 0.005, respectively.

REFERENCES

- A-1 D. E. Evans, D. E. Pitts and G. L. Kraus, "Venus and Mars Nominal Natural Environment for Advanced Manned Planetary Missions," 2nd Edition, NASA SP-3016, (1967).
- A-2 J. C. Slattery and J. F. Friichtenicht, "Ionization Probability of Iron Particles at Meteoric Velocities," *Astrophys. Journal*, Vol. 147, No. 1, p. 235 (January 1967).
- A-3 "A Laboratory Measurement of Meteor Luminous Efficiency" by J. F. Friichtenicht, J. C. Slattery and E. Tagliaferri. NASA CR-787 and to be published in *Astrophysical Journal*, February 1968.
- A-4 J. F. Friichtenicht, "Two-Million-Volt Electrostatic Particle Accelerator for Hypervelocity Research," *Rev. Sci. Instru.*, Vol. 33, p. 209 (1962).
- A-5 Ch. E. Moore, "Atomic Energy Levels," Vol. II, Circular of the NBS, 467, (1958).
- A-6 Yardley Beers, Theory of Error, Addison-Wesley, Cambridge, (1953).
- A-7 G. Herzberg, Molecular Spectra and Molecular Structure, Vol. III, "Electronic Spectra of Polyatomic Molecules," D. Van Nostrand Co., Inc. (1967).

LIST OF FIGURES

FIGURE

- A-1 Block Diagram of Experimental Arrangement.
- A-2 Relative Spectral Response of EMI 6255 uv Photomultiplier Tube.
- A-3 Relative Intensity of Light Emission from Iron Particles in Air. High velocity particles are 30 km/sec average and low velocity particles are 25 km/sec average. Vertical error bars are two standard deviations and horizontal error bars are full-width-at-half-maximum of the filter-phototube combination.
- A-4 Relative Intensity of Light Emission from Iron Particles in 44% CO₂ - 56% N₂. High velocity particles are 30 km/sec average and low velocity particles are 25 km/sec average. Vertical error bars are two standard deviations and horizontal error bars are full-width-at-half-maximum of the filter-phototube combination.
- A-5 Relative Intensity of Light Emission from Iron Particles in 75% CO₂ - 25% A. High velocity particles are 30 km/sec average and low velocity particles are 25 km/sec average. Vertical error bars are two standard deviations and horizontal error bars are full-width-at-half-maximum of the filter phototube combination.
- A-6 Relative Intensity of Light Emission from Iron Particles in 100% CO₂. High velocity particles are 30 km/sec average and low velocity particles are 25 km/sec average. Vertical error bars are two standard deviations and horizontal error bars are full-width-at-half-maximum of the filter phototube combination.